The Surface Chemistry and Interface Engineering of Lead Sulphide Colloidal Quantum Dots for Photovoltaic Applications

Neo Chi Jin, Darren
Mansfield College

A thesis submitted in fulfilment of requirement for the degree of
DPhil in Materials at **the University of Oxford**

Abstract

This thesis examines the effect of lead sulphide (PbS) CQDs' surface chemistry and interfaces to their photovoltaic performance.

Using PbS CQDs as the starting material, cation-exchange was utilised to form PbS/CdS core/shell CQDs, which were thoroughly characterised and the improved surface passivation was shown by increased photoluminescence yield and lifetime. The core/shell CQDs were incorporated into a ZnO/CQD heterojunction solar cell device and showed a substantial improvement of the mean open-circuit voltage (V_{oc}), from 0.4 V to 0.6 V, over PbS reference devices. By optimising shell thickness and surface ligands, core/shell CQD devices with average device efficiency of 5.6 % were fabricated as compared to 3.0 % for unshelled PbS devices.

The lower defect density due to better passivation confers lower carrier density in core/shell CQD film. To take advantage of low defect concentration and to aid charge extraction, a 3 dimensional quantum funnel concept was sought of by blending two populations of PbS/CdS CQDs of different sizes. By incorporating a blend component within a heterojunction device, even when the device thickness is beyond what is optimal for the depletion width and the diffusion length of the system, high V_{oc} is still maintained. In a separate study, a *p-i-n* device strategy was examined, and with this approach, a maximum device efficiency of 6.4 % was achieved.

Despite the improvements made to V_{oc} by optimizing surface passivation, fill factors of the devices are low. By using poly(3-hexylthiophene-2,5-diyl) (P3HT) as a hole transport material (HTM), fill factor and the overall performance improved over a reference device without the HTM. Further studies showed that oxidation of the HTM material results in increased *p*-type characteristic, thus optimising hole transport. This beneficial oxidation process also makes the device air-stable. From this, devices of up to 8.1 % efficiency and devices with fill factor as high as 0.72 were fabricated.

Dedication

To God, thank you for watching over me. To my parents, Neo Peng Soon and Teo Lay Cheng, and my sister Louise Neo, thank you for your love, support and prayers.

Acknowledgements

At the time of writing this thesis, I have known Professor Andrew Watt as my supervisor but more significantly, as someone who cares for our safety and well-being, as well as a friend whom I could approach for guidance and inspiration in my purposeful D.Phil journey. I thank him for the numerous opportunities he has given me in terms of networking and collaborative projects. I would like to also thank Professor Hazel Assender for her tremendous support and guidance as my co-supervisor. I value her constructive feedbacks and critical comments. I thank her for helping me with my writing skills and asking questions which beckons me to think about other possibility and critically assess the validity of my research results.

I thank my ex-colleague Dr Cheng Cheng, for coaching me and formally introducing me to the research in PbS colloidal quantum dots from synthesis, to fabrication of devices and optoelectronic characterisation techniques. Dr Cheng Cheng also played an important role as my college parent and in making my initial stay in Oxford more bearable. His generosity and contributions to the lab will never be forgotten. I also thank Dr Chris Cattley for his spontaneity in scientific discussions and his effort in keeping the lab in order. I will always remember the quirky jokes he shared with us. Not forgetting Dr Jenna Holder for her help in advanced optoelectronic characterisation and her superb effort in keeping lab social events going. I would also like say a special thank you to Natasha Hjerrald for being such a memorable labmate as well as a running companion. I give thanks to my fellow peers,

Assia Kasdi, Inji Yeom, Nina Klein, Nanlin Zhang, Yujiro Tazawa and Zhanet Zaharieva for their enthusiasm and lively discussions.

At this juncture, I would like to formally express my gratitude towards my collaborators. I thank Prof Henry Snaith, from the Physics department, for collaboration opportunities. Likewise, I would like to acknowledge Dr Samuel Stranks and Dr Giles Eperon for their contributions towards this collaboration and also with their aid in photoluminescence characterisation. I also thank Dr Simon Fairclough for his advice on TEM usage and XRD simulations. I would also like to take the opportunity to thank Prof. Wendy Flavell, Prof. David Binks and their team of post-doctorates and PhD students from the Photon Science Institute, University of Manchester for their enormous help in term of XPS support and other collaborative efforts. Thank you for being such good hosts when I was there for a lab visit. I would like to thank Prof. Neil Greenham from the Univeristy of Cambridge and his PhD student, Tom Jellicoe, in providing an invaluable assistant on the PLQY measurement of our PbS/CdS CQD. I thank Prof. Kim from Engineering department and his team of post-doctorates for numerous opportunities for collaboration and fruitful discussions. I thank Richard Turner and Dr John Topping for their technical support and I thank Dr Ziqian Ding, Dr Long Jiang, Dr Vincent Tobin for numerous discussions.

Last but not least, I would like to acknowledge my loved ones. To my mum, dad and sister, thank you for all your prayers and well wishes, not forgetting the timely gift box from Singapore which always never fails to surprise me. To my girlfriend Jasmine See, thank you so much for your care, emotional support and love.

Statement of Originality

This thesis is an account of work carried out by the author in the Department of Materials, the University of Oxford under the supervision of Professor Andrew Watt and Professor Hazel Assender. Any work of others that has been utilised, directly or indirectly, is duly acknowledged in the text, and a list of references is presented at the end of each chapter. No part of this thesis has been submitted towards the completion of another degree at the University of Oxford or elsewhere. Parts of the thesis have been submitted to or published in the following scientific journals or conference presentations:

Journal articles:

Neo, Darren C. J. *et al.* **Influence of Shell Thickness and Surface Passivation on PbS/CdS Core/Shell Colloidal Quantum Dot Solar Cells**. *Chem. Mater.* 140606160802003 (2014). doi:10.1021/cm501595u

Neo, Darren C. J. *et al.* **Quantum funneling in blended multi-band gap core/shell colloidal quantum dot solar cells.** Applied Physics Letters, 107, 103902 (2015), doi: 10.1063/1.4930144

Neo, Darren C. J. *et al.* **P3HT as a Hole Transport Layer for Colloidal Quantum Dot Solar Cells with High Fill Factors**. Manuscript submitted and awaiting for review.

Conference proceedings:

Darren C. J. Neo, Cheng C., Assender H.E., Watt A.A.R., **PbS/CdS Core/Shell Colloidal Quantum Dot Solar Cells**. In the 10th *Photovoltaic Science Application and Technology (PVSAT-10)*, Loughborough, UK, 2014. (Poster presentation)

Darren C. J. Neo, Cheng C., Assender H.E., Watt A.A.R., **Developing a robust surface passivation strategy for colloidal quantum dot solar cells: The core/shell approach**. In Nanocrystal Zing Conferences, Dominican Republic, 2014. (Poster presentation)

Darren C. J. Neo, Cheng C., Assender H.E., Watt A.A.R., **PbS/CdS Core/Shell Nanocrystals For Solution-Processed Colloidal Quantum Dot Solar Cells**. In *2014 MRS Fall Meeting*, Boston, USA, 2014. (Poster presentation)

Darren C. J. Neo, Assender H.E., Watt A.A.R., **Surface and interface engineering of lead sulphide colloidal quantum dot for better photovoltaic performance.** In Solution Processed Innovative Solar Cell (SPINS) 2015, Santiago de Compostela. (Oral presentation)

Darren C. J. Neo, Assender H.E., Watt A.A.R., **Interface and surface engineering of colloidal quantum dots for photovoltaic applications.** Rank Prize Fund conference 2015- Symposium on Electroluminescent and Photovoltaic Effects in Nanocrystal Quantum Dots. (Oral presentation)

Signed…………………………………………… Date……………….

Table of Contents

List of Tables

List of Figures

List of Abbreviations

Ag	Silver
Al	Aluminium
AM	Air Mass
Au	Gold
BDT	1,4-Benzenedithiol
BHJ	Bulk heterojunction
Bi_2S_3	Bismuth sulphide
C-V	Capacitance - voltage
CB	Conduction band
CdS	Cadmium sulphide
CdSe	Cadmium selenide
CTAB	Cetyltrimethylammonium bromide
CQD	Colloidal quantum dot
EDT	1,2-Ethaneidthiol
E_g	Band gap
EQE	External quantum efficiency
FET	Field effect transistor
FF	Fill factor
FTO	Fluorine-doped tin oxide
HOMO	Highest occupied molecular orbital
I-V	Current - voltage
ITO	Indium-doped tin oxide
J_o	Reverse saturation current
J_{sc}	Short circuit current density
J-V	Current density - voltage
LED	Light-emitting diode
LUMO	Lowest unoccupied molecular orbital
MoO_3	Molybdenum trioxide
MPA	3-Mercaptopropinoic acid
NREL	National Renewable Energy Laboratory
OA	Oleic acid
ODE	1-Octadecene
P3HT	Poly(3-hexylthiophene-2,5-diyl)
PbS	Lead sulphide
PbSe	Lead selenide
PCBM	Phenyl-C61-butyric acid methyl ester
PCE	Power conversion efficiency
PEDOT:PSS	poly(3,4-ethylenedioxythiophene) poly(styrenesulfonate)
PL	Photoluminescence
R_s	Series resistance
R_{sh}	Shunt resistance

SIMS	Secondary ion mass spectrometry
Spiro OMeTAD	$N^2,N^2,N^{2'},N^{2'},N^7,N^7,N^{7'},N^{7'}$-octakis(4-methoxyphenyl)-9,9′-spirobi[9H-fluorene]-2,2′,7,7′-tetramine
TCO	Transparent conductive oxide
TEM	Transmission electron microscope
TiO_2	Titanium dioxide
$(TMS)_2S$	Bis(trimethylsilyl) sulphide
VB	Valence band
V_{bi}	Built-in potential
V_{oc}	Open circuit voltage
XRD	X-ray diffraction
XPS	X-ray photoelectron spectroscopy
ZnO	Zinc oxide

Chapter 1 – Introduction

1.1 Harnessing solar energy

The sun is a constant source of blackbody radiation at 5800K: it provides about 1.74×10^{17} W to the Earth's upper atmosphere[1] with an average intensity of 1366 Wm^{-2}, known as the solar constant[2] (or Air mass zero (AM 0)). On the terrestrial level, this value is reduced to around 1000 Wm^{-2} by atmospheric light absorption and scattering, which is set as a standard for solar cell performance testing (or AM 1.5G)[3] (see *Figure 1-1*). Contrary to popular belief, as compared to many other energy sources, photovoltaics require relatively little space to create power. To put things into perspective, with current technology only about 0.4 % worth of the earth's surface fitted with solar panels would be required to generate all the energy (be it transportation, buildings, industry, electricity, etc.) consumed by the whole planet[4]. Despite temporal/seasonal changes and intermittency due to weather/cloud cover, solar radiance is a rather equally distributed energy resource – all inhabited parts of the world have access to sunlight[5] whereas for fossil fuels and other extractive energy resources, this is not the case.
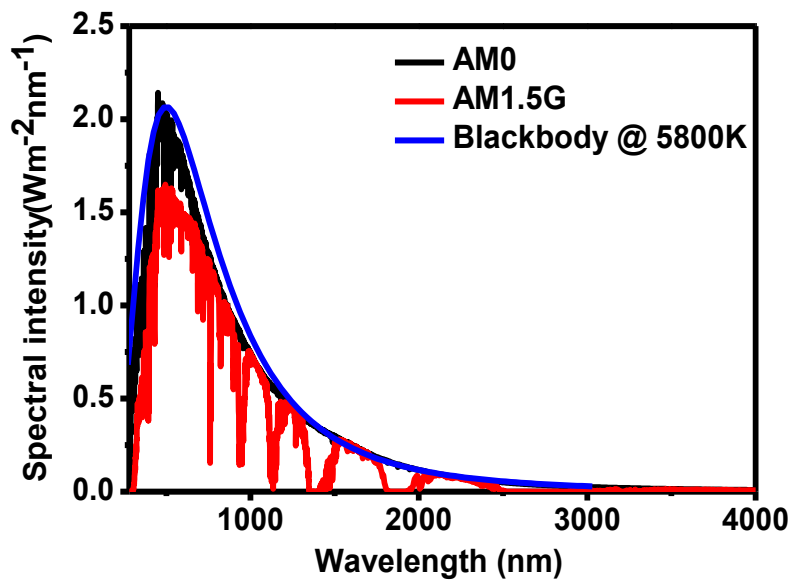
Figure 1-1. Solar spectrum irradiance as taken just outside Earth's atmosphere (AM 0), global averaged terrestrial data (AM 1.5G) and a blackbody approximation of the sun using the sun's surface temperature of about 5800 K. Raw data extracted from reference[6].

There are various ways of harnessing this abundant source of energy:

(i)   Solar thermal collection. This is the most conventional way of using solar energy. Usage can be in the form of heating water, solar air-conditioning and even cooking, just to name a few.

(ii)   Photovoltaic cells or solar cells. A more recent form of solar energy collection that involves conversion of radiant energy into the more distributable and accessible electrical energy.

(iii)   Concentrated solar power. Radiant energy from the sun is concentrated using parabolic mirrors and then used as a heat source for conventional power plants.

(iv)   Photocatalytic hydrogen generation. This is a relatively new area which involves using light energy to break down water into oxygen and hydrogen. It

is like a non-electrical analogue to electrolysis of water. The hydrogen produced

can be then use as a clean fuel.

In this thesis, the focus will be on photovoltaic cell technology.

1.2   Current status of solar cell technology

Given the ever rising energy demand of the world, coupled with a finite fossil fuel resource

and increased CO_2 emission[7] (see *Figure 1-2*), the pressure to shift towards green and

renewable energy is on. In recent times, there is a huge drive for lowering the cost of solar

cell modules and panels. In the United States, the average cost per installed watt of

photovoltaics has dropped from \$7.50/watt in 2009[8] to \$4.44/watt in 2012 and in 2011

alone, the cost per installed watt declined 17.4 %[9].

Note: Mtoe = million tonnes of oil equivalent; Gt = gigatonnes.
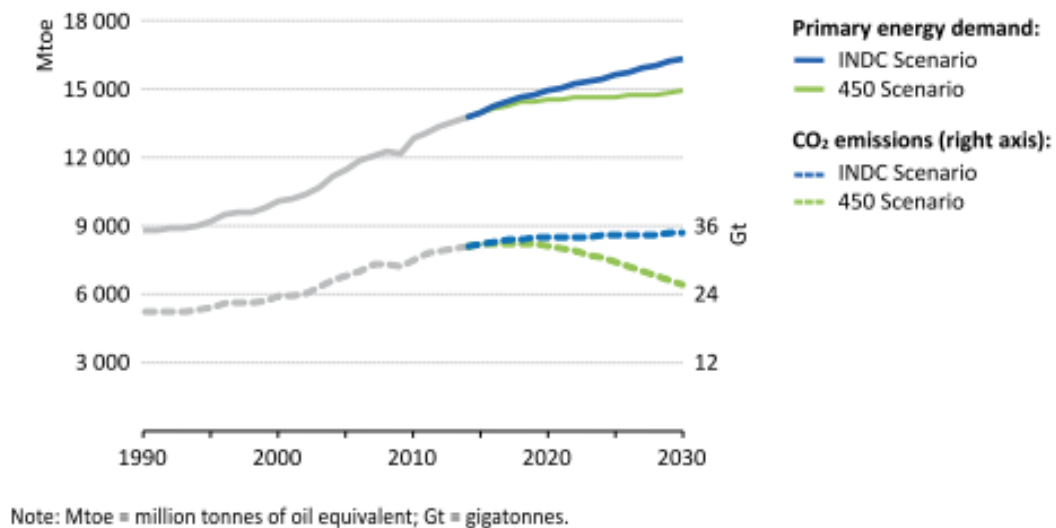
Figure 1-2. The global trend and projection of energy demands and CO_2 emissions. INDC Scenario

represents Intended Nationally Determined Contributions (INDCs) submitted by governments the

different countries while 450 Scenario is a more optimistic estimate which is based on a prediction

consistent with around a 50 % probability of meeting the 2°C climate goal. Obtained from

reference[7].

Nevertheless, the current averaged energy cost for photovolatics is still higher than that of fossil fuels. *Figure 1-3(a)* shows the case for US energy prices by source. This might explain why the current global energy production from photovoltaics is dwarfed by conventional fossil fuel sources (see *Figure 1-3(b)*). Therefore, there is still an urgent motivation to drive prices of photovoltaics further down before it can be widely adopted.
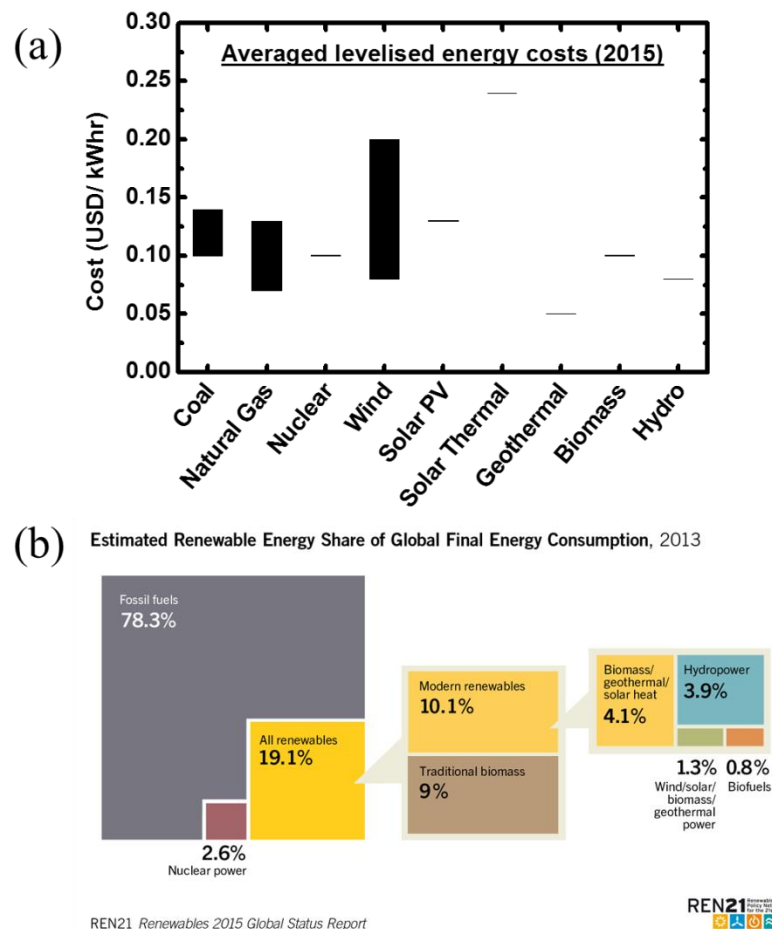
Figure 1-3. (a) Averaged levelised cost estimated for the year 2015 in US alone[10]. (b) World energy consumption distinguished by source, a global estimate of the year 2013, obtained from reference[11].

As of today, solar cell technology can by classified into three generations:

(i)   First generation – The wafer based solar cell represents the most conventional as well as the most established class of photovoltaic. This includes crystalline silicon solar cells and gallium arsenide solar cells.

(ii)   Second generation - Thin film solar cell represents the next wave of technology that sees the possibility of bringing down the cost of photovoltaics by lowering material usage and manufacturing costs. This class includes amorphous silicon, cadmium telluride and copper indium gallium sulphide/selenide solar cells.

(iii)   Emerging thin film technologies- The next generation (or third generation) of solar cells. This covers a wide range of materials but the key idea surrounding them is the ease of fabrication which makes such technologies attractive. The promise of cheaper material and manufacturing cost makes them the predicted highest efficiency to cost ratio group of solar cells (see *Figure 1-4(a)*). Many of them can be solution-processed and can be fabricated on curved or flexible substrates – their versatility leads to a spectrum of applications, right from very specialised usage, like in the military, where portability is a key factor, to house hold/personal usage. Most of these technologies are still not available in the market but huge focus is placed on its research for device improvement, stability and scalability. PbS CQD solar cells fall under this category.
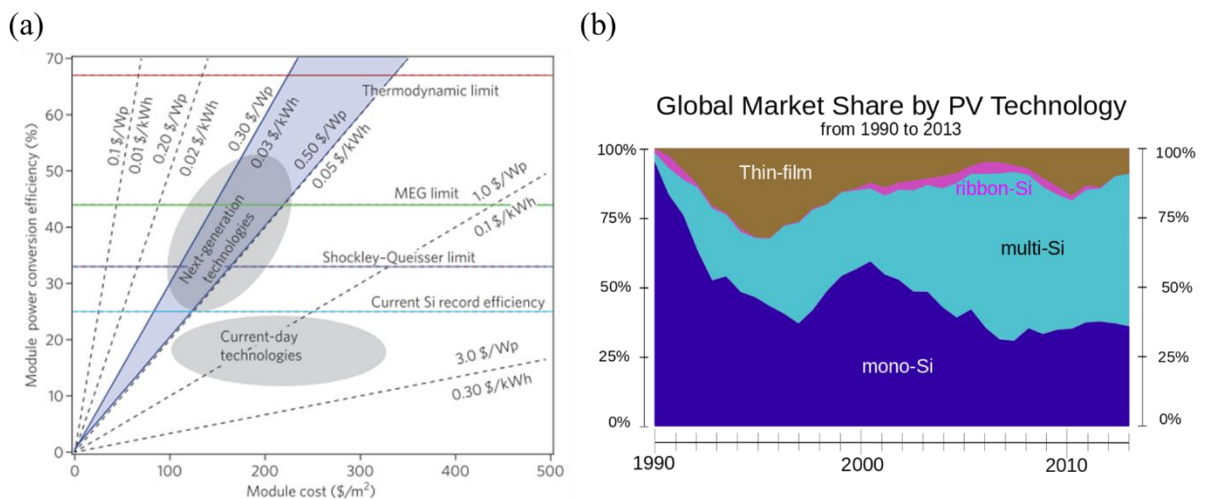
Figure 1-4. (a) Relationship between power conversion efficiency, module areal costs and cost per peak watt (in \$/Wp). A given \$/Wp (dashed black lines) can be achieved at a lower efficiency if the

module costs also decrease, and higher module costs can be tolerated if the module PCE also increases. For next-generation technologies the goal is to reach 0.03–0.05 $/kWh, denoted by the blue shaded region. Graph obtained from reference[12]. (b) The market share of the various PV technologies. Mono, multi and ribbon-Si can be classified as the first generation solar cell and thin film as the second generation. Data adapted from reference[13]

The current market share is dominated by the first generation solar cells (see *Figure 1-4(b)*). As of today, silicon and commercial thin film technologies far outperform the next generation technologies. However, with on-going research for better device performance and stability, and the promise of lower manufacturing costs, the next generation solar cell technology is poised to take over the first generation solar cells in market share.

1.3   PbS CQD technology as a candidate for the next generation solar cell

For the next generation of solar cell to become commercially available, cost effectiveness or high performance to cost ratio is key. PbS CQD solar cell technology is one such hopeful candidate: Low temperature and easy fabrication procedures drive the manufacturing costs down, and solution processing offers easy mass production approaches like ink jet printing, spray coating[14] and roll to roll fabrication[15], which allows high throughput production of solar cells. Moreover, it is particularly promising as an emerging thin film because PbS offers the possibility of band gap tuning, just by changing the size of the quantum dot, so as to better match the solar spectrum[16]. Also, there are many other quantum mechanical phenomena, like multiple exciton generation and hot electron collection, which present the possibility of breaking the Shockley–Queisser limit with a single junction solar cell[17,18].

Rapid advances in materials processing and device physics have driven impressive performance progress. Since PbS CQDs were first integrated into solar cell devices[19], they

have made remarkable improvements from a modest sub 1% to the current record of 9.9 %
power conversion efficiency[20] in a span of 10 years. However, the potential of this
technology is still masked by the difficulty of controlling surface defects and the lack of
complete understanding of charge transport within a system of colloidal quantum dots[21].
To elucidate the issue, a careful study of the intricate nature of charge transport processes
and a deeper understanding of the intimate link between the chemistry of the quantum dots
and their optoelectronic properties is required.

1.4   Aim of the thesis

The performance of PbS CQD solar cells is currently limited by low open-circuit voltages
(V_{oc}) and fill factors (*FF*). The goal of this thesis is to tackle these issues by focusing on
two aspects of materials chemistry- the surface passivation of CQDs and the interface
material between the CQD film and the electrodes. The following questions will be
addressed:

(i)   Whether V_{oc} could be improved by better surface passivation and defect mediation
         of PbS because of lower trap-related non radiative recombination and whether this
         passivation can be conferred by using a core/shell CQD strategy?

(ii)   Can overall device performance be further improved with device architectural
         modifications so as to circumvent the innate poor charge transport properties of
         quantum dots?

(iii)   Can the fill factor of CQD solar cell devices be improved by shifting away from
         relying too much on the depletion width and therefore, looking into enhancing
         diffusive transport? Is it possible to aid diffusive transport by incorporating a hole
         transport material in a heterojunction device?

1.5   Structure of thesis

Chapter 2 provides the reader with the theoretical background on solar cells as well as quantum dots. Then chapter 3 is a literature survey of PbS CQD technology in photovoltaic application and their recent progress in photovoltaic devices. Chapter 4 describes the experimental methodology of materials synthesis, characterisation and device fabrication as applied in the next few chapters. Chapter 5 encompasses the experimental results of synthesising and characterising PbS/CdS core/shell CQDs and eventually, the report of the performance of PbS/CdS core/shell devices with an inverted heterojunction structure of ITO-PEDOT:PSS-CQD-ZnO-Al device structure with the focus on optimising the shell thickness and ligand treatment. Chapter 6 explores utilising PbS/CdS core/shell in non-conventional device architectures so as to extend the active layer thickness and to also improve overall device performance. Chapter 7 discusses about utilizing P3HT as a hole transport layer, sandwiched between PbS film and the top electrode, for an improved device *FF*, overall performance as well as device stability. Chapter 8 finally concludes the main thesis findings and suggests future work to be carried out.

Chapter 2 – Solar cells and the colloidal quantum dot

2.1   The colloidal quantum dot

A quantum dot is a nanocrystal - a material that has a physical dimension so small that it displays quantum confinement effect in all three dimensions, which results in an increase in band gap and discretisation of energy levels. The band gap is determined by the energy difference between the highest occupied molecular orbital (HOMO) level and the lowest unoccupied molecular orbital (LUMO) level. The threshold size for which quantum confinement takes place is given by the exciton Bohr radius, which varies between different materials. At such small dimensions, the ratio of surface atoms to bulk atoms becomes significant. Due to the abrupt termination to the crystal structure, the surface atoms are associated with dangling bonds which results in defect states. These defects are detrimental to the optoelectronic properties of quantum dots and thus, the surface must be properly terminated or passivated.
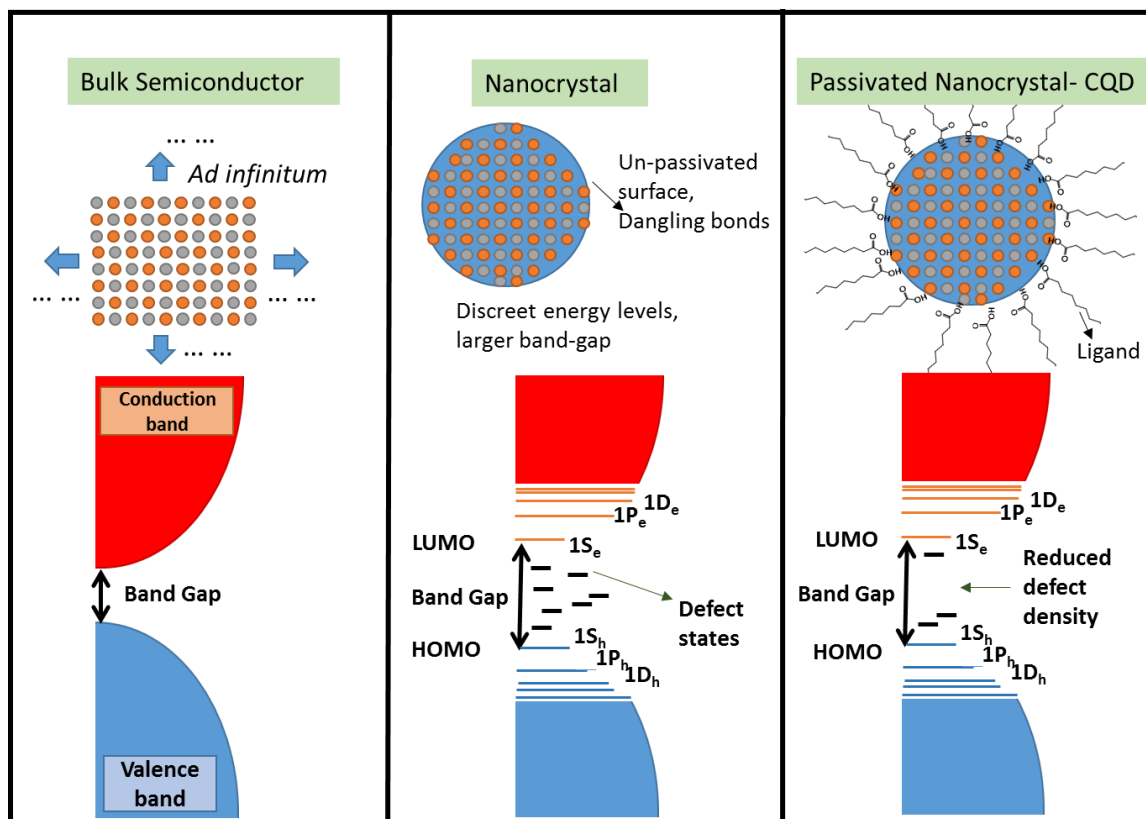
Figure 2-1. A schematic representation showing the difference between a bulk semiconductor, a nanocrystal (or quantum dot) and a colloidal quantum dot.

CQDs are quantum dots terminated by passivating species, known as ligands as illustrated in *Figure 2-1*. Passivation is essentially tying down dangling bonds, by chemical bond formation, which then reorganizes the energy states of the surface atoms. Since a CQD has high percentage of surface atoms, the choice of ligand would ultimately affect its electronic properties. Passivation is crucial even in the synthesis step as it serves as an impediment to further atomic accumulation beyond a certain size, stabilizing the CQDs by steric hindrance and rendering them soluble in the medium of synthesis.

High quality CQDs are often produced by the hot-injection method, which was pioneered by Murray *et al.*[22], and CQDs obtained from this method are capable of reaching near monodispersity (size variation as small as 5 %). The importance of a small size variation for optimum electronic properties will be explained in a later section. The hot-injection

method relies on the rapid introduction of the anionic precursor into a hot mixture of the metal precursor and surfactant. A typical setup for the lab-scale synthesis of CQDs by the hot-injection approach is shown in *Figure 2-2(a)*. The mechanism of the hot-injection approach can be described as follows. Right after the injection, the precursor species rapidly decompose to give free reactive species, which react with the metal precursors. The high degree of saturation of reactants provides the driving force to create numerous nuclei of the nanocrystal. Nuclei that have sizes beyond the critical size continue to grow while those that are smaller shrink and disappear. During the synthesis, the surfactant (ligand) molecules play an important role in tuning the reactivity between the precursors and also regulate the growth of the nanocrystal size over time. This is because they are constantly adsorbing and desorbing from the surface of the nanocrystals as growth carries on, thus allowing the addition or removal of chemical species at the surface of the nanocrystals. When the synthesis is halted by lowering the reaction temperature, a coating of ligands around the nanocrystals remains, enabling their solubility in a variety of solvents. The size and size distribution of CQDs can be very easily estimated by taking the absorption spectrum of an aliquot of the CQD solution. With reference to an example on a PbS CQD sample in *Figure 2-2(b)* and *(c)*, the background absorption is first removed from the experimentally obtained absorption curve by comparing it with the absorption curve of the sample holder containing the solvent but without the CQD, and next, the curve is converted to an energy axis instead of wavelengths. A Gaussian peak fit is then applied to the resultant peak, also known as the exciton peak, where the peak position is the mean band gap (and can be converted to CQD size) and standard deviation, σ, gives us information about the size dispersity in the CQD population. To calculate the diameter of PbS CQD, an empirical relation formulated by Moreels *et al.* is used[23]:

$$E_g = 0.41 + (0.0252d^2 + 0.283d)^{-1} \hspace{2cm} \textit{Equation 2-1}$$

where E_g is the band gap of the PbS CQD in eV as determined by the exciton peak in the absorption spectrum and d is the diameter of particle in nm.
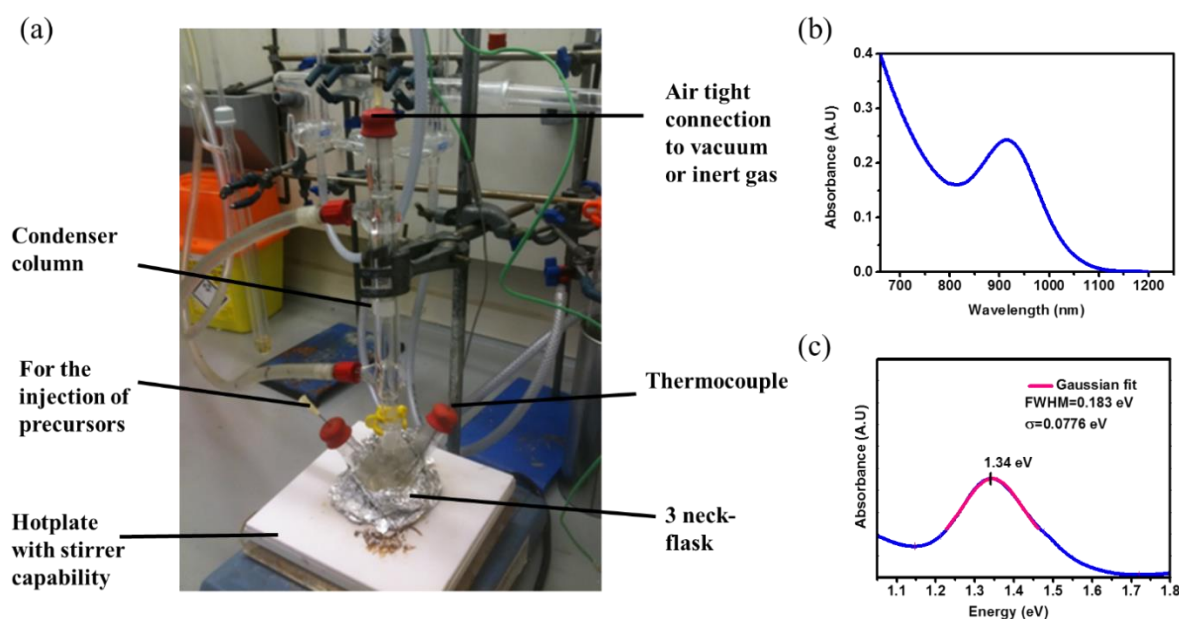
Figure 2-2. (a) A typical Schlenk line set up used for the synthesis of CQD by hot injection approach. (b) Absorbance curve obtained from UV-Vis-NIR absorption spectroscopy on a particular batch of PbS CQD sample. (c) The same curve with baseline subtracted, axis converted and peak fitted to a Gaussian distribution.

At the synthesis stage, long-chain, bulky, ligands are usually used to ensure maximum colloidal stability. However, when they are dispensed onto a surface, the evaporation of solvent results in a solid film of CQD and in this state, the film can be thought of as a composite of dispersed crystalline semiconductor in a matrix of insulating ligands. Therefore, in device applications, where effective transport of charge carriers is required, the long insulating ligands are swapped with shorter ones via ligand exchange, so as to increase the proximity between quantum dots. The effect of increased proximity will be

discussed in a later section but in the next section, the basics of photovoltaic action will be explained.

2.2   The physics of solar cell

2.2.1   Capturing light energy

The amount of sunlight available on the surface of the earth can be represented by the AM 1.5G and this is discussed in section 1.1. Much of this energy is concentrated in the visible range with a long tail extending into the infrared region of the spectrum. The composition of the solar radiation consists of approximately 50% infrared, 40% visible, and 10% in the ultraviolet portions of the electromagnetic spectrum[6]. For a semiconductor, only photons of energy equal or greater than the band gap will be absorbed and also, the extra amount of energy of the photon beyond that of the band gap would be lost as heat. Therefore, for a device that has only a single junction, the size of the band gap determines how efficiently the solar spectrum is utilised. If the band gap is lower than optimal, more photons can be absorbed but the amount of energy wasted as heat would be larger and this will also translate to a lower maximum possible device V_{oc}. Conversely, if the band gap is larger than optimal, less photons of the solar spectrum will be absorbed, leading to a lower device J_{sc}. The best efficiency obtainable with that optimal band gap size (of 1.1 eV) is calculated to be 33% and is termed as the Shockley–Queisser limit[24] (see *Figure 2-3(a)*). Nevertheless, there are ways to overcome this limit and one of which involves utilising more than one separate junction in a solar cell device, each with a different band gap to collectively capture a larger portion of the solar spectrum. *Figure 2-3(b)* illustrates this point.
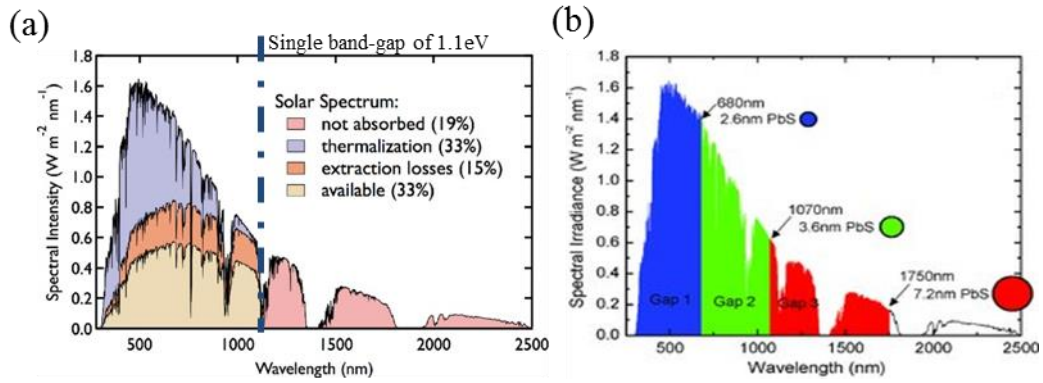
Figure 2-3. (a) The solar spectrum - showing the effect of Shockley–Queisser limit on a solar cell with a single semiconductor active material of band gap 1.1eV. Only a maximum of 33% efficiency can be attained. Figure adapted from reference[18] (b) A similar diagram showing the benefit of having a multiple band gap device. By using quantum dot of different fixed sizes, a greater part of the solar spectrum could be harnessed. Figure obtained from reference[16].

2.2.2 Operational principle of solar cells

The electronic nature of a CQD solid film is different from a bulk semiconductor, where a spatial continuum of the conduction and valence energy bands exists. For CQD solids, the energy band concept can be approximated, with the idea that individual exciton wavefunctions associated with each dot could overlap to form a "band". This concept allows us to simplify our understanding and serves as a basis from which electronic properties of a CQD solid could be examined and correlate to device performance. Further, using this approach allows the emulation of existing technologies of silicon and other bulk material solar cells and to adopt similar architectures, for example a *p-n* junction solar cell and Schottky solar cell, but with the bulk materials replaced with quantum dot films (see *Figure 2-4(a)*) . With a sequential reference to a simple *p-n* junction presented in *Figure 2-4(b)*, the photovoltaic action could be briefly described as follows:

(1) Upon absorption of incident photons with energy larger than the band-gap of the active material, electron-hole pairs are created.

(2) These photogenerated charges will be transported by drift in the depletion region which is a result of a built-in electric field across a junction, or by diffusion in quasi-neutral regions.

(3) The depletion region is a result of charge and Fermi-energy equilibrium between a *p* and *n* type semiconductor, leading to band-bending and giving rise to the built-in potential and electric field.

(4) The photovoltaic action is completed when photogenerated charges get collected at their respective electrode

(5) Alternatively, carriers can be slowed by shallow trap states or completely lost at deeper traps known as recombination centres, where an electron and hole recombine via non-radiative processes before they can be successfully extracted.
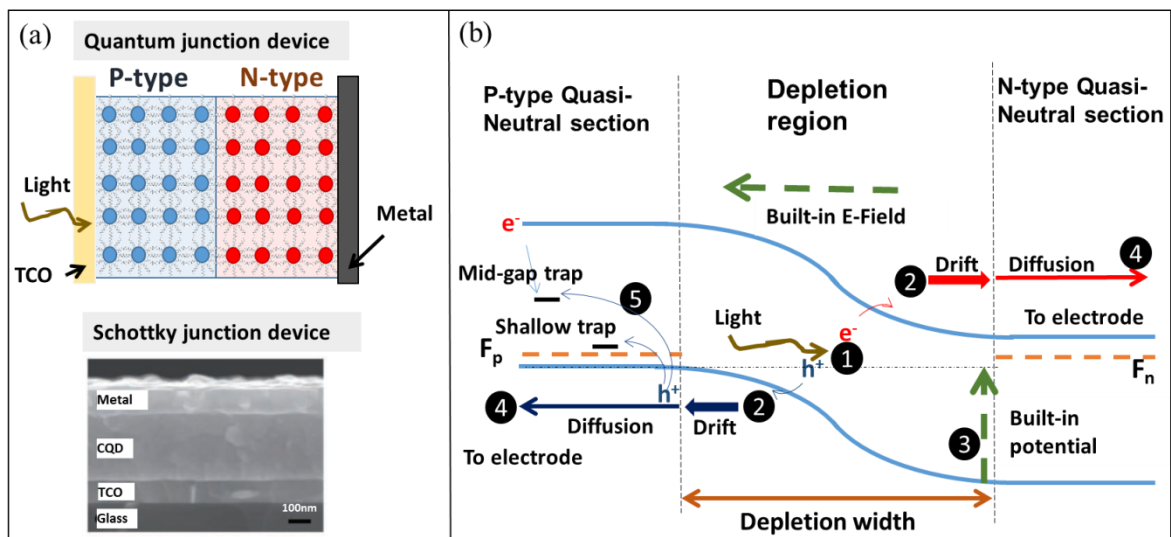
Figure 2-4. (a) Top: A diagram depicting a p-n junction solar cell made up of p-type and n-type CQD films sandwiched between a metal electrode and a transparent conducting oxide (TCO).

Bottom: A cross-section scanning electron microscopy image of actual CQD Schottky device, wherein the metal acts as both the junction and an electrode. (b) The corresponding band diagram and the illustration of the photovoltaic effect. F_p and F_n refers to the quasi-Fermi energy level of the p-type and n-type semiconductor material respectively.

The depletion width, *W*, of a *p-n* junction is dependent primarily on the doping densities of the *p* and *n* type material and is given by:

$$W = \sqrt{\frac{2\varepsilon_r\varepsilon_0}{q}\left(\frac{N_A+N_D}{N_A N_D}\right)(V_{bi} - V)} \qquad\qquad \text{Equation 2-2}$$

where N_A and N_D are the doping densities of the *p* and *n* type material respectively, *q* is the elementary charge, ε_r is the dielectric constant and ε_o is the permittivity of free space. V_{bi} is the built in potential, determined by the Fermi level positions of the *p* and *n* type material, F_p and F_n by:

$$V_{bi} = \frac{(F_n - F_p)}{q} \qquad\qquad \text{Equation 2-3}$$

2.2.3 Characterisations of solar cells

2.2.3.1 Current-voltage analysis

The power conversion efficiency, η, of a photovoltaic device is determined by the ratio of maximum area-normalized electrical output power over the intensity of incident light. This is given by:

$$\eta = \frac{V_m \cdot J_m}{I_{in}} = \frac{V_{oc} \cdot J_{sc} \cdot FF}{I_{in}} \qquad\qquad \text{Equation 2-4}$$

where V_m and J_m are the voltage and current density at the maximum power point, I_{in} is the incident light intensity, V_{oc} is the open-circuit voltage, J_{sc} is the short-circuit current density and *FF* is the fill factor.
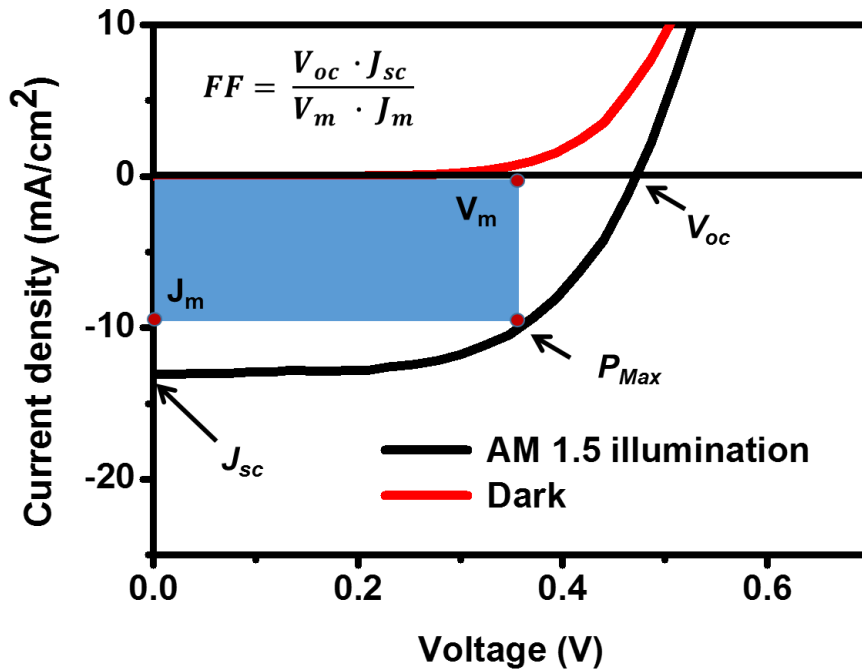
Figure 2-5. A typical experimental result showing current density-voltage response of a solar cell in dark and illuminated conditions.

These performance indices that determine the overall device efficiency can be collated via a simple current density-voltage trace as shown in *Figure 2-5*. J_{sc} is the maximum number of photogenerated carriers per unit area that are extracted from the solar cell and depends on the incident light intensity, the total photon absorption by the active regions of the solar cell and any recombination losses prior to extraction. The V_{oc} is the maximum potential difference that a solar cell can generate which results from the difference between the quasi-Fermi level of the *n*-type and *p*-type material. The band gap of the active material and trap states which result in non-radiative recombination affects V_{oc}. *FF* indicates the quality of current-voltage characteristics and it depends on the ability of charges to reach the electrodes which is governed by recombination processes. The maximum power point, *Pmax*, and the "squareness" of the *J-V* graph determines *FF* and it is given by:

$$FF = \frac{P_{max}}{V_{oc}J_{sc}} = \frac{V_m J_m}{V_{oc}J_{sc}} \qquad \qquad \textit{Equation 2-5}$$

The concept of fill factor will be reinforced in chapter 7.

2.2.3.2 External quantum efficiency (EQE)

EQE is another measure of photovoltaic device performance. It allows one to determine how exactly efficient is one photon of a particular wavelength in generating an electron-hole pair and then successfully collecting them at their respective electrodes, thereby registering a photogenerated current. Examining this one photon to one electron (and hole pair) quantum process at discrete wavelengths against the absorption profile provides more details on charge collection efficacy across the device. EQE takes into account the effect of optical loss processes such as transmission and reflection. The short-circuit current density generated by the solar cell can also be calculated using EQE by[25]:

Equation 2-6

$$J_{sc} = q \int b_s(E) EQE(E) dE$$

where $b_s(E)$ is the number of photons incident, per unit area and per unit time, of energy in the range of E to $E + dE$ and q is the elementary charge.

Figure 2-6 shows an annotated EQE data plot that is characteristic of PbS CQD solar cell.
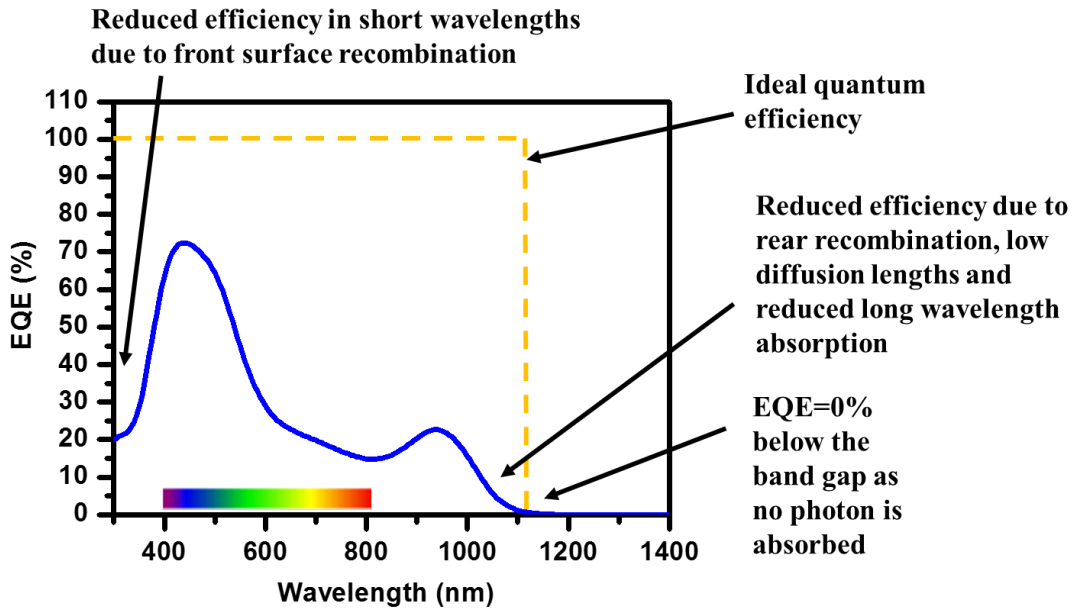
Figure 2-6. An annotated EQE data plot of a typical PbS CQD solar cell. The mean band gap of PbS CQD film is 1.33 eV (930 nm in wavelengths). The higher wavelength peak corresponds to the exciton peak absorption of the PbS and the shorter wavelength is the second order exciton peak, which is higher because the higher energy excitons, that result from the absorption of high energy photons, have longer diffusion length and thus have a greater collection efficiency.

2.2.4 Operational characteristics of solar cells

The characteristic operation of a solar cell can be approximated as a current source working against a diode. Under illumination, the overall current can be thought of as the superposition of the short circuit current generated by photon absorption and a reverse current caused by the potential built-up under load. This reverse current is also known as the dark current and it is given by:

$$J_{dark}(V) = J_0(e^{\frac{qV}{nkT}} - 1)$$
<div align="right">*Equation 2-7*</div>

where J_0 is the reverse saturation current density and it a measure of carrier recombination in the diode, q is the elementary charge, V is the voltage between the cell terminals, k is the Boltzmann constant and T is temperature. n is the diode ideality factor which is dependent

on recombination mechanism. $n = 1$ if recombination is band to band and only limited by the minority carriers, while $n = 2$ if it occurs in the depletion region and both carriers limit recombination[25]. The superposition principle then gives the total current density from a solar cell device under illumination to be:

$$J(V) = J_{sc} - J_0(e^{\frac{qV}{nkT}} - 1) \qquad\qquad \textit{Equation 2-8}$$

At open-circuits conditions, $V = V_{oc}$ and $J = 0$. Rearranging the equation gives:

$$V_{oc} = \frac{kT}{q} ln \frac{J_{sc}+J_0}{J_0} \approx \frac{kT}{q} ln \frac{J_{sc}}{J_0} \qquad\qquad \textit{Equation 2-9}$$

This highlights the relationship between open-circuit voltage and reverse saturation current density J_o. To improve V_{oc}, carrier recombination in the quasi-neutral region should be kept low and this corresponds to a highly rectifying diode-like characteristic in the dark. However, one must proceed with caution when applying these diode models to colloidal quantum dots solar cells because these are developed based on conventional *p-n* junction solar cells.

Nevertheless, for real solar cell devices, considerations must be given to parasitic series resistance R_s and shunt resistance R_{sh}. The following equation shows the modification made when parasitic resistances have been taken into account:

$$J(V) = J_{sc} - J_0 \left(e^{\left(\frac{q(V+IR_S)}{nkT} \right)} - 1 \right) - \frac{V+IR_S}{R_{sh}} \qquad\qquad \textit{Equation 2-10}$$

The series resistance R_s reduces J_{sc} and overall output current, while the shunt resistance R_{sh} reduces the V_{oc}. R_s is closely related to carrier transport resistance, while R_{sh} is linked to shunt paths and carrier recombination loss. More importantly, *FF* is also related to R_s

and R_{sh}. A lower R_s and a larger R_{sh} leads to a larger *FF,* with a concomitant improvement to V_{oc} and J_{sc}, and hence better power conversion efficiency, η. For PbS CQD solar cells, devices are often limited by lower V_{oc} and *FF* values.

2.3   Electronic transport in CQD solids

2.3.1   Mobility and lifetime

Optimization of CQD device performance involves meeting the antagonistic demands of effective light absorption versus efficient charge extraction. As an illustration, in a device with active material of thickness 1 μm, an absorption coefficient at the band gap in the order of 10^4 cm^{-1} (more exactly: 2.3×10^4 cm^{-1}) is required to absorb 90% of incident photons at the band gap of CQDs assuming no reflection losses[16]. If the thickness were increased for greater optical depth so as to ensure complete photon absorption, there could be a drop in charge collection efficiency because charge carriers are prone to be lost through recombination if the lifetime is shorter than their transit time. Lifetime refers to the average time a photogenerated carrier is free to move before recombination occurs.

The speed at which a carrier moves by drift is described by the drift mobility μ, which can be thought of as the velocity of the charge carrier under the influence of an electric field. Together, mobility μ, electric field E and lifetime τ are related by drift length, L_{drift}, as in:

$$L_{drift} \ = \ \mu \, E \, \tau \qquad\qquad \textit{Equation 2-11}$$

Diffusion, on the other hand, is characterised by the diffusion length, L_{diff}, as in*:*

$$L_{diff} = \ \sqrt{D \, \tau} \qquad\qquad \textit{Equation 2-12}$$

where D is the diffusivity and is governed by the Einstein relation:

$$\frac{D}{\mu} = \frac{kT}{q}$$

<div align="right">Equation 2-13</div>

The sum of drift and diffusion lengths gives an approximation as to how thick the active layer should be designed in a solar cell device. Drift transport is much more efficient and covers a longer range before charge recombination sets in. Therefore, one would typically want to maximise the depletion width in a device and this requires controlled doping of materials that form the junction. However, maximising depletion width is not the only facet to improving charge transport: reducing the density of trap states, which are abundant in CQD solids, is another important aspect.

Traps that are deep and lie near the middle of the band gap act as recombination centres, resulting in the loss of charge carriers before they can be extracted at the electrodes. Shallow traps are less detrimental: although they lower the mobility of carriers non-radiative recombinations are less likely to happen as trapped carriers can acquire energy easily again to be re-excited into conduction/valence band. An example pertaining to PbS CQD is described by Tang et al.[26] Hence, the implication for CQD films in solar cell devices is that the charge carrier transport characteristics should be improved so as to be able to make thicker active layers to enhance absorption without compromising charge collection efficacy. Still, charge transport is not straightforward in nanostructured systems and to make improvements requires knowledge on the transport mechanism in CQD solids. Attempts have been made to formalise the transport phenomena into theories and these will be discussed in the next section.

2.3.2 CQD Transport theories

A few theories have been proposed to describe charge separation and charge conduction in CQD based devices. The foundations were laid by Mott[27], Efros, Shklovskii[28,29] and others,

but these early theories have only been experimentally verified on CQD films available at those times, that are highly disordered by today's standards— due to large variance in particle size. The recent developments in the synthesis of monodisperse CQDs, together with the capability to change bulky ligands for more compact ones, has led to the expansion of transport theories.

Broadly, there are two major proposed mechanisms. The first (*Figure 2-7(a)*) is termed hopping, by which the charge conductivity derived follows an Arrhenius type dependency. Mott introduced "Variable Range Hopping" (Mott-VRH)[27] to describe a low temperature regime of conduction in strongly disordered systems with localized states[30]. Nearest neighbour hops are ideal but hops to a further site with less energy difference may be more favourable and this long range transport also contributes significantly to conduction. Efros-Shklovskii variable range hopping (ES-VRH) was later developed[28] and takes into account the Coulomb gap and charging energy.
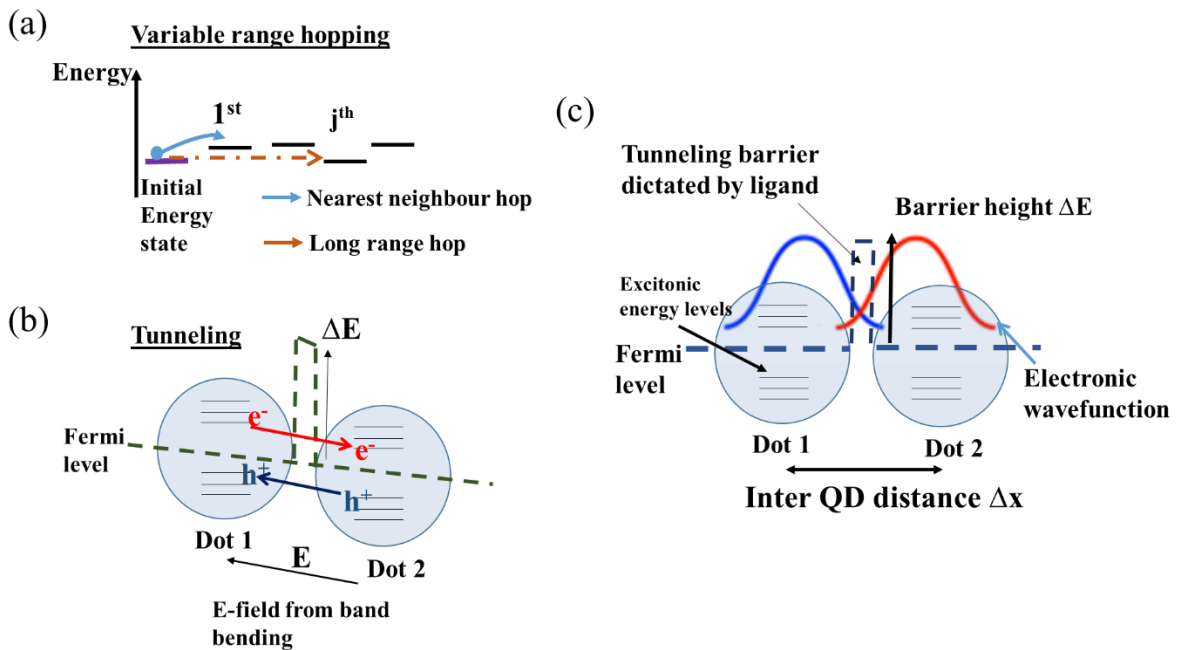
Figure 2-7. (a) Diagram showing nearest neighbour hop and a long range hop - further distance but with a similar energy level. (b) Tunnelling in the direction favoured by the direction of internal

electric field. (c) The idea of coupling between neighbouring CQDs. The extent of wavefunction

overlap is dependent on barrier height and interparticle spacing.

The second mechanism is tunnelling (*Figure 2-7(b)*) and unlike hopping, it is temperature-independent. The concept of tunnelling for quantum transport requires the understanding of coupling energy *β*, between two neighbouring CQDs (*Figure 2-7(c)*). Coupling energy describes the extent to which wave functions of neighbouring states overlaps and hence, the extent of exciton delocalisation[31–33]. It is given by:

$$\beta \approx \Gamma/h \qquad \qquad \textit{Equation 2-14}$$

where *h* is Planck's constant and *Γ* is the tunnelling rate, which can be approximated as in[34]:

$$\Gamma \approx \exp \{-2 \cdot (2m^*\Delta E/ \hbar^2)^{1/2} \cdot \Delta x\} \qquad \qquad \textit{Equation 2-15}$$

where *m** is the carrier effective mass, and *ΔE* and *Δx* are the height and thickness of the tunnelling barrier. It is apparent that coupling and eventually tunnelling rate, decreases exponentially with nearest neighbour distance *Δx*.

2.3.3 Factors affecting transport

From the transport mechanisms, it is evident that interparticle spacing and energetic coupling greatly affect the ease of conduction of charge carriers and hence their mobility. These factors can be altered by changing the surface ligands of CQDs. Another crucial element is energy disorder ($\Delta\alpha$). Absolute monodispersity in nanocrystal size is virtually impossible to achieve. Even with current synthesis techniques which allow for dispersion to within a single atomic layer[35], this amounts to a standard deviation of a few percent. Size distribution results in the finite dispersion of the orbital energies *α*, due to quantum confinement that, scales approximately with $1/r^2$, with *r* as the radius of particle[36]. This leads to a finite disorder of $\Delta\alpha/\alpha \approx 2\Delta r/r$ in site energies. The smaller the disorder, the

more efficient the processes of charge transfer amongst CQDs due to better alignment of neighbouring energy states and hence, a more effective energetic coupling amongst an array of CQDs. This highlights the significance of a narrow size distribution of individual CQDs.

The last factor is charging energy E_c, which is also referred to as the self-capacitance[37]. In its simplest form for spherical particles, charging energy is inversely related to the radius r and the permittivity ε of the surrounding medium, and proportional to the square of charge e, as given by:

$$E_c = \frac{e^2}{4\pi\varepsilon r}$$

Equation 2-16
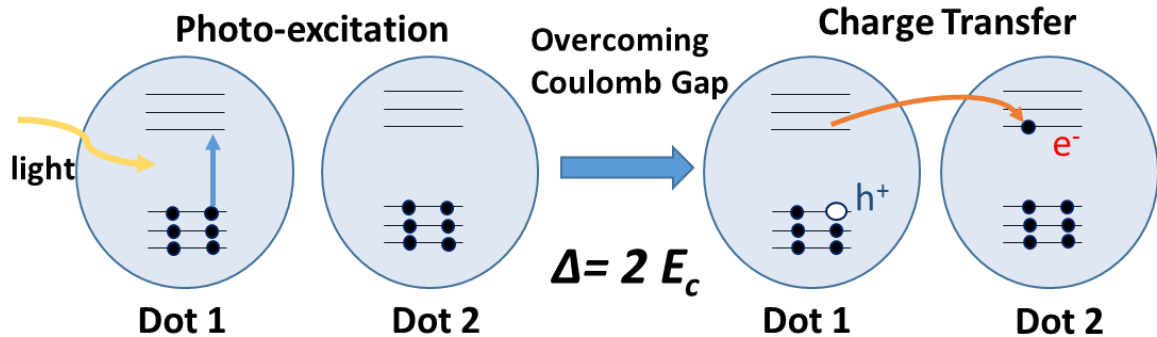
Figure 2-8. A schematic diagram explaining the Coulomb Blockade effect. Coupling energy must be sufficient to overcome charging energy to enable facile charge transfer.

E_c is an energetic penalty for removing or adding a charge on a system and for a CQD where size is small, E_c becomes significant. In an array of weakly coupled CQDs, the charging energy creates the Coulomb energy gap $\Delta \approx 2E_c$, which quashes conduction undern low-bias . This effect is known as the Coulomb blockade[38] (*Figure 2-8*). For effective charge delocalisation to occur, the coupling energy β must be greater than E_c.

Using *Equation 2-15*, keeping the size of quantum dot fixed, the only way to improve charge delocalization is to alter the permittivity or dielectric constant of the surrounding medium. In a CQD solid, the surrounding medium refers to the ligands which could be altered by ligand exchange. *Figure 2-9* shows the relationship between factors that affect effective charge delocalisation and hence the ease of charge transport in a CQD solid.
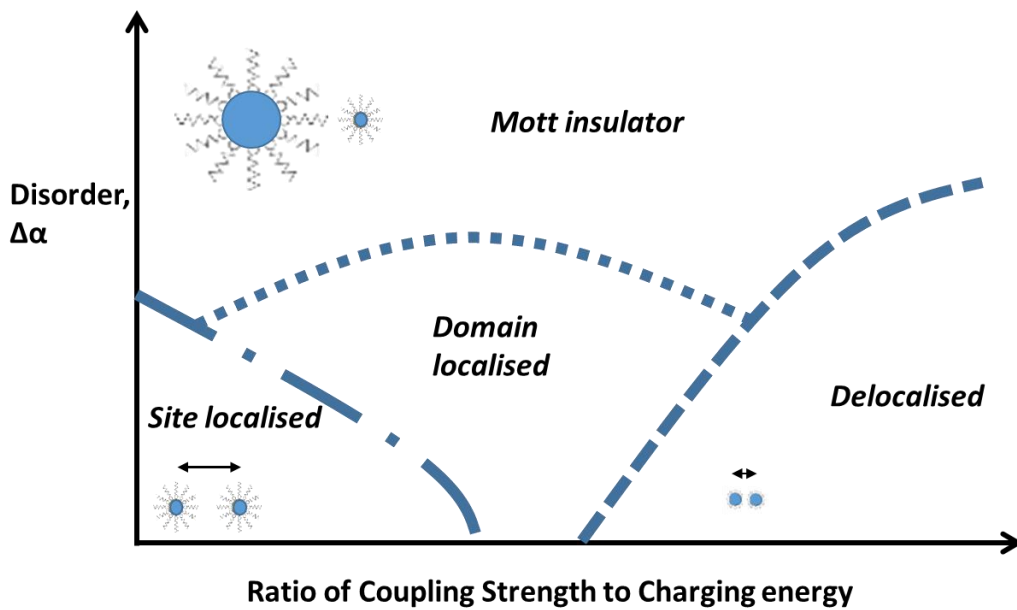
Figure 2-9. A conceptualised electronic transport phase diagram based on the factors of energy disorder, coupling strength, charging energy as well as interparticle spacing. Adapted from reference[39]

2.4   Using CQD in solar cells

2.4.1   PbS as a material of choice for CQD solar cell

Lead chalcogenides (PbS, PbSe and PbTe) have a narrow bulk band gap, which absorbs infrared wavelengths as long as 3000 nm. However, they have a large Bohr radius, for example PbS is 18nm, which makes it possible to tune the band gap absorption wavelength from 3000 nm to about 600 nm, by simply controlling the size of quantum confined PbS CQDs. This makes them a group of very versatile materials and their band gap tunability

provides opportunity for creating multi-junction/tandem solar with other materials or even with itself. The focus of this thesis is placed on PbS, primarily because it is more air stable than PbSe and PbTe, and it is the most well-established quantum dot material in terms of device performance as processing technologies. PbS CQDs prepared by the hot injection route have been shown to possess a long-term photophysical stability of over four months of storage in a freezer (-20 °C) without any inert gas protection[40]. In the next section, the various ways in which PbS CQD could be incorporated into solar cell devices are discussed.

2.4.2 The evolution of PbS CQD employment in solar cells
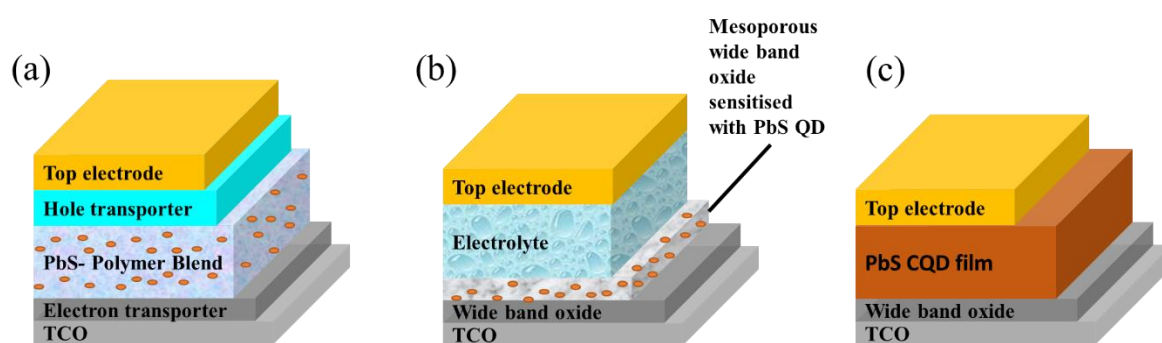
Figure 2-10. (a) PbS:polymer blend solar cell and (b) PbS sensitised solar cell. Both (a) and (b) makes use of increased interfacial area between PbS CQD and another material to improve charge extraction. (c) PbS CQD used as both the light absorber and charge transporter.

In the initial stages of CQD technology, the knowledge of ligand chemistry and surface treatment of quantum dots was limited. As such, the transport properties of PbS CQDs were limited and therefore early efforts of utilizing PbS CQD in solar cells were restricted to the role of light absorber, producing photogenerated charges that are then passed to a polymer matrix in the case of PbS:polymer blends or acting as a sensitizer on a mesoporous wide band oxide like titania (*Figure 2-10(a)* and *(b)*). In both cases, PbS CQD were exploited for light harvesting properties while the device architecture aids in accommodating its poor charge transport properties. However, in the last 10 years or so, there has been a tremendous

improvement in quantum dot film processing, device physics and material chemistry such that PbS CQD film could be utilised as both the main light absorber and charge transport material (*Figure 2-10(c)*). In this thesis, the emphasis is placed on this particular approach.

2.5   Conclusion

For a functioning solar cell, two fundamental processes have to take place: Charge generation from light absorption and the process of separating, transporting and extracting photogenerated electron-hole pairs. From a device standpoint, higher power conversion efficiencies imply a need for improved FF and improved V_{oc} (from lowering carrier recombination), especially for PbS CQD devices. Then from the CQD perspective, performance improvement could be warranted from improving charge transport in PbS CQD film. In the next chapter, a review will be given on the progress of PbS solar cell technology in the aspects of synthesis, surface chemistry and device making.

Chapter 3 – Literature review

3.1 Developments in PbS CQD synthetic chemistry

3.1.1 Monodispersity

Below 18 nm, the diameter of a PbS quantum dot influences its band gap and it was discussed in section 2.3.3 that the smaller the size distribution of CQD packed in a solid film, the larger the extent of coupling that would aid charge transport from dot to dot and eventually across the film. Furthermore, different size PbS CQD would encourage recombination due to differing energy levels below the mean band gap acting as trap sites. Zhitomirsky *et al.* showed by simulation and by fabricating actual devices that a standard deviation of 150 meV or less is optimal for device performance[41], which is very much achievable by current synthetic approaches.

The most common method to produce photovoltaic quality PbS CQD to date is the hot-injection protocol developed by Hines and Scholes[42]. This method is very precise and reproducible, as shown by Zhang *et al*[43]. Although PbS CQD synthesis protocol is confined to the laboratory scale, Pan *et al.* have recently demonstrated that it is possible to modify this procedure to a dual stage batch process which accommodates a large scale PbS CQD production without any compromise to quality[44]. Other research efforts have been geared towards avoiding the highly reactive and potentially dangerous sulphur precursor, bis(tri-methylsilyl) sulphide ($(TMS)_2S$), and instead relied on elemental sulphur[45–47].

Nevertheless, despite the high level of monodispersity achieved, to date, the V_{oc} of PbS CQD devices is limited to below half its band gap value[48]. Zhitomirsky *et al.* argued that V_{oc} improvement from monodispersity would only be significant if PbS surface defect/trap

density is reduced[41]. This highlights the importance of surface passivation for better device performances.

3.1.2   Size control and size effect

On another front, there was a better understanding of the size effect on PbS CQD chemical stability. Intriguingly, PbS CQD's stability[49,50] has been found to vary with its size[51]. While often portrayed as solid spheres, nanocrystals actually have a highly faceted structure, inherently owing to their crystallography. Small PbS CQDs have been reported to have a higher Pb:S ratio compared with the more faceted large PbS CQDs. In contrast, large PbS CQDs are more faceted and they include exposed {111} facets consisting of sulphur anions not protected by common ligands like thiol and carboxyl-terminated ligands (*Figure 3-1(a)*). Therefore, oxygen and other reactive species can easily attack these vulnerable {111} surfaces.

The study of such a surface reaction is made possible by X-ray Photoelectron Spectroscopy (XPS), which shows the distinction between large and small PbS CQDs: $PbSO_3$ is the main oxidation product for small PbS CQDs, which gives a shallow trap state of 0.1 eV [52,53] while that of large PbS CQDs is $PbSO_4$, constituting a deeper midgap state, responsible for performance degradation[49]. These observations were further corroborated by Choi *et al.* as he synthesised batches of PbS CQD with diameters ranging from 1.5 nm to 7.5 nm and studied their composition, stability against oxidation, and shape evolution as size decreases[54] (*Figure 3-1(b)*). Furthermore, the stability of CQDs were characterized by the extent of blue-shifts of the PbS excitonic absorption peaks, which was attributed to surface oxidation[55,56], and this was shown to increase with decreasing PbS CQD size (*Figure 3-1(c)*).
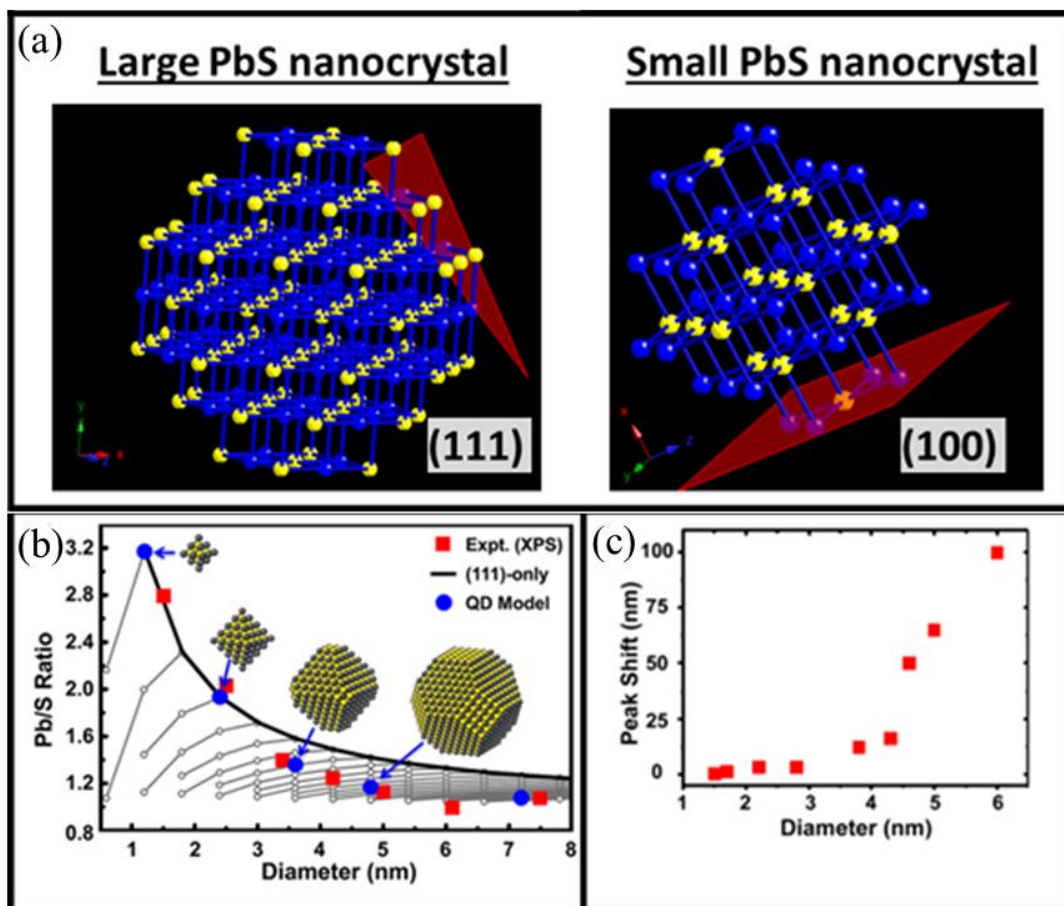
Figure 3-1. (a) Nanocrystal models created, using crystal maker software, depicting that larger PbS nanocrystals having more (111) facets which contain unterminated sulphur atoms, as compared to smaller nanocrystals. (b) Graph showing the relationship between the size of PbS CQD, its crystalline shape and cation to anion ratio, both simulated and backed by experimental data. (c) Plot revealing the size-dependent stability of PbS CQD to oxidation. The extent of the peak shift represents the amount of oxide shell formed on the PbS CQDs. (b) and (c) are reproduced from reference[54].

Therefore, the implication is that, in principle, the stability of a CQD and its surface passivation could be managed with materials engineering. Vulnerable crystal facets could potentially be avoided by synthesising smaller PbS CQD, or even by developing a passivating strategy that binds to both cations and anions on the surface of CQD. However, the route of using smaller PbS CQD was shown to be counterproductive (see *Figure 3-2*).

Choi *et al.* and Yoon *et al.* both independently showed that Schottky solar cell devices with smaller PbS do give higher V_{oc} due to the increasing band gap[57,58], however, with increasing band gap (or decreasing PbS CQD size) the J_{sc} decreases due to (i) less light being absorbed and (ii) higher series resistance due to greater number of inter-QD hops that carrier has to make to travel across the same QD film thickness. Choi *et al.* evaluated that the stability towards oxidation only becomes apparent when PbS CQD size is of 3 nm (which equate to about 1.3 eV) or below[54]. Therefore, PbS CQD should optimally be around this size to reap the benefit of both oxidative stability and a band gap size to capture a reasonable portion of the sunlight.
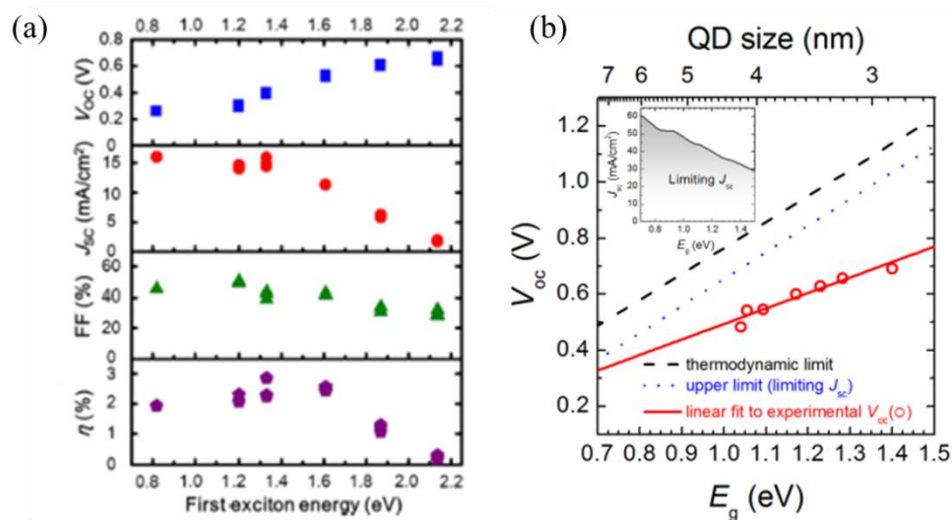
Figure 3-2. (a) Device performance metrics of Schottky solar cells against the size of the PbS CQDs used. In this study the optimal band gap is found to be about 1.3 eV. Figure reproduced from reference[57]. (b) Generalised relationship between band gap and experimental V_{oc}, theoretical V_{oc} (limited by maximum of J_{sc}) and thermodynamical V_{oc}. Graph and insert shows that it is unwise to gain V_{oc} by increasing band gap for the gain in V_{oc} is limited while the higher band gap suffers a loss in J_{sc}. Figure reproduced from reference[58].

3.1.3 In-situ surface treatment

Yet another less common PbS CQD synthesis method is one that utilises a lead chloride source and this technique was first developed by Cademartiri and Ozin[45]. Moreels *et al.* later showed that this method could be adapted to produce PbS size ranges that the Hines and Scholes' protocol is capable of[47]. A further step was taken by Zhang *et al.* who studied the effect of using different lead halides for synthesis and they showed that the halide atoms are incorporated onto the synthesised PbS CQD[59]. Especially for the case of chlorides, the PbS product gave higher PL yield. They further report incorporating the as-synthesised PbS CQDs into devices, which gave better device performances and higher stability as compared to controls. This was understood as a way to treat and protect the surface of PbS CQD during the synthesis stage. Another unique approach is the use of metal chloride treatment during synthesis. First reported by Ip *et al.*, where cadmium chloride was introduced during the growth stage of the synthesis process, it was shown as a method to ensure extensive trap mitigation as the small size of the halide atom is able reach trap sites that are not easily reached by bulkier organic ligands (*Figure 3-3(a), (b)*)[60]. It was later generalised as a metal chloride treatment where this time, different metal cations have been studied (*Figure 3-3*) and it was found that the metal cation is important in influencing the final energy states of PbS CQD and therefore influences trap passivation[61–63]. Recent works from Zhang *et al.* followed by Crisp *et al.* showed the benefit of using both cation and anionic passivation by using lead chloride for a cadmium sulphide to lead sulphide (and also cadmium selenide to lead selenide) cation exchange synthesis procedure[62,64]. It was argued that the cation exchange process leaves behind a certain amount of cadmium and chloride left in the resultant PbS (and PbSe) CQD and devices made from the as synthesised CQD showed better device performance and stability (*Figure 3-3*). In the following section, passivation is discussed at the device processing level.
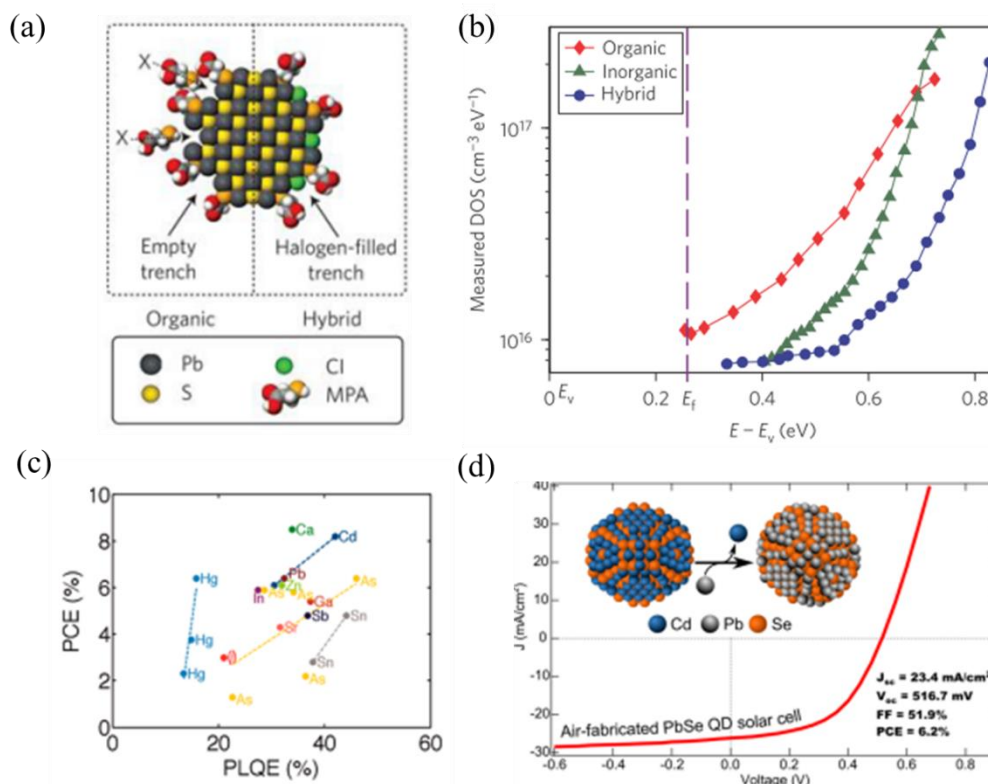
Figure 3-3. (a) Pictorial representation of the hybrid passivation. Chlorine atoms were introduced at the synthesis stage while oleic acid is replaced by MPA at the film fabrication stage. Chlorine atoms are able to passivate "trenches" that are hard to reach. (b) Graph indicating better trap passivation by using a hybrid ligand exchange strategy. (c) The effect of different metal cations of metal chloride used in synthesis as a treatment procedure. Better PLQE is an indicator of better trap passivation. (d) Cation-exchanged PbSe (from CdSe) showing remarkable performance and stability and this same strategy was used for PbS solar cells[62]. (a) and (b) are obtained from reference[60] while (c) is from[61] and (d) is from[64].

3.2 Progress in surface ligand chemistry and CQD film processing

3.2.1 The ligand exchange process

CQD surfaces have to be well passivated and protected from oxidative attacks and colloidal aggregation. Yet, in order for PbS CQDs to be useful as a photovoltaic active material, long ligands attached to the CQD after synthesis needs to be replaced by smaller ones so as to

improve the conductivity of CQD film. There are two general approaches in which ligands can be substituted and they are pictorially illustrated in *Figure 3-4*. The first approach (*Figure 3-4(a)*) is termed solid-state ligand exchange and involves replacing the native ligands only after casting the CQD film. The second approach (*Figure 3-4(b)*) is termed solution-phase ligand exchange and it involves swapping the long native ligands for shorter ones while the CQDs are still suspended in a solution.
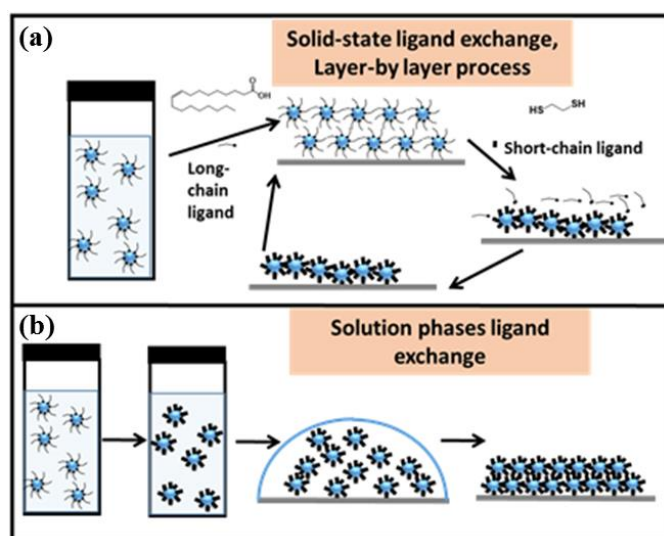
Figure 3-4. Pictorial representation of the ligand exchange approaches: (a) solid state ligand exchange (b) solution phase ligand exchange.

Solid-state ligand exchange is a more established method and is usually integrated into the device fabrication process, for example with spin coating or dip coating. The crux of the method is the formation of a thin film of CQD on a substrate, followed by the introduction of the replacement ligands and the washing away of excess and exchanged ligands. However, due to the fact that the replacement ligand is much shorter than the native one, the entire film would experience significant volume shrinkage, resulting in macro defects such as cracks and voids. This is remedied by using a layer-by-layer approach – the process of film deposition and ligand exchange is repeated several times until the desired thickness is achieved, with each new layer filling in the voids of the previous layers. This layer- by-

layer casting and ligand exchange approach is still the most established method and it is used to make the best devices reported in recent times[65,66].

While this technique seems attractive, it is dependent on exchange kinetics and in certain cases the exchange rate is slow. As an example from Tang *et al.,* the ligand cetyltrimethylammonium bromide (CTAB) exchanges slowly with oleic acid. By putting copious amount of ligand solution over the film and allowing the solution to stand for a minute before washing it off, and then by repeating the procedure twice more, they showed that this would ensure complete exchange before the next layer of CQD is deposited[67]. While this technique is relatively reproducible in laboratory conditions, its scalability is questionable. For example, in a roll-to-roll production line, a layer-by-layer approach would be time consuming and costly (*Figure 3-5(a)*).

The second approach is conceptually more ideal as a solution phase exchange ensures adequate time for complete and thorough ligand exchange. The number of deposition cycles of CQD layers could be reduced as voids would less likely be formed and this would lead to lesser material wastage compared to a layer-by-layer procedure (*Figure 3-5(a), (b)*). Unfortunately, this procedure has its fair share of limitations when forming solar cell devices. First, the replacement ligands are smaller and so do not stabilize the colloidal state of the solution very well. Extra care must be taken with solution purity, inertness of the environment and temperature, especially with long exchange times, to avoid unwanted oxidation or contamination. Also, these small ligands are labile, and might be lost during the coating process, forming new defects and energetic disorder. One of the first few examples of using this approach is a work done by Johnston *et al.,* in which oleic acid was swapped for butylamine in PbS CQD[68]. The exchanged PbS CQD is re-dispersed in toluene, which is used to fabricate a Schottky junction solar cell. The device gave an AM1.5 efficiency of 1.8 % and a monochromatic efficiency on 4.2 % at 975 nm with a 12 mW/cm^2

intensity. However, it was reported that the devices were stable for only 4 hours and were completely degraded when left out in ambient air for a day. There have been various solution phase ligand exchange procedures reported since then, with metal chalcogenide complexes, chalcogenides, metal halides and even psuedohalides as the exchanging ligands but these studies have no reports of using the exchanged PbS CQD for solar cell devices. A significant milestone was reached when Fischer *et al.* reported the use of thioglycerol as a ligand[69]. PbS CQD was successfully transferred from the octane phase to dimethyl sulphoxide (DMSO) phase and then was separated and used for solar cell device fabrication. However, due the low volatility of DMSO, a non-conventional CQD film casting method was used and it requires mild heating under low pressure condition for hours. Furthermore, device efficiency is at best 2.1 %. Even though the results are not remarkable, this work serves as a proof of concept that a direct one-step deposited PbS could result in a working solar cell device.
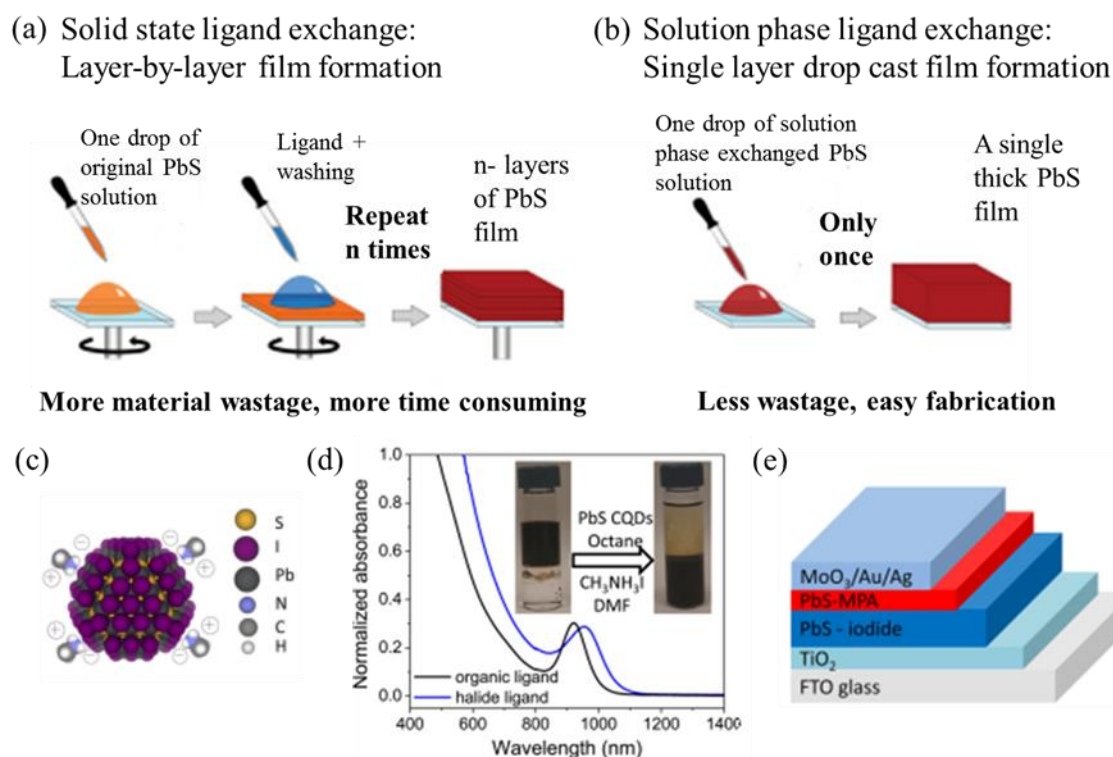
Figure 3-5. (a) , (b) Schematic diagrams showing the difference between the two film fabrication processes and the possible benefits of using solution phase ligand exchanged- CQD solution. (c) A PbS CQD model depicting iodide ligands passivating the Pb rich PbS CQD surface and the methylammonium counterion balances the overall charge. (d) Absorption curve showing the presence of PbS CQD exciton peak before and after ligand exchange, which exclude any possibility of CQD aggregation during the process of ligand exchange. The slight redshift however, is due to stronger coupling between CQD due to closer proximity between CQD with the smaller sized iodide ligands. (e) The device architecture which incorporates the iodide exchanged PbS CQD. (a), (b) are figures adapted from reference[69] while (c)-(e) are obtained from reference[70].

A huge progress was made recently, where iodine was used as a passivating ligand. Introduced as methylammonium iodide, PbS CQD was transferred into dimethylformamide (DMF) solvent as stabilized by iodide ligand[70]. This exchanged-PbS was cleaned and then re-dissolved in butylamine to give a highly concentrated volatile colloid which could be deposited by spin coating. Device fabrication was not only simplified but devices were air-stable and the best devices were reported gave a power conversion efficiency of 6.1 % (*Figure 3-5(c)-(e)*).

3.2.2 Types of ligand

The most obvious intention for employing ligand exchange is to decrease the inter CQD distances, thereby improving charge mobility. Talapin *et al.* investigated the effect of swapping oleic acid ligands for hydrazine on PbSe CQD film, showing experimental evidence of the reduction of interparticle spacing and a 10-fold increase in conductance, measured from FET experiments[71]. Similarly, Guyot-Sionnest *et al.* showed that by replacing trioctylphosphine oxide ligands with 1,4-phenylenediamine, cadmium selenide CQD's conductivity by three orders of magnitude[72]. Furthermore, Liu *et al.* showed a direct

experimental observation of ligand length to carrier mobility in lead selenide (PbSe) nanocrystal solids[73] and this is illustrated in *Figure 3-6*.
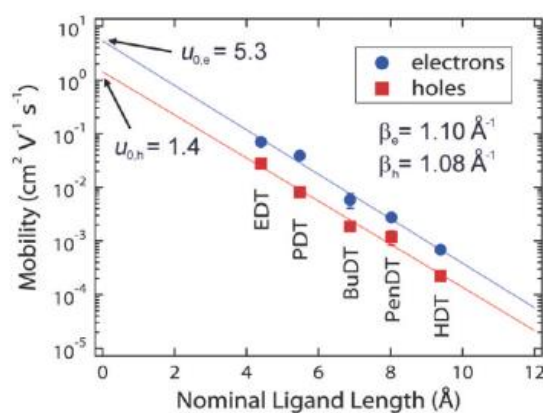
Figure 3-6. Carrier mobility showing an exponential dependence on ligand length. Mobility is extracted from Field Effect Transistor studies of PbSe CQD Films. Reproduced from reference[73].

Bi-functional ligands are one of the top choices for ligand replacement when it comes to device fabrication. These organic molecules could bind to one CQD and also a neighbouring CQD, which effectively reduces interparticle spacing, making a very compact CQD film. The downside is that they could only be used in a solid state exchange process because applying them in solution causes the CQDs to aggregate. Also, the process generates voids in the film as the exchange of long ligands for shorter ones creates huge volume shrinkage, thus necessitating a layer-by-layer film formation approach. Nevertheless, their usage is quintessential for most of the current best performing PbS CQD solar cell devices[65,66].

Table 3-1. Classification of ligands used for the stabilization and passivation of CQDs as reported in the literature.

Ligand type	Example	Characteristics/Function	Best efficiencies	References
Long chain organic	Oleic acid, Trioctyl phosphine	-Carbon chain length > 8 -Stabilizes CQD via steric repulsion -Used as a surfactant in CQD synthesis	None (CQD films are too insulating with long chain organic ligands)	
Short chain organic	Pyridine, butylamine, Hexanethiol	-Reduces inter CQD distances	1.8 % with butylamine (AM1.5) 2.6 % with ethanthiol (76 mW/cm^2 at 1 μm)	[68,74]
Bi-functional organic	1,2-ethandithiol (EDT), 3-mercaptopropionic acid (MPA)	-Reduces inter CQD distances to a greater extent with inter CQD attachment	9.2 % with MPA	[66]
Metal complexes	-Metal chalcogenide complexes like $(Sn_2S_6)^{2-}$ -Halometalate complexes like PbI_3^- and $CdBr_3^-$	-Reduces inter CQD distances -Creates a composite of CQDs in a matrix of a second metal halide/chalcogenide phase	8.95 % with Methylammonium lead tri-iodide (MAPbI$_3$)	[75]
Small molecules, atomic ligands	-Psuedohalides like SCN$^-$ -Halides like I$^-$	-Reduces inter CQD distances -Small size allows extensive passivation	8.9 % with tetrabutylammonium iodide (TBAI)	[65]

Ligand length is not the only consideration for ligand choice but also the passivating role of ligands and in this case, the chemical structure of the ligand (especially the attachment group) is crucial. *Table 3-1* gives a summary and classification of the types of ligands discussed in the literature. Although organic ligands afford tunability due to the wide variety of structures available, another direction of development that is on the rise is the use of metal complexes as ligands. The methodology for incorporating them in CQD films

was developed by Talapin and co-workers[76–78]. These inorganic ligands are small in nature and they are electrically charged. While traditional bulky organic chain-ligands render colloidal stability to CQDs in solutions via steric hindrance, metal complexes, being electrically charged, confer CQD stability through electrostatic repulsion. This is a distinct advantage over other small inorganic ligands which do not provide the same stability in solution. After ligand exchange, CQDs are very densely packed and FET measurements show that high carrier mobilities can be achieved. Perhaps the most fascinating feature is that when the CQD films with metal complex ligands are annealed, a unique heterostructure of a continuous metal chalcogenide matrix with CQDs embedded is formed[76]. Despite their promising attributes, metal complex-capped PbS CQDs were not used as active materials of solar cell devices until only very recently, where the first such PbS solar cell is reported, and it is fabricated with a lead iodide perovskite complex[75].

The last class of ligand studied comprises of small molecules or even atoms. Before halide ligands became popular, there was very little mentioned on the use of other small molecule ligands in PbS solar cell device fabrication apart from OH$^-$, administered as tetramethyl ammonium hydroxide, which was found to increase the p-type[79] character of PbS but notably increase trap density[80]. Recent work has shown the use of thiocyanate ligand but it does not show any improvement over conventional cross linking ligands like MPA or EDT[62]. The advent of using halides as ligands came towards the end of 2011 in a notable work published by Tang *et al.,* which involves using bromine atoms as surface ligands on PbS[67]. The bromine ligand exchange not only improves mobility but was also shown to provide better passivation than organic ligands. Then, solar cells made from PbS CQD with bromine ligand exchange gave the highest efficiency recorded for CQD solar cells at the time of publication. Attention then spread across the other halogens and most notably the use of iodine. Iodine ligand exchange has led to the formation of "n-type" PbS films,

imparted remarkable air stability and is responsible for some of the highest efficiencies recorded for PbS solar cells at the time of publication[65,80]. Due to increased attention on halogen ligands, there was an increased effort towards understanding the effect of passivating ligands on the properties of PbS CQD films.

3.2.3   Effect of ligands

As a ligand binds to the nanocrystal, surface energy states are altered and the aim is to ensure that mid-gap states are eliminated. Other than passivating the surface, the ligand alters the optoelectronic properties of a quantum dot. Even with similar size/length, different atoms/molecular group may induce different properties - ligands affect the charge transport properties of the CQD film in two important aspects: mobility and lifetime. It was discussed in section 3.2.2 that improved CQD coupling would greatly improve mobility. As for lifetime, it is correlated to trap states/ recombination rate and the extent of passivation offered by the ligand affects this.

Other than charge transport, ligands change the overall composition of the quantum dot[81] and therefore, they would affect the resultant distribution of energy levels and might affect the doping levels of the quantum dot[82,83]. Other than the sulphur and lead composition in PbS, incorporating other elemental species, for example, different halides (Cl, Br, I) as ligands, gave a different extent of doping, as reflected by the PbS CQD film carrier concentration[80,84]. The notion that PbS CQD film is *p*-type has always been widely accepted till reports of the use of halide ligands on PbS CQD were made. Field effect transistor (FET) measurement of halide exchanged-PbS CQD films[84,85] and successful fabrication of PbS "*p-n*" junction devices[79,84,86] both gave evidence of PbS CQD films displaying *n*-type characteristics.

To date, two major hypotheses have been proposed to explain such a phenomenon. The first is a simple argument on stoichiometry balance in a quantum dot – for exact stoichiometry, complete filling of the valence orbitals resembles a closed electronic shell configuration and results in an intrinsic material. For the off-stoichiometry case, an excess of electrons populates the conduction band and results in n-type doping, while a lack of electrons and incomplete filling of the valence band results in p-type doping. As an example, for PbS, when instead iodine substitutes for sulphur, to maintain charge neutrality, this corresponds to an extra electron in the conduction band, that is, n-type doping. This framework was dubbed as "charge-orbital balance" and was formalised by Voznyy *et al.* as a method to predict doping in colloidal quantum dots[87]. The second hypothesis involves surface-induced dipoles of the ligand species on quantum dot and therefore, invoking a change in absolute energy levels of the quantum dot. Brown *et al.* used a range of ligands with different dipole moments and then showed using ultraviolet photoelectron spectroscopy (UPS) a systematic shift of PbS valence, conduction bands and Fermi levels with ligands of increasing dipole moments[88]. This set of experiments is crucial in showing that PbS energy levels are easily modified – either by size, which influences the band gap, or by ligands, which influences the position of band and Fermi levels. Also, the tweaking of Fermi level with respect to valence or conduction band implies a change in doping levels.

While it is still inconclusive as to which hypothesis is more appropriate to describe the action of ligands on PbS CQD doping and energy levels, it is fair to say that there is a huge improvement in the understanding of the surface chemistry of PbS CQD since the advent of CQD film processing. In the next part of this chapter, the improvement and the variety of device architectures would be discussed.

3.3 Advances in device architecture

In the earlier two sections, a review was given on how PbS CQD solar cells have been improved from a fundamental level, which is by augmenting the active material itself – PbS CQD. The surface chemistry and CQD's size/composition has a huge effect on the optoelectronic properties of a CQD film and that, in principle, is a good vantage point to improve the photovoltaic performance of a CQD solar cell. This section takes the reader away from a micro perspective of the quantum dots to the macro – the device structure itself. Improvements made to CQD solar cell performance via a device architectural change are reviewed, along with a focus on material choices and interfaces. Some of the device architectures illustrated in *Figure 3-7* would be discussed in this section.
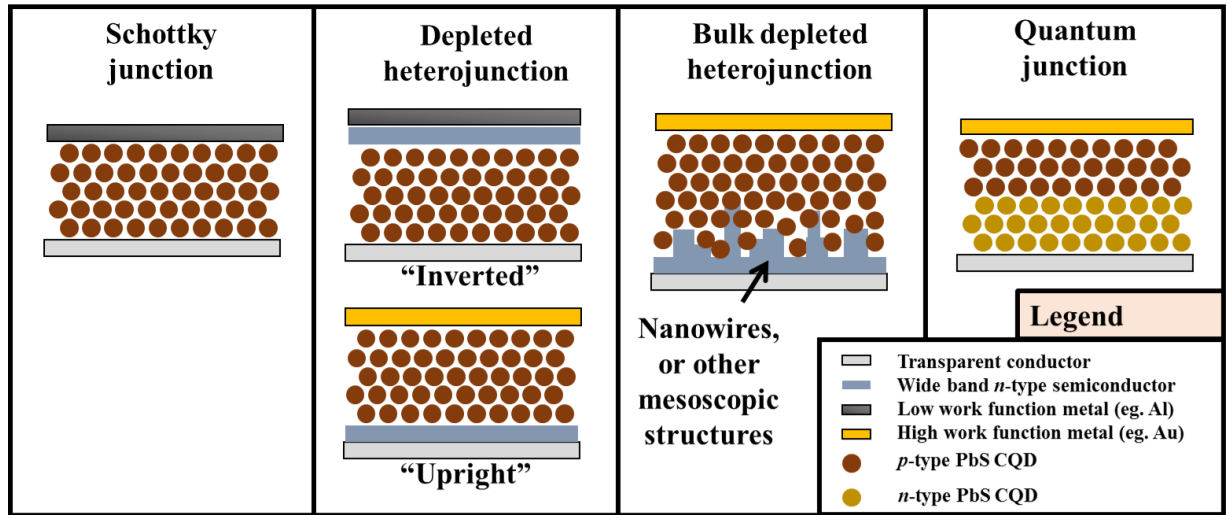
Figure 3-7. A summary of the major PbS CQD architectures described in literatures.

3.3.1 Schottky junction solar cell

The first PbS CQD solar cells using PbS CQD layers as the main photoactive layer was that of a Schottky junction solar cell architecture. Amongst all the various architectures that will be discussed, the Schottky junction solar cell has the simplest structure: It consists of a PbS CQD film sandwich between a metal electrode and a transparent conductor. The choice of a low work function metal (like aluminium or magnesium) forms a rectifying

Schottky junction with the *p*-type PbS CQD film while the transparent conductor (like indium doped tin oxide (ITO)), having a deeper work function, forms an ohmic contact with PbS CQD film (See *Figure 3-8*). Band bending occurs at the interface between the metal and the semiconductor, setting up a Schottky barrier ($\varphi_{barrier}$) and a built-in potential ($\varphi_{built-in}$) with height of magnitude determined by the difference between the *p*-type PbS and metal work function. This built-in potential sets an upper limit to the V_{oc} of the device.
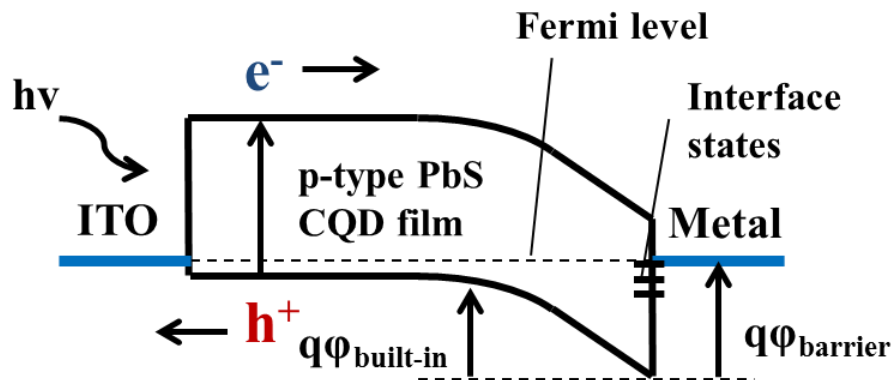
Figure 3-8. Band diagram of a Schottky junction solar cell formed by PbS CQD film and a low work function metal like aluminium.

The efficiency of the Schottky junction solar cell is limited by a few factors. Firstly, the metal-semiconductor interface generates interface states which in many instances, pin the Fermi level of the devices to these interface states. This limits the actual barrier height and hence, the eventual V_{oc} of the device[58,89]. Furthermore, since carrier extraction is most efficient when active layer thickness is the sum of the depletion width and carrier diffusion length[90], the limited depletion width as a result of limited bending at the Schottky junction limits the optimal thickness of PbS film and restricts the J_{sc} of the device. Bend bending is limited because of Fermi-level pinning effect induced by the presence of metal/semiconductor interface states. Secondly, depending on the reactivity and how labile are the ligands of PbS CQD, they might be prone to react with electrode metals[91]. Thirdly,

the PbS CQD Schottky junction devices usually suffers from a low fill factor (*FF*) (40 % or even lower) since the only material that lies between the two electrodes is the PbS CQD film, which makes it is possible that any voids present in the CQD film would create shunt paths for charges and this lowers the shunt resistance and *FF* of the solar cell.

Nevertheless, there are several notable milestones achieved for this architecture of which two, that are in line to the main theme of this thesis, are to be discussed as important learning points for PbS CQD solar cell device technology. The first involves inserting an ultrathin (0.8 nm to 1 nm) interface layer of lithium fluoride (LiF) between the CQD film and the metal electrode[58,91]. This was shown to improve V_{oc} and *FF* of devices, as well as the stability of the device. It was hypothesized that the thin layer of LiF (an insulator) energetically separates the metal from the PbS CQD film, removing interface states and therefore reducing the Fermi level pinning effect. Also, the addition of an interface layer serves as a barrier towards CQD's ligands reacting with the metal electrode, hence prolonging the stability of the device. The second is an inversion of the device structure, making the transparent conductor/PbS junction the Schottky junction. To make that possible, the work function of fluorine-doped tin oxide (FTO) is modified using a thin layer of polyethylenimine (PEI) and a high work function metal was chosen as the top electrode[92]. This work was done by Mai *et al.* and they showed that the inverted device out performs their control regular Schottky device as improvements was gained from better V_{oc} and J_{sc} of the device. Inverting the structure places the Schottky junction closer to the illumination side therefore optimizing charge extraction from higher energy photons (which have lower penetration depth).

3.3.2 Depleted heterojunction solar cell

To overcome the disadvantage of a limited depletion width in a Schottky junction device, the next evolution is to include a second (*n*-type) semiconductor material. Although devices

with cadmium sulphide layer or the polymer PCBM forming the heterojunction with PbS have been realised, the focus in today's research work is on wide band semiconductors that are highly n-type doped, like TiO_2 and ZnO, as they are low cost, offer higher transparency and can be deposited by solution processing techniques. They ensure that the depletion width is very much extended into main absorber of the device, which is the p-type PbS CQD film. Therefore, this particular device structure relies heavily on drift transport as the main carrier extraction mode. Again, the option of having an inverted or an upright structure is available and currently, the upright depleted heterojunction device structure serves as the platform for some of the most efficient PbS CQD solar cells till date.

3.3.3   Bulk heterojunction solar cells

A proposed step ahead of the depleted heterojunction architecture is one that modifies the morphology of the n-type material. Nanowires[93], nanopillars[94] and even grooves tailored to match the length scale of the usual device depletion width[95] – are just some examples on how such a structure can be built upon. Another notable example would be to blend the nanoparticles of the n-type material together with PbS CQD to form a 3-dimensional interpenetrating and percolating network of the two materials[96,97], a strategy familiar to polymer solar cell technology[98]. Ultimately, the bulk heterojunction architecture seeks to improve device performance via:

(i)   An increased surface area of contact between PbS CQD to the n-type semiconductor and therefore effectively allows an increase in PbS CQD loading and total film thickness for increased light absorption.

(ii)   Inducing light scattering and increasing path lengths of photon within the device, therefore increasing the extent of light absorption.

3.3.4 Other strategic device structural improvements

There are two other notable studies on device structure/interface engineering. The first involves putting down a thin layer of molybdenum trioxide (MoO_3) between the PbS CQD film and the top gold electrode[99]. Gold should form an ohmic junction with PbS CQD when considering work functions. However, it was discovered that this tends to deviate with smaller sized PbS CQD and there also exist interface states between gold and PbS CQD film[100]. The addition of MoO_3 was found to alleviate this problem, thereby improves V_{oc} and FF of devices. Additionally, this also allows the use of cheaper low work function metals (like aluminium) in place of gold with almost the same performance. The second deals with modifying the n-type wideband semiconductor. TiO_2 was doped with zirconium to shift its conduction band to better align with the conduction band of PbS CQD of a particular size[101] while in another work, a thin layer of (6,6)-phenyl-61-butyric acid methyl ester (PCBM), that is deposited on TiO_2, helps to reduce interfacial recombination[102]. Similar studies have also been reported with ZnO[103,104].

3.4 Conclusion and prospects

In summary, this chapter reviewed the research progress of PbS CQD photovoltaics, which take into account the understanding of how the material chemistry of PbS CQD and the engineering of device architecture/material interfaces affect the performance of CQD devices. The major findings include:

(i)   Having very monodisperse PbS CQD is important but its further improvement would not lead to further device improvements unless surface defect density has been very much improved first.

(ii) Passivation of PbS CQD surface is thus an important task. Attempts have been made at the synthesis stage, at the fabrication step or using a combination of both, like in the case of hybrid passivation.

(iii) Passivation cannot be done at the expense of sacrificing the electronic properties of PbS CQD. As such, a better understanding and the improvement to ligand exchange, surface chemistry and CQD film processing has been made throughout the years to ensure that PbS CQDs are both well passivated and possess better charge transport properties.

(iv) Device architecture is also an important consideration when seeking to improve overall device performance. Altering device architecture could supplement the low diffusion lengths of PbS CQD films and interface engineering would play a role in reducing interfacial states and interfacial recombination, therefore improving charge extraction.

PbS CQD technology holds great promise for a new generation of solution-processed solar cells with high performance to cost ratio. With the recent news of air stable, high efficiency PbS CQD solar cells without encapsulation and now with reported efficiencies that are almost breaking 10 %, this make PbS CQD an exciting technology. Despite the vast improvements to device physics and materials chemistry of PbS CQD there is still much room for improvements, in particular, in the V_{oc} and FF. Improving defect mediation and charge extraction are therefore urgent tasks for this technology.

Chapter 4 – Experimental Methods

4.1 Introduction

In the previous chapter, a review was given on the various efficiency milestones in the history of CQD solar cells and the various improvements that has provided the impetus for progress. In this chapter, an account of the experimental details of how PbS CQD photovoltaic devices described in the ensuing chapters were fabricated and tested. These include the synthesis of PbS CQDs, surface modification, ligand exchange, materials characterization, film fabrication, metal contact evaporation, and device testing. The aim of this chapter is to provide sufficient information such that any interested reader can have the basis to reproduce the results presented in this thesis.

4.2 Synthesis

4.2.1 Colloidal synthesis of PbS CQDs and purification

The synthesis procedure described in this section was adapted from Hines *et al*.[42] Quantities and injection temperatures were varied to achieve the mean PbS CQD size that is required. In a typical synthesis of PbS CQD with a mean band-gap of 1.3 eV, 0.46 g (2 mmol) of PbO, 2 g of oleic acid (OA) and 10 g of octadecene (ODE) were added into a 25 mL three-neck flask and the mixture was heated and stirred continuously under vacuum at 90 °C for at least 2 hours, yielding a clear lead-oleate solution. The Schlenk line was then switched to Argon flow from vacuum and the temperature of lead-oleate solution was raised to 105 °C. 210 μL of $(TMS)_2S$ (1 mmol) was carefully diluted with 5 g ODE within the fumehood and quickly loaded into a syringe. Care must be taken because $(TMS)_2S$ is extremely reactive and it reacts with moisture in air rapidly to produce H_2S. Then $(TMS)_2S$ was rapidly injected into the flask and the solution turned dark within 3 s, indicating a

nucleation burst. After injection, the heating mantle was switched off immediately (but leaving the stirring on) and after 30 s, the three neck flask was placed in a room-temperature water bath to aid cooling. The modifications required for the synthesis of other mean band gap PbS CQDs described in this thesis are laid out in *Table 4-1* and with the rest of the conditions kept constant.

Table 4-1. Conditions required for the synthesis of PbS CQDs with different mean band gaps

Mean band gap	Amount of oleic acid used	Injection temperature	Cooling procedure
1.2eV	2.5 g	120 °C	Air cooled
1.3eV	2 g	105 °C	Cooled with room-temperature water bath
1.4eV	1.5 g	90 °C	Cooled with iced water bath

Next, the CQDs had to be collected and cleaned to remove unreacted reagents and excess surfactant. This step was carried out in air-ambient. The CQDs product was first separated into two batches and 30 ml of acetone added to each batch to precipitate out the PbS CQDs. The suspension was then centrifuged at 6000 rpm for 10 minutes and the supernatant was discarded. 5 mL of hexane was subsequently added to individual batches to re-dissolve the CQDs and 25 mL of methanol was added to precipitate the CQDs again. The resultant suspension was then centrifuged at 4000 rpm for 4 min. The hexane/methanol washing step was repeated once more and the PbS CQD precipitate was left to dry overnight in the glovebox. The PbS CQDs were finally dissolved in octane, made up to a concentration of 50 mg/mL and stored in a N_2 filled glovebox until further use.

4.2.2 Cation exchange for CdS shell formation

The production of PbS/CdS core/shell CQD utilizes the PbS cores, which were synthesized using the procedure as described in the previous section. Essentially, the formation of a CdS shell is based upon a cation-exchange method, whereby in this case Pb^{2+} cations are being replaced by Cd^{2+}, starting from the outermost surface. The synthetic protocol was adapted from Neo *et al.*[105], with quantities adjusted to be made applicable to the size of PbS CQDs that were used and the thickness of CdS shell to form. Also, further refinement to the reaction temperature and time was made. The first step is to calculate the approximate diameter of PbS CQD by using the empirical formula as described in section 2.1.

Cation-exchange is a substitution reaction and therefore the thickness of the resultant CdS shell could be estimated by the molar quantity of Cd^{2+} precursor used and with this knowledge, the shell thickness could be varied while the total CQD radius remains the same. Having CQD with different shell thickness would provide the opportunity to investigate on the extent of surface passivation and its optoelectronic properties. The quantity of $Cd(Ac)_2$ used is determined by:

$$\frac{mole_{Pb}}{mole_{Cd}} = \frac{\frac{4}{3}\pi r^3 \rho_{PbS} Mr_{CdS}}{\frac{4}{3}\pi(R^3 - r^3)\rho_{CdS} Mr_{PbS}}$$

Equation 4-1

where r is the radius of the core PbS CQD in nm, ρ_{PbS} and ρ_{CdS} are the density of bulk PbS and CdS respectively (g cm^{-3}), Mr_{PbS} and Mr_{CdS} are the molecular weights of PbS and CdS respectively (g mol^{-1}), R is the radius of the CQD (nm), and $mole_{Pb}$ /$mole_{Cd}$ is the experimental atomic ratio of Pb to Cd. As an illustration for 3.2 nm PbS and a final shell thickness of 0.1 nm, using 2 ml of 50 mg/mL of PbS CQD, the number of moles of PbS can be calculated to be 4.2 mmols and from the mole ratio calculated from *Equation 4-2*, the quantity of $Cd(Ac)_2$ needed is evaluated to be 1.0 mmols. The mole ratio of oleic acid to $Cd(Ac)_2$ used is kept at 2.5:1 and the amount of octadecene used is kept at 3.95 times

the volume of oleic acid. It must be noted that the calculation is based on the assumption that the CQD is perfectly spherical.

To prepare 0.1 nm CdS shell-thick PbS/CdS core/shell CQD, 0.395 mL of ODE, 0.115mL of OA and 0.030 g of $Cd(Ac)_2$, were mixed in a 25 mL three-neck flask, connected to a Schlenk line assembly. The mixture was heated and stirred continuously under vacuum at 100°C for at least 1 hour, forming a clear cadmium-oleate solution. The temperature was then reduced to 80°C and the vacuum environment was swapped to an argon atmosphere. 2 mL of the prepared 50 mg/mL PbS CQD solution was swiftly injected into the flask and allowed to react under stirring for 10 minutes. The heating was then turned off and the reaction was quenched by adding 5ml of cold hexane and the resultant solution was then added to 30 mL of acetone to precipitate out the CQDs. The same washing step for PbS CQDs was applied and the prepared CQDs were re-dissolved in octane to a concentration of 50 mg/mL.

Table 4-2 gives a summary of the reaction quantities used and reaction times (with the reaction kept at 80 °C). For the 3.2 nm batch of PbS CQD (averaging 1.3 eV in band gap), for example, if we want 0.1 nm shell, the radius of resultant PbS core is 3 nm. Putting these parameters into *Equation 0-2* yields an atomic/molar ratio of 4.04 Pb:1 Cd.

Table 4-2 Reagent quantities and parameters for different CdS shell thickness based on original 3.2 nm PbS CQD.

	CdS shell thickness (nm)		
	0.1	0.2	0.3
ODE (ml)	0.295	0.681	11.950
OA (ml)	0.075	0.172	3.025
Cd(Ac)2 (g)	0.0253	0.0582	0.1022
Reaction time after injection (min)	7	10	15

4.2.3 Synthesis of ZnO CQD solution

ZnO nanocrystals were synthesized by using the method adapted from Pacholski *et al*[106], with the final solvent composition tuned in accordance to Li *et al* for better colloidal stability[107]. 2.95 g of zinc acetate dihydrate was dissolved in 125 ml of methanol and kept, under stirring, at 60°C. 1.48 g of potassium hydroxide was dissolved in 65 ml of methanol. Then, potassium hydroxide solution was added dropwise to the zinc acetate solution and the reaction mixture was kept, under stirring, at 60°C for 2.5 h. ZnO nanocrystals were extracted by centrifugation at 6000 rpm and then washed twice by methanol followed by centrifugation. Finally, a mixture of 5 ml of chloroform and 5 ml of methanol was added to dissolve the precipitates and the solution was finally filtered with a 0.45 µm polyvinylidene fluoride (PVDF) filter.

4.2.4 Preparation of TiO$_2$ sol-gel

This procedure is reported in the work of Docampo *et al*[108]. The TiO$_2$ sol-gel is prepared by first mixing of 2.53 mL of isopropanol and 35 µL of 2 M HCl and then the resulting

solution is slowly added dropwise to a 0.43 M titanium isopropoxide solution in isopropanol (typically 369 μL titanium isopropoxide in 2.53 mL of isopropanol) under vigorous stirring. This yields a clear liquid and the sol-gel is ready for use.

4.2.5 Iodide solution-phase ligand exchange

This procedure was developed by Ning *et al*[70]. PbS CQDs were diluted to a concentration of 10 mg/mL and 4 mL of this solution was added to 3 mL of methylammonium iodide in dimethylformamide (DMF) solution with a concentration of 80 mg/mL. The immiscible phases were vortexed vigorously and PbS CQDs were transferred into the DMF phase. The DMF phase was carefully separated and toluene is added to precipitate the CQDs. The precipitates were finally dispersed in butylamine at 200 mg/mL concentration for film fabrication. It must be noted that the final solution in butylamine has to be prepared fresh prior to film fabrication.

4.3   Characterisation of CQDs

4.3.1   Transmission electron microscopy (TEM)

A morphological study of CQDs was performed using a JEOL 2010 TEM, with EDX capability, operating at 200 kV and the Oxford JEOL 2200MCO Aberration Corrected, Monochromated FEG-TEM operating at 80 kV. The JEOL 2200MCO was operated with the help of Dr Judy S. Kim. TEM samples were prepared by making dilute solutions of CQD, then briefly dipping the TEM grids into the solution and the letting them dry in ambient conditions. Additional 1-3 s of argon plasma treatment aids the removal of free organic ligands so as to achieve higher quality images. With its high resolution, TEM enables the measurement of the particle sizes, size distribution and crystallinity. The reported mean particle sizes were obtained by fitting with a Gaussian distribution curve to the experimental size histogram.

4.3.2 UV-Vis-NIR absorbance spectrometry

All optical absorption spectroscopy of the CQDs was measured on a Cary Varian 4000 UV-VIS-NIR spectrophotometer. For solution measurements, diluted CQD solution (5 mg/ml in octane) was loaded in a quartz cuvette. For solid films, CQD solutions were spin coated onto a clean glass substrate. Before each measurement, a baseline procedure is performed, which sets the 100% transmission (no sample) and 0% transmission (block the light completely). Measurements are always taken against a reference sample which is the pure solvent in the case of solution measurement and a piece of clean glass for the case of solid film measurement.

4.3.3 X-ray diffraction (XRD)

XRD is a crystallographic characterization tool that determines the periodic arrangement of atoms within a crystal. Diffracted X-rays are collected by the detector which sweeps through a range of angle and then measuring the intensity or counts of the collected X-rays. The diffractogram of intensity versus angle gives various information about the sample such as the identity of the phases present, composition and even the approximate size of the crystals. Our XRD data are obtained by Philips theta/2theta diffractometer and samples were prepared by drop casting CQD solutions onto glass.

4.3.4 Energy dispersive X-Ray (EDX) spectroscopy

EDX provides information on the identity and the composition of elements in a sample. High energy electrons bombard the sample, causing core electrons from the sample's atoms to be excited to a higher energy level and upon relaxation, they release X-ray radiation that has a specific energy, characteristic to that of the element's electronic structure. EDX was performed in conjunction with JEOL 2010 TEM characterisation, at 200kV, and INCA

analysis software was used for identification and quantification. The electron beam spot is adjusted such that several CQDs are exposed at a time so that the collected EDX spectrum gives a statistical average.

4.3.5   Raman spectroscopy

Raman spectroscopy detects the presence of specific bonds that vibrate or rotate at a particular frequency. This relies on the inelastic scattering of incident light. Some photons from the incident light interacts with phonons (quantized molecular vibrations), resulting in the scattered photons having more or less energy. This shift in energy gives us the identity of a certain bond. Scattered photons are detected and collected to form the Raman spectrum. Raman spectroscopy analysis was carried out using a JY Horiba LabRAM ARAMIS imaging confocal Raman microscope. A 532 nm laser is used and its intensity is controlled to minimise sample damage. Each scan is averaged upon 8 co-scans. Raman spectra for CQD samples were prepared by drop-casting CQD solutions onto silicon substrates, allowing them to dry and thereby forming a solid film.

4.3.6   Fourier transform infrared spectroscopy (FTIR)

Infrared spectroscopy identifies a particular bond based on the vibration characteristics of chemical functional groups (mostly organic functional groups) in a sample, by measuring the molecular absorption in the infrared. Information obtained from FTIR complements Raman spectroscopy. The FTIR spectra presented in this work were obtained by using a Varian Excalibur FTS 3500 spectrometer. Samples were prepared by drop casting solutions on glass. The final spectrum of a sample is an average of 64 scans and the background is taken into account and deducted by the software.

4.3.7 X-ray photoelectron spectroscopy (XPS)

XPS is a surface-sensitive chemical analysis tool. It not only identifies the presence of a particular element but also its bonding state (and oxidation state) and it is also quantitative in nature. The XPS spectrum is obtained by irradiating a sample with X-rays and then detecting and measuring the number and the kinetic energy of photoelectron ejected from the sample due to X-ray excitation. These electrons are core electrons that have energies that are element specific, which enables elemental identification. The limitation of this technique is that it is surface specific – ejected photoelectrons only escape from the top 0 to 10 nm of the sample being analysed. Also, the detection limit is in the parts per thousand to parts per million range and hydrogen and helium cannot be detected. CQD samples were mounted with conductive carbon tape on the sample holder. The machine used is a near ambient pressure XPS (NAP-XPS) kit used in UHV mode and the pressure during the measurements was below 10^{-9} mbar. Each sample was scanned 5 times at 0.1 eV resolution over the binding energy range of 0-900 eV. Also, the sample was charge compensated with an electron flood gun. An Aluminium K-alpha X-ray source with an excitation energy of 1486.6 eV is used. The detector/analyser is a PHOIBOS 150 NAP (a differentially pumped and a 150mm mean radius hemispherical analyser). Casa XPS version 2.3.16 and Igor Pro 6.36 were used to analyse XPS results. All XPS measurements were carried out by Dr Christopher Muryn, Ms Philippa C. J. Clark and Ms Hanna Radtke in the Photon Science Institute, University of Manchester.

4.3.8 Photoluminescence (PL) spectroscopy

PL is a non-destructive, contactless tool for studying the electronic structure of a sample. It allows the determination of band to band optical transitions and the presence of any defect levels. Furthermore, quantification of PL yields measures the extent of radiative recombination over non-radiative loss channels. When PL is taken in a time-resolved mode,

the PL lifetime gives an indication on how fast recombination process are occurring to charges in the excited state. The lifetime is the inverse of the sum of both the radiative and non-radiative recombination rate. Steady-state PL measurements were taken using an automated spectrofluorometer (Fluorolog, Horiba Jobin-Yvon), with a 450 W Xenon lamp excitation source and an InGaAs NIR detector. The excitation wavelength was 500 nm. All spectra were corrected for instrumental response using a calibration lamp of known emissivity. Time-resolved PL measurements were acquired using a time-correlated single photon counting (TCSPC) apparatus (FluoTime 300, PicoQuant GmbH). Film samples were photo-excited using a 507 nm laser head (LDH-P-C-510, PicoQuant GmbH) pulsed at 300 kHz (for PbS-OA and PbS/CdS-OA samples), with a pulse duration of 117 ps and fluence of ~0.5 μ/cm^2. The PL at the peak emission (~1100 nm) was collected using a high resolution monochromator and NIR-PMT detector assembly (H10330A-45, Hamamatsu). Monoexponential fits to the data were carried out using commercial fitting software (FluoFit v4.5.3, PicoQuant GmbH). CQD films 50 ± 4 nm thick were prepared by spin coating CQD solutions on microscope glass slides. All PL measurements were conducted in the physics department with the help of either Dr Samuel D. Strank or Mr Giles E. Eperon. Additional results were obtained from photoluminescence quantum yield (PLQY) experiments, which feature an integrating sphere to capture all emitted photons for a given excitation beam fluence. This gives a very clear indication and a fair comparison on the non-radiative defect densities between samples. CQD solution (in octane) was loaded into cuvettes for PLQY measurements A continuous-wave 532 nm green diode laser with a beam spot of 0.3 mm^2 was used to photo-excite the samples. Emission was measured using an Andor iDus DU490A InGaAs detector. For each PLQE value, PL spectra from this setup were taken with no sample inside the sphere, then with the sample in the sphere but the laser excitation not directly incident on it, and then when the sample was directly excited.

These three measurements enable the absorption of the sample to be accounted for, thus giving a percentage of photons emitted for a given number of photons absorbed. PLQY measurements were done by Mr Tom Jellicoe from the Optoelectronic Group of Cavendish Laboratory in the University of Cambridge as part of an external collaborative work.

4.3.9 Scanning Kelvin probe (SKP)

Kelvin probe is a technique which relies on measuring a potential gradient between a sample and the probe that is used to contact the material. To measure the potential gradient (or difference) between the sample and probe, an applied voltage ΔV_{sp} is varied till flat band potential is achieved, which is identified by no current flow, then eΔV_{sp} is the work function difference between the probe and the sample, where e is the elementary charge. To get the absolute value, the probe has to be calibrated first with a material of known work function. Work function data were taken by the KP Technology Scanning Kelvin Probe System 2001. For each sample, 25 data were measured for each of 3 arbitrarily chosen scanning points (75 data in total). At the beginning and the end of analysis, measurements of reference samples (Al: work function of 4.1 eV, and Au: work function of 5.1 eV) were used to generate a calibration curve. This calibration curve converts raw data, which are relative work function values with respect to the work function of the scanning probe, to absolute work function data. All SKP measurements were made by Mr Yujiro Tazawa, a fellow PhD candidate in the same group.

4.3.10 Secondary ion mass spectrometry (SIMS)

SIMS is a technique suited for the analysis of the elemental composition of solid surfaces by sputtering the surface of the sample with a focused beam of ions and then collecting and analysing the ejected secondary ions. The mass/charge ratios of the detected secondary ions are measured with a mass spectrometer to determine the elemental, isotopic, or molecular composition of the surface, up to a depth of 1 to 2 nm. SIMS is very sensitive

as it has a low elemental detection limits ranging from parts per million to parts per billion. However, due to a huge variation in ionization probabilities among different species, SIMS is generally considered to be a qualitative rather than a quantitative technique. Another drawback is that it is a destructive technique. If the sputtering of the surface and detection of secondary ions goes on continuously, a compositional depth profile of the sample could be built. NanoSIMS50 (CAMECA, France) was used to obtain compositional depth profiles of devices made without the top gold contact. The Cs^+ source in the NanoSIMS was used, and $^{12}C^-$ $^{16}O^-$, $^{32}S^-$, $^{64}Zn^{16}O^-$ and $^{127}I^-$ signals were detected to measure the O/S count ratio and to identify layers in the solar cell. A probe current of ~6.9 pA was used for depth profiling. The NanoSIMS was set up to sputter an area of 20 µm by 20 µm, and signals from the central 10 µm by 10 µm area were counted to avoid artefacts from crater edges. All SIMS measurements were carried out by Dr. Haibo Jiang.

4.4 Device fabrication

There are five different structures presented in this thesis. Therefore, only the generic device fabrication steps are outlined here with the details discussed in their associated chapters.

4.4.1 Substrate and transparent electrode preparation

4.4.1.1 Indium tin oxide (ITO) etching

Commercial ITO coated glass substrates (Delta Technologies, 7 Ω/□) were diced into 12 mm by 14 mm by 1.1 mm pieces. They were then patterned by masking the central portion of ITO with a polyvinylchloride adhesive tape for protection and then exposing the rest of the ITO surface to an etchant. The etchant was made up of deionised water, concentrated hydrochloric acid, and concentrated nitric acid in the volume ratio of 50:45:5. The etchant was held at 65 °C and the masked ITO substrates were immersed in it for 5 minutes. The

substrates were then immersed into cool deionised water, stripped of their adhesive masks and then washed with deionised water again. The resultant ITO electrode pattern is illustrated in *Figure 4-1*.

4.4.1.2 Fluorine doped tin oxide (FTO) etching

Commercial FTO coated glass substrates (Pilkington NSG-TEC A7) with 2.2mm thickness and sheet resistance of 7 $\Omega/\square$, were first diced into 12 mm by 14mm sized pieces. The same masking procedure as ITO was applied. The etching process involves covering the entire surface of the masked substrate with zinc metal powder and then adding 200 μL of 2M hydrochloric acid. The FTO is reduced by the nascent hydrogen produced by the acid-metal reaction and could be removed by rubbing the surface gently with a cotton swab. An electrode pattern identical to that on the ITO was produced.
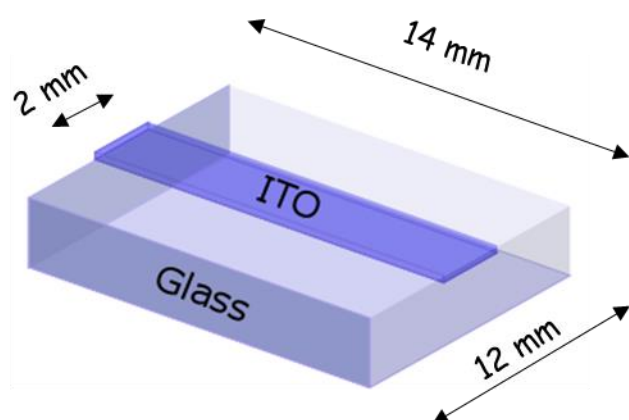
Figure 4-1. ITO-glass electrode pattern. FTO substrates have the same pattern.

4.4.1.3 Cleaning

To clean the surface of the transparent electrode, the substrates were immersed in a beaker of laboratory detergent solution (Decon), and then sonicated for 5 minutes. The substrates were then transferred and sonicated in a beaker of de-ionised water for a further 5 minutes

to remove any traces of detergent. Next, the substrates were sonicated in acetone and then in isopropanol at 50°C for a further 5 minutes each. The acetone washes away any organic matter on the substrate while the isopropanol aids in removing the traces of acetone left over from the previous cleaning step.

Finally, the substrates were dried naturally in a clean environment and then subjected to an oxygen plasma treatment for 1 minute, by using Nanotech PLASMOD plasma chamber, so as to remove any remaining organic material that had bonded to the substrate surface. The O_2 plasma treatment also make the substrate surface smooth and hydrophilic, which is critical in improving the uniformity of the first subsequent layer of solution processed thin film formed by spin coating.

4.4.2 Spin coating process

Spin coating is a fast and simple technique to form a uniform thin film on a smooth substrate. The final thickness of the film depends on the spin rate and the concentration of the solution. The ability to form a uniform thin film depends very much on the wettability of the solution on the substrate surface. In this thesis, the first layer of thin film formed on the transparent electrode substrate is either poly(3,4-ethylenedioxythiophene) polystyrene sulfonate (PEDOT:PSS), zinc oxide (ZnO) and titanium dioxide (TiO$_2$) – all of which are dissolved in polar solvents, which would be compatible with the prepared substrates after O_2 plasma treatment.

Spin coating of CQD solution mainly involves a layer by layer build up process, with the exception of the iodide ligand exchange PbS that is discussed in chapter 7. Each layer comprises a film formation step, a ligand exchange step that renders the CQDs insoluble in their original solvent, and then a washing step to remove the unbound original ligands. The

ability to form layers of CQD thin films comes from chemical bonding between the CQD to the first layer of material formed on the substrate.

4.4.3   Top contact deposition

All top metal contacts are formed by thermal evaporation, which is a physical vapour deposition technique. It involves in heating up a metal source at very low pressure. The advantage of using such a system is that deposition rate can be controlled to a very fine level and slow, controlled evaporation minimizes impact on the sample surfaces, as opposed to techniques like sputter coating. Thermal evaporation is carried out with an Edwards 306 evaporator with a pressure of at least 1.0×10^{-5} Torr. The deposition rate was kept fixed at 0.1 nm/s, measured by a quartz crystal thickness monitor, and the thickness were kept at 120 nm for Al and 100 nm Au evaporation. A shadow mask was applied to define the metal electrode pattern and therefore, the final solar cell sample area. A generic device structure is shown in *Figure 4-2*. The test sample has a device area of 0.02 cm^2. The actual test area is reduced by the application of a 0.01 cm^2 shadow mask during performance characterisation.
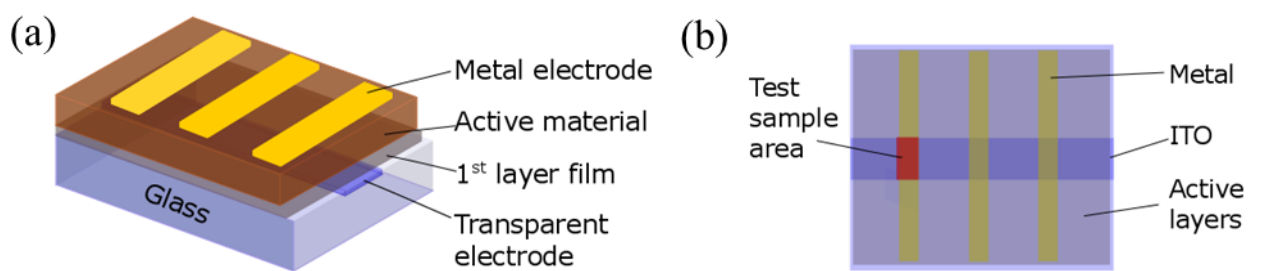
Figure 4-2. (a) A schematic showing a generic device structure and (b) the top view of the device. The area shaded in red (0.02 cm^2) is that of an actual test sample – there are 3 samples per device substrate.

4.5 Device characterisation

4.5.1 Current-voltage characteristic

The power conversion efficiency, fill factor, V_{oc}, J_{sc} and the parasitic resistances of the device are determined with this measurement. In the absence of light, dark current measurements could be carried out, which gives information about the reverse saturation current and general diode characteristics. A current-voltage sweep is performed using a Keithley 2400 source-meter with voltage swept from -0.5 to 1.0 V at a step size of 0.025 V, with a time delay of 100 ms between each step. The sample is contacted and housed in a home-made sealed testing rig with continuous N_2 purge. The actual test pixel is reduced by the application of a 0.01 cm^2 shadow mask. Illumination was provided by Newport 96000 150 W solar simulator fitted with an AM1.5 filter and the intensity is adjusted to 100 mW cm^{-2} as calibrated using ABET Technologies Model 15151 reference cell. Spectral mismatch factor was not calculated.

4.5.2 External quantum efficiency (EQE)

EQE is another way to quantify the efficiency of a device. In this case, it measures the amount of the incident photons supplied, at each wavelength, onto the sample and simultaneously measures the amount of extracted electrons (reported as current). Therefore, it reports the device's electrical response at a quantum level over the various wavelengths, which provides useful information about device light absorption and the ability to extract photogenerated carriers. Our EQE spectrum is recorded while illuminating the devices by a halogen lamp fitted with an Oriel Cornerstone 130 monochromator. No white light bias is applied and illumination spot size is focused such that it is smaller than the actual device area. Light intensity at different wavelengths was calibrated using a Newport 818 UV enhanced silicon photodetector and a Newport 918 IR germanium photodetector. For this

work, no external bias was applied during measurement and the current signal was measured with a Keithley 6845 picoammeter.

4.5.3 Capacitance-voltage (*C-V*) measurement

C-V is a measurement carried out on metal-semiconductor junction (Schottky junction) or a *p-n* junction. In these junctions, a depletion region is present and behaves like a capacitor. The depletion width is dependent on the application of external bias and this enables the modulation of the capacitance. Plotting capacitance against voltage and following Mott-Schottky analysis gives information on the semiconductor such as its doping densities and electrically active defect densities. Our *C-V* measurements are performed using an Agilent E4980A option 001 precision LCR meter, with a 25 mV probe signal modulated at 1000 Hz. The sweeps are performed between -1.0 and 1.0 V. All measurements are performed with sample housed in a dark, electrically shielded test rig but with no air or moisture control.

4.5.4 Open circuit (*V$_{oc}$*) decay measurement

V$_{oc}$ decay measures the minority carrier lifetime in a photovoltaic device. Lifetime is dependent on recombination kinetics and lifetime can be obtained by monitoring the exponential decay of *V$_{oc}$* from the illuminated quasi-equilibrium state (maximum photogenerated carriers) to the dark equilibrium (no photogenerated carriers). Our *V$_{oc}$* decay measurements are carried out by illuminating devices with a Thorlabs MWWHL3 white LED fitted with a DC2100 LED driver with PWM mode. All measurements are performed with the sample mounted on a test rig with connection to the oscilloscope. Keeping the device to LED distance fixed, the white light intensity was adjusted to reach device *V$_{oc}$* as recorded in the *J-V* measurement, and light pulses were adjusted to 100 Hz with a 30% duty cycle. The light pulse duration is chosen such that the devices reached their *V$_{oc}$* value during the first 10% of the light pulse to ensure the steady state has

been reached before the pulse is switched off. The photovoltage decay was captured on a Teledyne LeCroy WAVEJET 354 oscilloscope across the high impedance (1 MΩ) port.

4.5.5 Light dependent short-circuit current (J_{sc}) measurement

Light dependent J_{sc} measurement is a technique that investigates the balance of charge extraction at opposite electrodes. Photocurrent should vary linearly with light intensity but a deviation from that signifies that rate of electron and hole extraction is unbalanced, resulting in the formation of space charge (space charge limited current). The same setup for *J-V* measurement is used here. Illumination was provided by a Newport 96000 150 W solar simulator fitted with an AM1.5 filter and the intensity is adjusted to 100 mW cm^{-2} as calibrated using ABET Technologies Model 15151 reference cell. Neutral density filters were used to achieve fractions of 1 sun light intensity.

Chapter 5 – PbS/CdS CQD solar cell

Part of this thesis chapter was published in *Chem. Mater.*, **2014**, *26* (13), pp 4004–4013 and presents the synthetic chemistry and the material characterisation of PbS/CdS core/shell nanocrystals. The synthetic method was developed by Darren C. J. Neo, who also prepared the manuscript with the help of Dr Cheng Cheng, Dr Samuel D. Stranks, Dr Simon M. Fairclough, Dr Judy S. Kim, Prof. Angus I. Kirkland, Prof. Jason M. Smith, Prof. Henry J. Snaith, Prof. Hazel E. Assender and Prof. Andrew A. R. Watt. Dr Samuel D. Stranks provided assistance with photoluminescence measurement and fittings. Mr Tom Jellicoe from the Cavendish Laboratory of the University of Cambridge conducted the photoluminescence quantum yield (PLQY) measurements. Dr Simon M. Fairclough performed the X-ray diffraction simulations and Dr Judy S. Kim helped with high resolution imaging of PbS/CdS CQD using JOEL 2200 transmission electron microscope.

5.1 Introduction

The effects of CQD surface defects were discussed in chapter 2 and the various techniques that have been developed to mitigate this were reviewed in chapter 3. This chapter is dedicated to explaining how CdS shell passivation is utilized on PbS CQD and then optimized for photovoltaic performance.

The limiting factor for the current generation of CQD devices is the lower than expected open-circuit voltage (V_{oc})[58] values, which are attributed to the high density of defect states[109] on the CQDs. Electronically active CQD thin films are produced by exchanging the long-chain ligands used to synthesize and stabilize the CQD for a shorter linker ligand which allows electronic coupling between neighbouring CQDs in the film. Currently a post-deposition solid state treatment is used to produce the best devices[79,84,110]. However, despite the improvements made, this exchange process has been shown to be imperfect,

causing surface defects which increase recombination and non-radiative losses, thus directly reducing V_{oc}[110]. These defects are caused by incomplete ligand coverage[111] or the inherent instability of the more labile shorter ligands[112]. It must be noted here recombination events includes bi-molecular and even tri-molecular (Auger) recombination but nonetheless, the focus here is on defect-mediated recombination. In addition, post-deposition exchange is highly dependent on optimizing ligand concentration, solvation, impurity elimination, and processing environment[113–115]. Ip *et al.* recently investigated the role of ligand coverage and demonstrated that a combination of short bi-functional organic and atomic halide ligands results in nearly complete CQD surface passivation. Using transient photovoltage measurements, the authors showed a reduction in defect density as compared to an organic ligand-only treatment[110]. However this strategy is still dependent on the stability of ligands. This provides the motivation to search for a more robust passivation technique.

Shell passivation involves using another material that has a higher band gap to coat the surface of the original CQD, thereby forming a core/shell CQD. Shell passivation is used in photoluminescent applications of CQD such as bio-labelling[116]. This shell passivation method has been shown to be effective in eliminating defect states[105,117–119], giving rise to higher photoluminescence quantum yields, longer decay lifetimes and even greater chemical and environmental stability[117,120,121]. This provides the impetus to employ a similar strategy for PbS CQD in solar cell applications. While employing an overcoat of a wider band-gap material on a nanocrystal sensitizer is a well-established procedure in quantum dot-sensitized solar cells[122], reports of using core/shell quantum dots as both the light absorber and the active transport material are scarce. This is possibly because a thick shell layer of a type I heterostructure impedes exciton dissociation, charge extraction and transport[123]. Via heat treatment and thermally decomposable ligands, Zamkov and co-

workers build a thin film of PbS CQD in CdS matrix using PbS/CdS core/shells with relatively thicker shells. They showed that passivation improved and the distance between PbS quantum dots, and hence the thickness of CdS layer, influences carrier mobility and device performance[124,125]. At the time of writing, to the best of my knowledge, there is no report on a synthesis procedure that allows a fine control over CdS shell thickness producing PbS/CdS CQDs ready for solution processing. Also, a PbS/CdS CQD solar cell based on layer by layer spin coating technique without the need for heat treatment is virtually unheard of.

In this chapter, a core/shell passivation strategy will be studied. This entails looking into the balance between shell passivation and charge extraction, thereby making PbS/CdS CQD film a viable active layer in a solar cell device with improved performance over reference PbS devices. The developed strategy comes in two parts: (i) Shell passivation, thereby forming PbS/CdS CQD and the optimisation of shell thickness. (ii) Lower the energetic barrier imposed by the shell by using a combination of organic and halide ligand to improve device performance. The chapter will start off with results on characterizing the presence and the thickness of the CdS shell, then initial experiments done to incorporate PbS/CdS core/shell CQD into solar cell devices and the direct observation of the passivation effect on device performance will be examined. The effect of shell thickness on device performance will be discussed and finally, core/shell devices are optimised by using a combination of organic and halide ligands to modify the surface of PbS/CdS CQD so as to improve charge transfer process.

5.2 Synthesis and characterisation of PbS/CdS core shell CQD

5.2.1 Rationale for the choice of CdS as shell material

The choice of CdS as the shell material is that:

(i)   It has a higher band gap than PbS, which aids in preserving quantum confinement.

(ii)   CdS has a similar lattice constant to PbS and is able to form a face-centered cubic (FCC) structure and thus, using CdS as a shell layer via cation exchange reduces strain-related defects that negate the benefits of a passivating shell layer.

5.2.2   Rationale for cation exchange procedure

The rationale of using a cation-exchange approach to produce core/shell nanocrystals is as follows:

(i)   As opposed to conventional repeated hot injection methods, it requires a relatively low temperature and thus minimizes the effect of Ostwald ripening, which would otherwise increase the size distribution[126].

(ii)   A key feature of the cation-exchange method is that the anionic framework of the CQD is preserved and the incoming cation is incorporated into a similar crystal structure[127]. This again minimizes severe lattice distortions which would then introduce more defect states.

(iii)   Another feature of this technique is that the overall diameter of the synthesised PbS/CdS core/shell colloidal quantum dot remains the same as the initial diameter of the original PbS CQD, while the PbS core decreases in size and CdS shell thickens during the shell formation. Therefore, monitoring the size of the PbS core gives a way to track the extent of cation-exchange that take place.

5.2.3 Characterisation of PbS/CdS CQD

Using TEM, the mean particle sizes were measured and were fitted with a Gaussian distribution curve (See *Figure 5-1*). The preservation of the overall CQD diameter before and after cation-exchange supports the cation-exchange mechanism. However, due to the similarity in crystal structure and lattice constant of CdS and PbS, it is difficult to image the thin layer of CdS even when using high resolution TEM[128]. Hence, indirect methods to measure the core size and shell thickness are required.
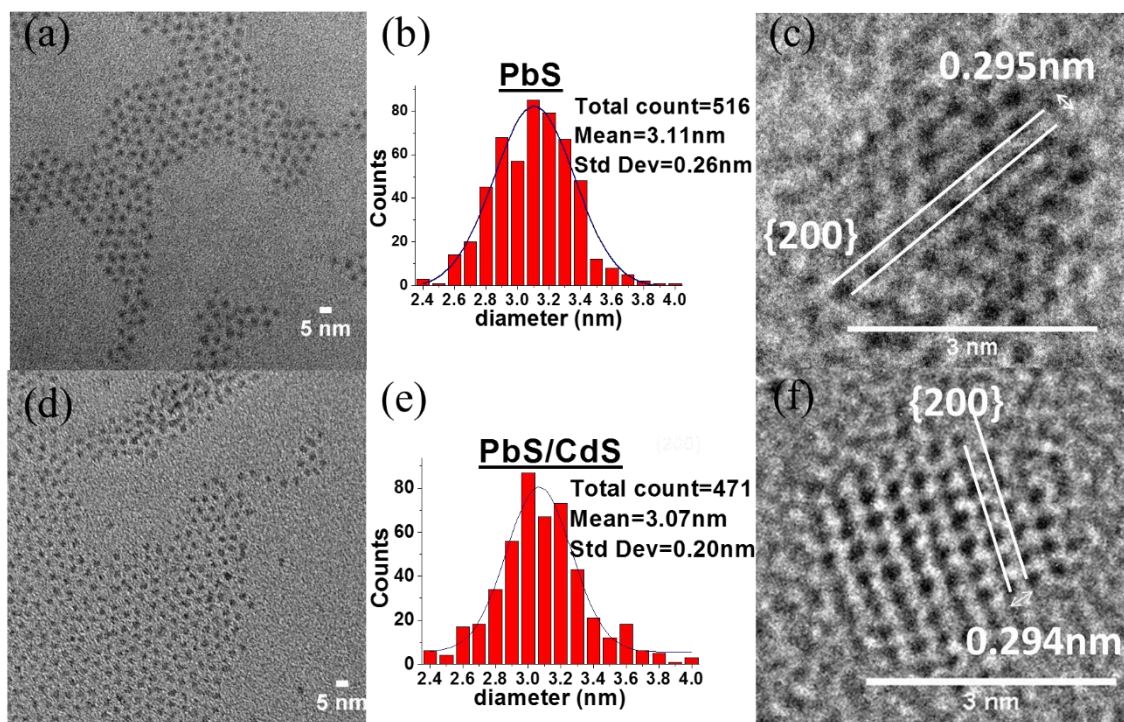
Figure 5-1. TEM images of PbS and PbS/CdS core/shell CQDs. (a, d) Low magnification images of 1.26eV PbS CQD and 1.34eV PbS/CdS CQD, respectively. PbS/CdS CQDs have a calculated 0.1nm CdS shell and are synthesized from the same batch as the PbS CQDs. (b, e) Histograms of the size distribution, with a Gaussian fit, of 1.26eV PbS CQDs and 1.34eV PbS/CdS CQDs, respectively. (c, f) High magnification images of 1.26eV PbS CQD and 1.34eV PbS/CdS CQD respectively. High resolution and high magnification images obtained with JOEL 2200 with the help of Dr Judy S. Kim.

Since PbS core size decreases while the CdS shell thickens and the overall diameter remains the same, by tracking the PbS core size using UV-Vis-NIR absorbance spectrometry (*Figure 5-2*), the shell thickness could be calculated. According to the empirical formula developed by Moreels *et al.*[23], that was introduced in section 2.1, the original and the final PbS core diameter can be calculated. Hence, the CdS shell thickness can by calculated by:

$$Shell\ thickness = \frac{Initial\ PbS\ diamater - Final\ PbS\ core\ diameter}{2}$$ *Equation 5-1*
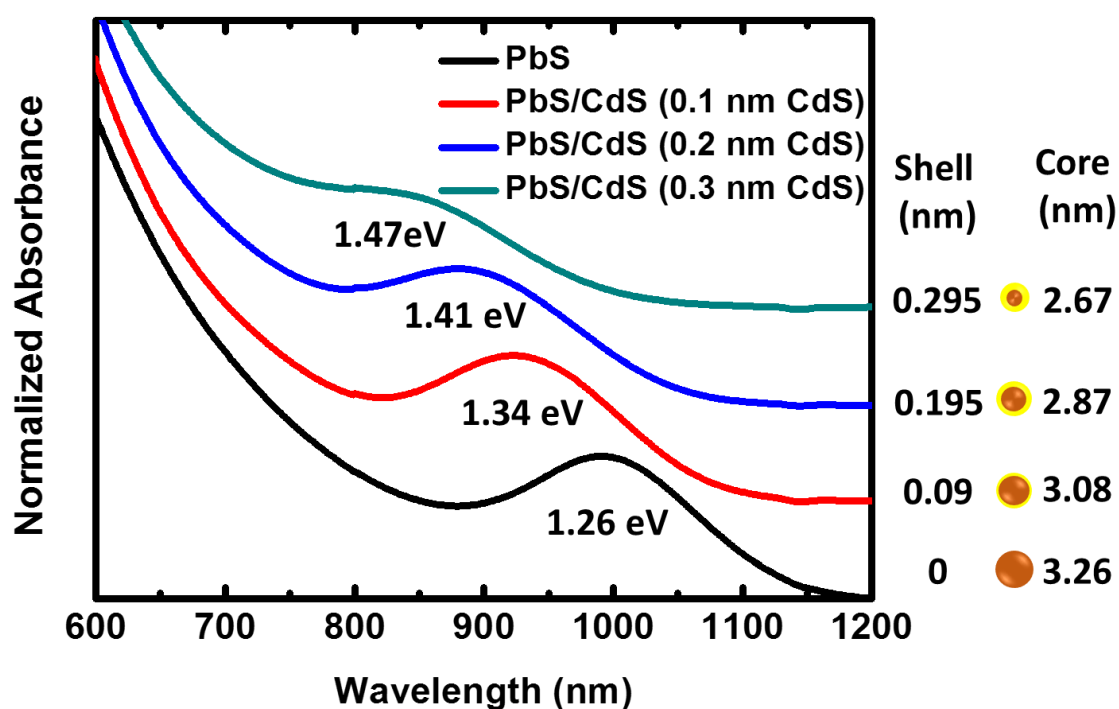
Figure 5-2. Normalized absorbance curve of PbS CQDs and PbS/CdS CQDs with increasing shell thickness, synthesized from the same PbS batch. Absorption was carried out with CQDs dissolved in hexane with oleic acid as ligands. The schematic inset serves as a visual aid, displaying the calculated shell thickness and core diameter displayed.

From the crystal structure of CdS (zinc blende), a good gauge of the thickness of a monolayer of CdS would be the nearest cadmium to sulphur atom distance, which is about 0.25 nm[129]. The thinnest CdS shell thickness for the core/shell CQD in this work was calculated to be 0.1 nm, using the band-gap approach. Similar sub-monolayer CdS has been deduced in other work using this approach[130]. This apparent discrepancy might be due to the fact that the thickness of shell layer is determined by subtracting the total CQD diameter from the diameter of the PbS core, which is only an estimation using the excitonic peak feature on the absorption curve, and *Equation 2-1* and *4-1* assume a spherical-shaped CQD. Furthermore, the PbS core has a common shared outer layer of sulphur atoms with the CdS layer. Thus, a simple subtraction of diameters may result in an apparent sub-monolayer value of CdS. Lastly, it is worth noting that *Equation 2-1* was formulated using PbS CQD with oleic acid as ligands. Therefore, when using *Equation 2-1* to determined PbS core size, CdS shell having less confinement potential compared to purely a shell of oleic acid ligand, suggests that the extent of blueshift was overestimated and therefore leading to an underestimation of the actual CdS shell thickness. Using UV-Vis-NIR absorption spectroscopy coupled with TEM measurements, core sizes and shell thickness could be determined but not the chemical composition of the CQDs. Hence, XRD was employed to confirm the presence of a CdS phase.

The obtained XRD diffractograms (see *Figure 5-3(a).*) indicate the presence of an increasing CdS phase composition for PbS/CdS CQDs with increasing CdS shell thickness. This implies that the CdS only exists as part of the core/shell heterostructure and, eliminating the possibility of the nucleation of separate CdS phases (also confirmed with TEM) and homogenous alloying. As illustrated in *Figure 5-3(a)*, the relative peak heights of the PbS/CdS core/shell CQD sample and positions are influenced by the CdS shell on the PbS core. Taking the most obvious peaks as an example, pure bulk CdS zinc

blende has a higher peak intensity for the {111} reflections compared to the {200} reflections whereas both PbS CQD and pure PbS bulk phase (rocksalt structure) have almost equal intensities for these reflections. For a core/shell structure with a constant diameter, a thicker shell layer would increase its overall composition with respect to the amount of PbS left in this heterostructure. This argument is consistent with the XRD results in *Figure 5-3(a)*, showing an increasing {111} intensity while the {200} peak decreases as the CdS shell thickness increases. A pure phase CdS shell rather than an alloyed Cd-PbS is also supported by a theoretical work by Zhao *et al.* that proposed an observation of a much smaller band gap (due to less quantum confinement) if shell layer exists as an alloy[117].
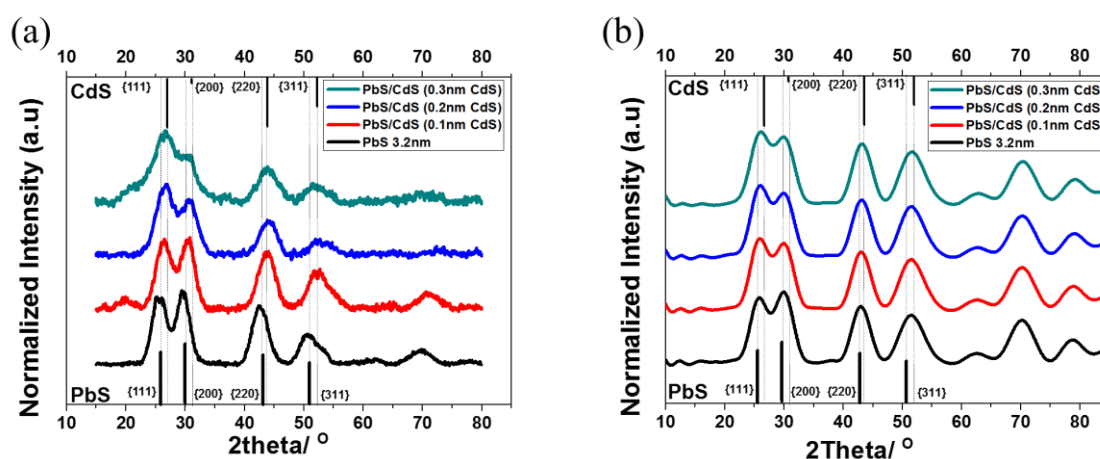
Figure 5-3. (a) Experimental X-ray diffraction patterns of PbS and PbS/CdS CQDs drop cast on glass substrates. PbS and CdS peaks are referenced from JCPDS file: #01-078-1057 and #00-001-0647 respectively. Main peaks of both PbS and CdS phases are labelled and guidelines to peaks are drawn to highlight the subtle shifts in peak position and relative intensity from PbS to CdS with increasing CdS shell thickness. (b) Simulated X-ray diffraction pattern of PbS and PbS/CdS CQD with varying shell thicknesses with an overall diameter of 3.2 nm.

To further back the proposition on the growth of an epitaxial CdS shell, simulated XRD patterns (*Figure 5-3(b)*) were calculated using a procedure based on that described

elsewhere[131]. In summary, a core/shell atomistic model (see *Figure 5-4*) was built by simulating the epitaxial growth of a CdS zinc blende shell around a PbS core with a rock salt structure using the common simple cubic positions of the rock salt and zinc blende crystal structure. Whilst the core diameter and shell thickness varied, the overall diameter of the core/shell particle was kept constant at 3.2 nm. Strain was incorporated into the atomistic model through continuum elasticity in a core/shell spherical geometry previously described[131,132]. The XRD pattern of the atomistic model was then simulated from the Debye equation for kinematic diffraction using the program 'DISCUS'[133] for a Cu K$_\alpha$ X-ray source and accounting for the thermal dependence of the scattering with Debye-Waller factors. Instrument broadening was not considered in the simulations. The parameters used for the simulation are given in

Table 5-1.
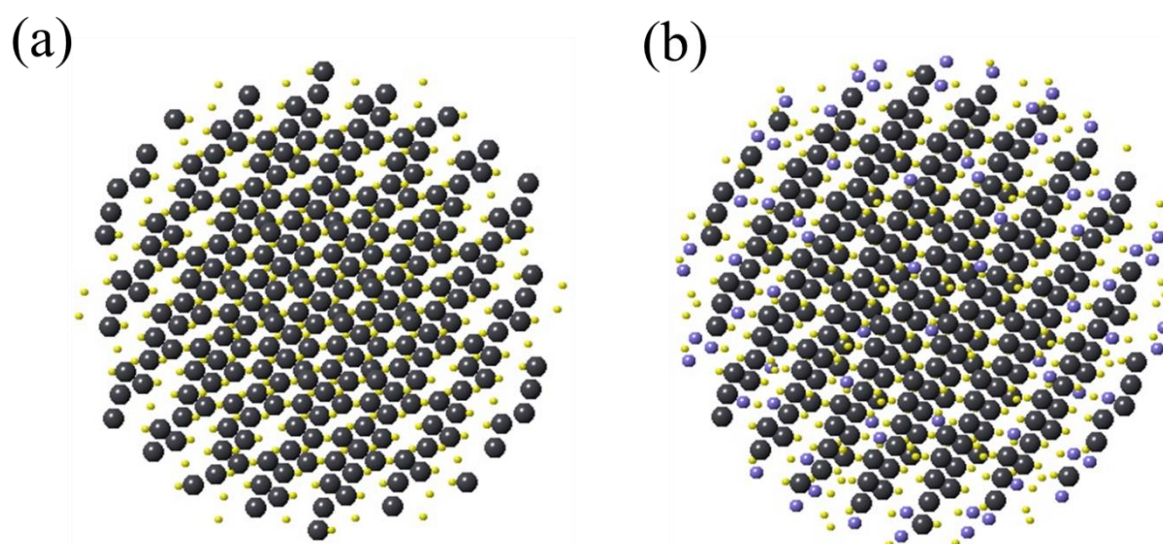
Figure 5-4. Atomistic models, built up using Crystal Maker software, of (a) PbS and (b) PbS/CdS (0.1 nm CdS) CQD. CQD models has a fixed diameter of 3.2 nm. Atomic coordinates of the models are imported into the XRD simulation program 'DISCUS'.

Table 5-1. Parameters used for XRD simulation.

	PbS (rock salt)	CdS (zinc blende)
Lattice Constant[129]	5.936 Å	5.832 Å
Young's Modulus[134]	70.20 GPa	42.00 GPa
Poisson's Ratio[134]	0.28	0.38
Shear Modulus[134]	27.42 GPa	15.22 GPa
Bulk Modulus[134]	53.18 GPa	58.33 GPa

The observed XRD result is supported by XRD simulations as illustrated in *Figure 5-3(b)*. Also, the transition of peak heights from PbS to CdS reveals the close proximity of the core and shell atoms, causing the scattered X-rays to constructively interfere between the two materials giving rise to a perceived average of the two diffraction patterns. XRD simulation of PbS/CdS core/shell CQD was constructed with the help of Dr Simon M. Fairclough.

5.2.4 Additional characterisation results for the presence of CdS shell

EDX maps out elemental composition, and examination of EDX results (in *Figure 5-5*) not only shows that core/shell PbS/CdS CQDs (with 0.1nm CdS shell) does contain Cd atoms but also show that the ratio of Cd to Pb present is approximately 1:4 (as shown in *Table 5-2.*), which agrees with the theoretical calculations as presented in section 4.2.2.
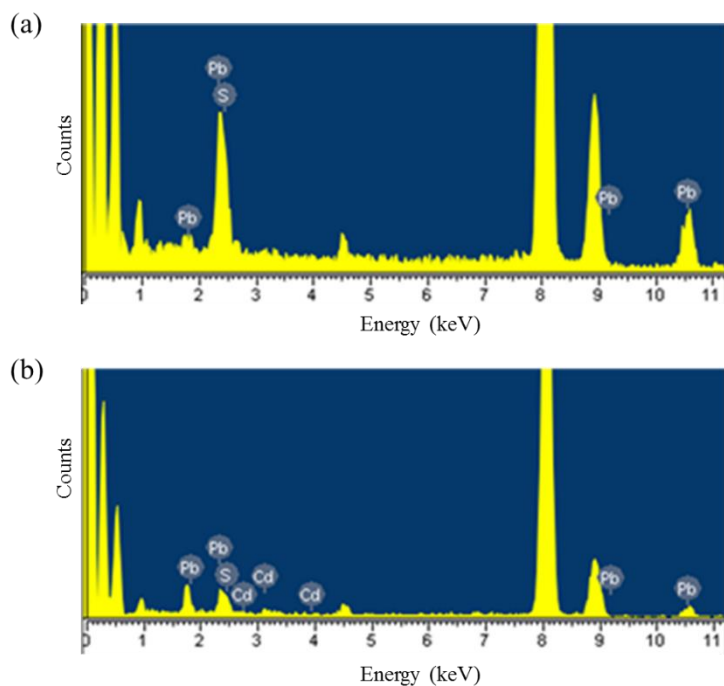
Figure 5-5. EDX map of (a) PbS CQDs (b) PbS/CdS (with 0.1nm CdS shell) CQDs

Table 5-2. Composition of elements in PbS/CdS CQD with 0.1nm CdS shell thickness, as shown in Figure 5-5 (b).

Element	Weight %	Atomic %
Cd L	13	23
Pb L	89	88
		Atomic Ratio
Totals	100.00	Cd : Pb= 3.8 : 1

Raman studies were also performed on PbS/CdS core/shell CQDs (with 0.1nm CdS shell). The results in *Figure 5-6* show that the spectrum recorded for PbS/CdS core/shell CQD film contains peaks that could be assigned to both PbS and CdS. Furthermore, the CdS

peaks are slightly red-shifted and this is consistent with the effect of a material under tensile strain, which is expected for CdS epitaxially grown on the surface of PbS.
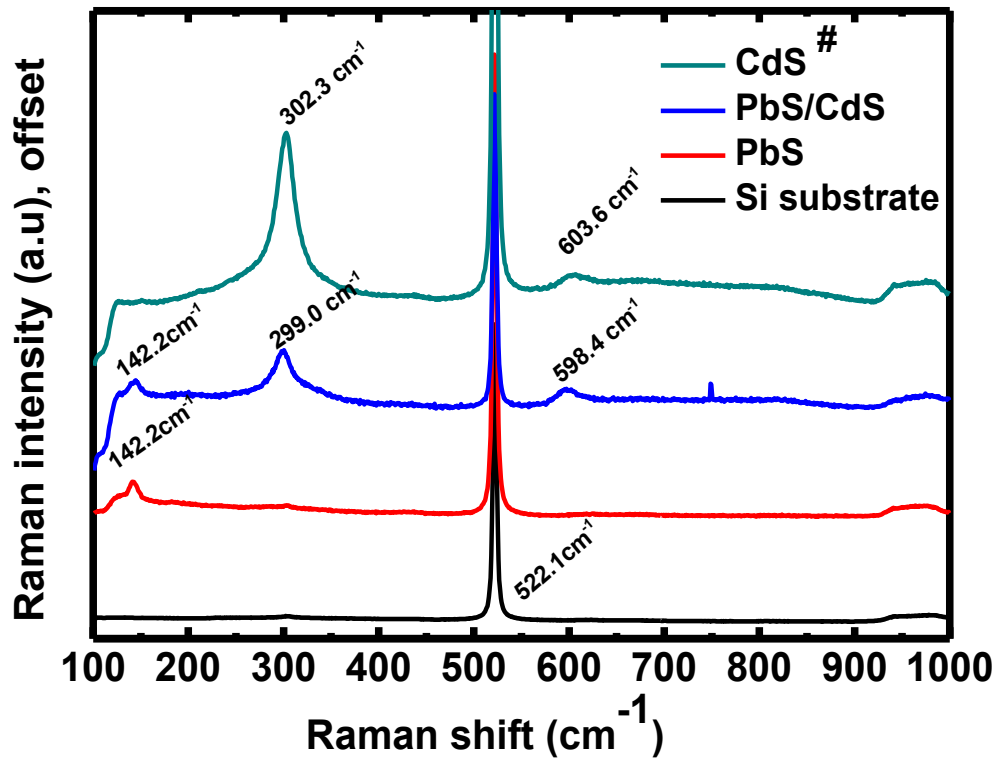
Figure 5-7. Raman spectrum of PbS/CdS versus PbS and CdS references. Peaks at ~140cm⁻¹ are not PbS but signatures of oxidised PbS[135] when exposed to the intense energy of the laser beam. #CdS formed from fine precipitates from the reaction between Cd(Ac)₂ and Na₂S. Signatures of CdS are ~300 cm⁻¹ (1LO) and ~600 cm⁻¹ (2LO). The PbS/CdS samples have a 0.1nm CdS shell thickness.

So far, techniques to probe the size and chemical composition of PbS/CdS CQD has been discussed. Absorption spectra provide an estimation to the PbS core size, and with the overall CQD diameter staying constant after cation-exchange as verified by TEM, this indirectly measures the resultant shell thickness. Then XRD with simulations, EDX and Raman spectroscopy show the presence of CdS phase and are indicative of it being an epitaxially grown shell layer. Next, to understand the effect of CdS layer on surface passivation, photoluminescence studies were carried out.

5.3.5 Photoluminescence (PL) studies

The PL spectrum as shown in *Figure 5-8(a)* supports the data from UV-Vis-NIR absorption (refer to *Figure 5-2*), which indicate a shrinking of the PbS core diameter, and therefore smaller peak emission wavelength, as shell thickness increases. Interestingly, PL peaks of core/shell CQD seemed to be composed of multiple peaks which could represent extra optical transitions due to the introduction of energy states corresponding to the CdS shell. Additionally, the graphs in *Figure 5-8(b)* together with *Table 5-3* show that the PL decay lifetime is longer for increasing shell thickness, which is consistent with that of increasing defect passivation and therefore reducing non-radiative recombination rate. A prolonged excitonic lifetime is an indicator that the faster, non-radiative, recombination channels are suppressed. It should be pointed out that the data presented for PbS/CdS with shell thicker than 0.1 nm seemed more linear than an exponential decay. PL decay illumination source wavelength was chosen based on the PL peaks gathered from *Figure 5-8(a)*. Since multiple peaks are present, perhaps there are more than one processes that are occurring and more investigation is needed for a conclusive understanding on this anomaly.
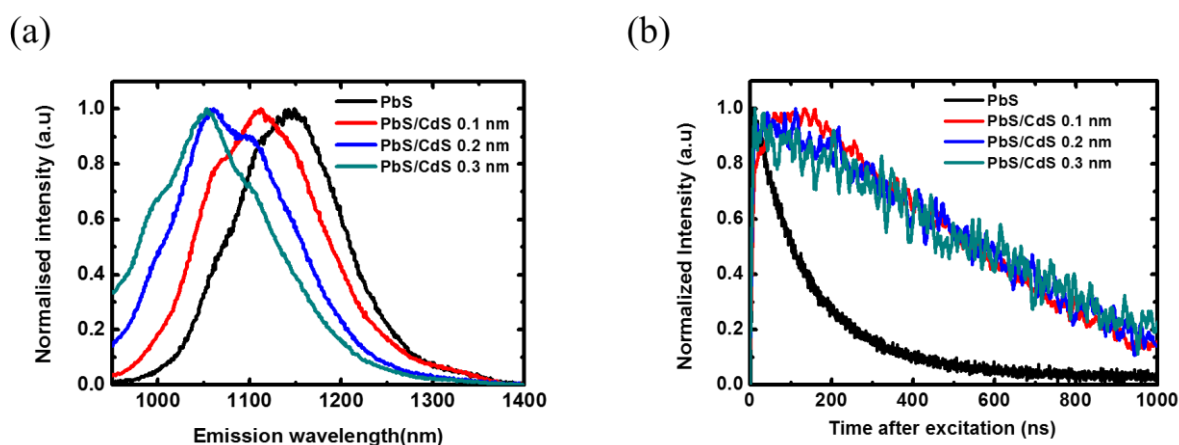
Figure 5-8. (a) Photoluminescence spectra of core/shell CQD with various CdS shell thickness versus bare PbS CQD. The samples were prepared as films on glass with no ligand treatment. (b) Corresponding photoluminescence decay graphs. Refer to Table 5-3 for fitting results.

Table 5-3. Decay time constant and pre-exponent constant from monoexponential fits.

Sample	Lifetime, τ (ns)[*]	χ^2 (reduced)
PbS	320	1.05
PbS/CdS (0.1nm shell)	1000	1.07
PbS/CdS (0.2nm shell)	1970	1.11
PbS/CdS (0.3nm shell)	2700	1.09
[*]Based on monoexponential fit: Y= A exp (-t/τ)+ B		

To further explore the shell passivation effect, PL studies were also carried on PbS and PbS/CdS (0.1nm CdS shell) CQD films before and after 1,2-ethanedithiol (EDT) ligand exchange. Oleic acid (OA) is the native ligand which is 18 carbons long while EDT is a short (2 carbon) bifunctional ligand which is known to draw PbS CQD closer together, resulting in an increase in electronic coupling but also a slight loss in quantum confinement. The effect of shell passivation is evident in two ways:

(i)   Results (see *Figure 5-9(a)*) show that with the same film thickness, before ligand exchange, PbS/CdS-OA produces a higher PL intensity than PbS-OA. The same can be said after ligand exchange (EDT). This implies that there is an effective defect density reduction conferred by CdS shell because an enhancement of radiative recombination would mean that there is a corresponding decrease in non-radiative recombination. Furthermore, for both OA and EDT as ligands, core/shell PbS/CdS CQDs display much longer decay lifetimes, typically 3 to 4 times longer than core-only PbS (see

(ii)   Figure 5-10). A prolonged lifetime is an indicator that the faster, non-radiative, recombination channels are suppressed.

(iii)   Upon closer inspection on the peak emission wavelengths (see *Figure 5-9(b)*), it is evident that PbS CQD film shows a redshift in emission after ligand exchange, which could be attributed to a loss in quantum confinement when CQDs are drawn closer to together by EDT ligands. However, when the same ligand exchange process is done on PbS/CdS CQD film, there is no appreciable redshift in emission, suggesting that passivating with CdS shell (that has a higher band gap) aids in preserving quantum confinement.
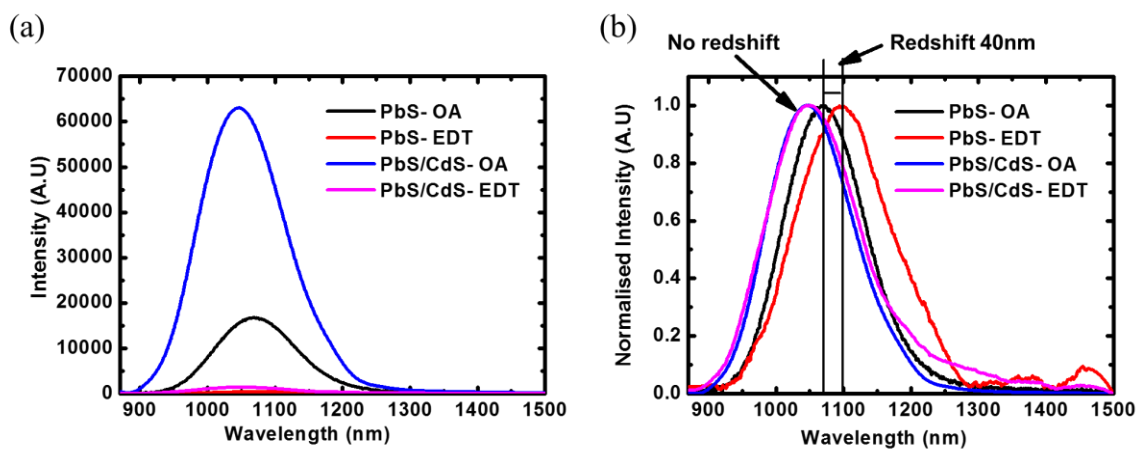
Figure 5-9. (a) Photoluminescence spectra of CQD films, showing significantly higher photoluminescence intensity of core/shell CQDs and the quenching effects of ligand exchange from OA to EDT. (b) The normalized intensity of the curves as in (a), illustrating the extent of redshift of the photoluminescence peaks.
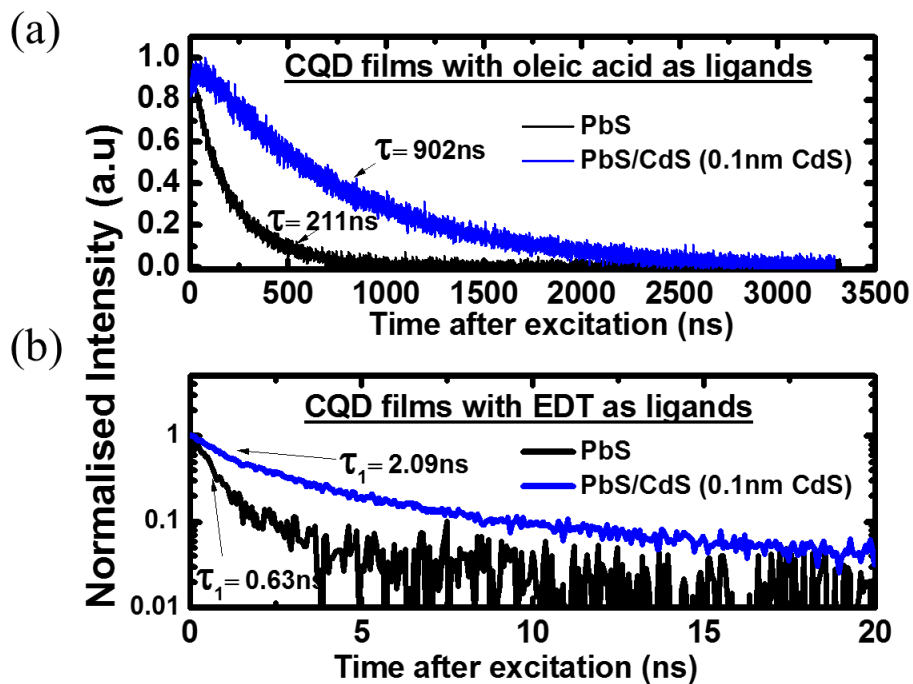
Figure 5-10. (a) Photoluminescence decay curves of the same samples described in (a). Detection wavelength for each decay curve is based on the peak emission shown in Figure 5-9. The curve fitting are based on mono-exponential decay for OA samples and bi-exponential decay for EDT samples. Refer to Table 0-4 for the values of decay time constants.

Table 5-4.Fitting and PL decay time constants for the curves displayed in Figure 5-10.

Sample	Fit	Lifetime, τ_1 (ns)	Lifetime, τ_2 (ns)	χ^2 (reduced)
PbS-OA	Mono-exponential	211	nil	1.06
PbS/CdS -OA		902	nil	1.10
PbS-EDT	Bi-exponential	0.63	7.45	1.04
PbS/CdS-EDT		2.09	16.0	1.07

To accurately confirm that the thin-shelled PbS/CdS does have an increased level of defect passivation, PLQY measurements were done, which were carried out by Mr Tom Jellicoe (see *Figure 5-11*). Comparing the absolute number of photons collected from sample emission, it is evident that PbS/CdS core/shell CQD displays more radiative recombination than PbS CQD, which in turn shows that non-radiative, defect mediated recombination is reduced in the case of core/shell CQD. However, at this stage, it is not confirmed that with the presence of CdS shell, the PbS/CdS CQD could still effectively transport charges. To directly observe the effect of shell passivation on the device performance, PbS/CdS CQD are integrated as an active layer in a solar cell device and this will be discussed in the following section.
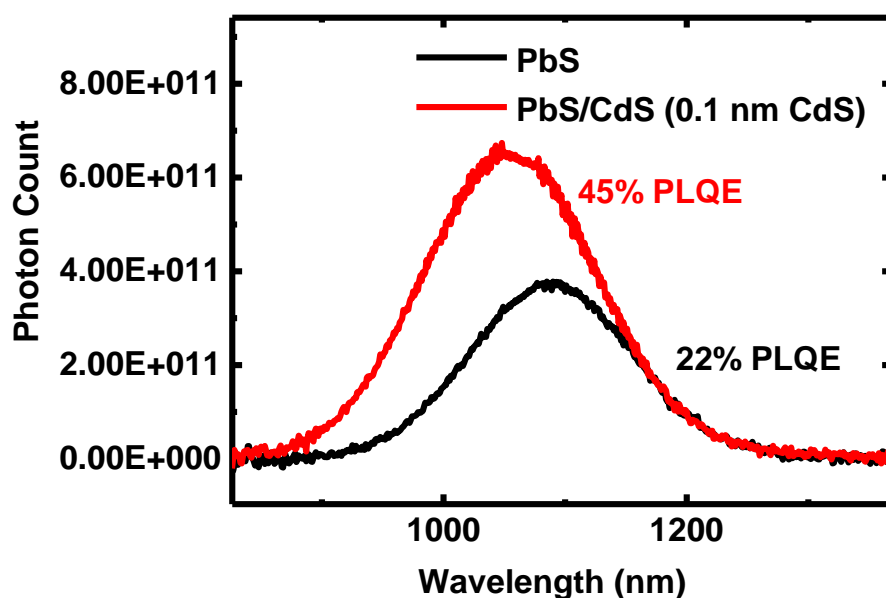
Figure 5-11. Photoluminescence quantum yield results of PbS and PbS/CdS CQD in hexane solution, showing higher absolute radiative emission of PbS/CdS compared to PbS. The blueshift in the emission peak is due to the slightly smaller core PbS size (2.9 nm) of PbS/CdS CQD compare to the PbS CQD (3.1 nm).

5.3 Incorporation of PbS/CdS CQD into solar cell devices

In this section, devices are constructed based on PbS/CdS (with 0.1nm CdS shell) as the active layer, and with PbS devices as the reference. The main results are focussed on CQD-ZnO heterojunction devices but to show that the PbS/CdS CQD works regardless of device configuration, the simplest photovoltaic device architecture – the Schottky junction device, is also fabricated.

5.3.1 Device fabrication

5.3.1.1 Schottky devices

PbS and PbS/CdS CQD films were deposited using a layer-by-layer spin-coating process with an in-situ solid-state ligand exchange process, carried out in an ambient atmosphere. Substrates were prepared by pre-patterning ITO on glass, spin coating a layer of PEDOT:PSS at 5000 rpm for 30 s and then annealing at 150°C for at least 5 minutes before use. For each layer, 10 μL CQD solution (50 mg/ml in octane) was deposited onto the spinning substrate, with a spin rate of 2000 rpm, followed by 20 μL of 1% v/v EDT in methanol. While spinning, 60 μL of methanol were added followed by 60 μL of octane to wash off unbound ligands and CQDs. This cycle was repeated to build up to the required thickness. All samples were standardized to have 4 layers of CQD deposited, which gave a thickness of about 120 ± 15 nm as measured by a surface profilometer. Top aluminium contacts (120nm) were deposited by thermal evaporation as described in chapter 4. The device structure is illustrated in *Figure 5-12(a)*.

5.3.1.2 Heterojunction devices

The exact same spin coating process for Schottky devices is repeated here but samples were standardized to have 5 layers of CQD deposited instead of 4, measuring about 150 ± 17 nm thick. This is because the limitations of a Schottky junction, which includes Fermi level

pinning effect and thus a limited depletion width[136], are overcome by adopting a heterojunction structure. The *n*-type material also acts as a hole blocking area, reducing recombination. These afford the CQD active layer to be thicker than that of Schottky cells. Then before the deposition of the metal contact, an *n*-type layer (of 107 ± 19 nm) was deposited by spin coating ZnO CQD solution on top of the as-prepared film at 2000 rpm for 30 s. Similarly, top aluminium contacts were deposited by thermal evaporation. The device structure is illustrated in *Figure 5-12(b)*.
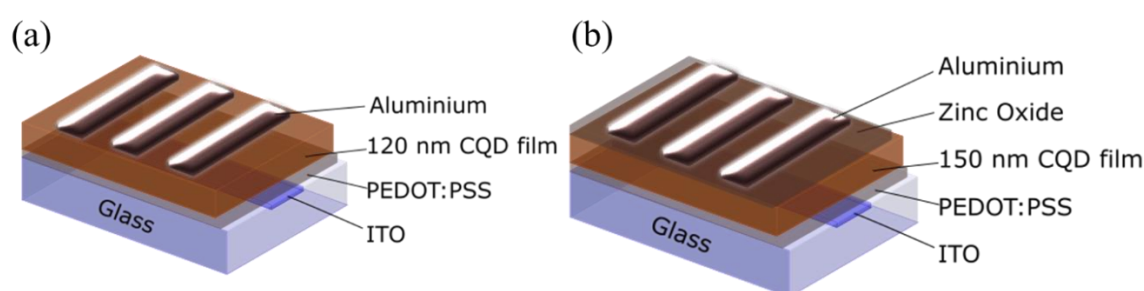
Figure 5-12. (a) Schottky junction solar cell and (b) heterojunction solar cell device structure

5.3.2 Results and analysis

PbS and PbS/CdS – ZnO heterojunction solar cell devices were first fabricated and tested. The current density-voltage (*J-V*) characteristic curves in *Figure 5-13* reveal that although the short-circuit current (J_{sc}) is substantially lower for the PbS/CdS device, V_{oc} exceeds that of the non-shelled PbS device by more than 0.2 V. A PbS band-gap change of 0.08 eV from 1.26 eV to 1.34 eV (as would be predicted using the method of Yoon et al.[58] , in this work moving from a PbS to a PbS/CdS CQD with 0.1 nm shell thickness) would result in only a 0.044 V change in V_{oc} if it were due only to an increase in band offset. Hence, the greater increase of V_{oc} observed must be due to additional factors. Using dark and illuminated *J-V* curves to estimate the built-in potential and comparing it with V_{oc}, it is clear that the PbS devices suffer a greater voltage loss than the PbS/CdS devices. Zhao

et al.[137] have reported a similar improvement in V_{oc} resulting from a post-deposition annealing treatment of a PbS CQD film, which forms a thin layer of oxide on the surface of PbS. However, the thickness of the oxide layer is harder to control and might promote further oxidation if the film is left to be exposed to air ambient. Similarly, the thin CdS shell layer would effectively passivate surface defects of the PbS core because cation-exchange relies on the replacement of the original host cationic species resulting in the complete bonding of every PbS surface atom. Therefore, deleterious deep traps that promote non-radiative recombination are minimized and this gives a rise in V_{oc} [138].

To confirm that the improvement in V_{oc} originates from the core/shell passivation strategy, a set of CQD devices fabricated using an aluminium metal Schottky junction instead of ZnO were tested. Results from these show that, even without a *p-n* junction, shell passivation is effective as V_{oc} increase from 0.33 V to 0.54 V (See *Figure 5-14*).
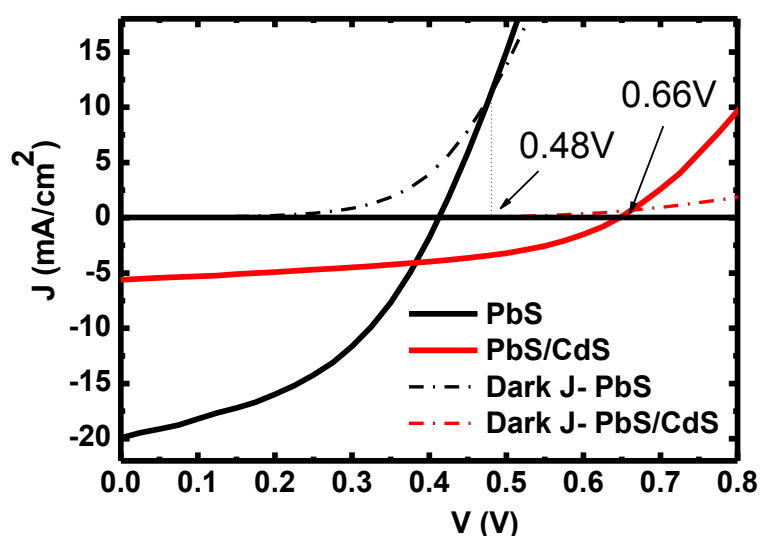
*Figure 5-13. Current density versus voltage performance testing of best performing devices under dark and AM1.5 illumination conditions. Both devices have the same structure, with similar thickness and underwent the same solid state ligand exchange process using EDT. Arrows indicate the voltage points where light generated current equals the dark current and gives an estimate of the built in potential of the device. Refer to **Error! Reference source not found.** for a summary of the average performance statistics.*
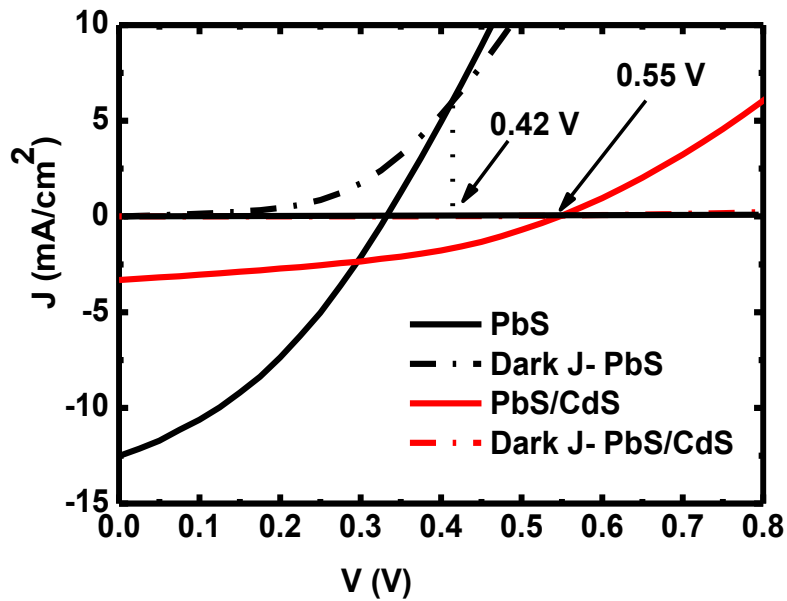
Figure 5-14. Current density versus voltage performance testing of best performing Schottky devices under dark and AM1.5 illumination conditions. Both devices have the same structure, with similar thickness and underwent the same solid state ligand exchange process using EDT. Arrows indicate the voltage points where light generated current equals the dark current and gives an estimate of the built in potential of the device. Refer to Table 5-6 for a summary of the average performance statistics.

Table 5-5. Performance data for heterojunction CQD solar cells (ITO/PEDOT:PSS/CQDs/ZnO/Al) under AM 1.5 spectral illumination (100 mW/cm^2).

Sample	J_{sc}(mA/cm^2)	V_{oc} (V)	FF	PCE (%)	J_o(mA/cm^2)	R_s (Ωcm^2)	R_{sh} (Ωcm^2)
PbS	17.9 ± 3.5 (19.8)	0.41 ± 0.09 (0.42)	0.45 ± 0.06 (0.44)	3.40 ± 0.22 (3.66)	$(1.2 ± 0.7) × 10^{-3}$	6.52 ± 0.93	55.5 ± 14.2
PbS/CdS (0.1 nm CdS shell)	5.9 ± 1.4 (6.2)	0.65 ± 0.04 (0.65)	0.42 ± 0.06 (0.42)	1.37 ± 0.28 (1.69)	$(1.3 ± 0.3) × 10^{-5}$	23.9 ± 4.3	324 ± 14
Results are averaged with standard deviation across 9 samples on 3 different substrates. The J_{sc}, V_{oc}, FF and PCE of champion devices are quoted in brackets.							

Table 5-6. Performance data for Schottky CQD solar cells (ITO/PEDOT:PSS/CQDs/Al) under AM 1.5 Spectral illumination (100 mW/cm^2).

Sample	J_{sc}(mA/cm^2)	V_{oc} (V)	FF	PCE (%)	J_o(mA/cm^2)	R_s (Ωcm^2)	R_{sh} (Ωcm^2)
PbS	10.2 ± 2.6 (12.1)	0.33 ± 0.04 (0.33)	35 ± 3 (0.34)	1.22 ± 0.11 (1.36)	$(6.2 ± 0.3) × 10^{-3}$	14.5 ± 0.7	62.5 ± 17.3
PbS/CdS (0.1 nm CdS shell)	2.9 ± 0.8 (3.3)	0.51 ± 0.03 (0.54)	40 ± 3 (0.41)	0.71 ± 0.14 (0.73)	$(2.0 ± 0.4) × 10^{-4}$	59.7 ± 2.5	473 ± 18
Results are averaged with standard deviation across 9 samples on 3 different substrates. The J_{sc}, V_{oc}, FF and PCE of champion devices are quoted in brackets.							

5.4 Effect of shell thickness

To maximize the benefit of shell passivation, in the context of solar cell devices, the shell thickness has to be optimized such that it is sufficiently thick for complete passivation, yet sufficiently thin for charges to be transported dot to dot. Using the same starting core PbS CQD, a series of core/shell CQDs with increasing shell thicknesses was examined using the same procedure. *Figure 5-15* shows *J-V* curves with respect to increasing shell thickness and it clearly shows that J_{sc} decreases with increasing shell thickness. Since the device active layer is kept to around the same thickness, it could be said that the drop in J_{sc} arises from the thicker CdS shell impeding charge flow, thereby limiting the amount of charge extracted even with the same amount of illumination. Additional device metrics are derived from the light and dark *J-V* curves and they are summarised in *Figure 5-16* which also demonstrate the effect of shell passivation as discussed in the next two paragraphs.

Results indicate an increase in V_{oc} with increasing shell thickness, with the most substantial change between no shell and a 0.1 nm shell. Ip *et al.*[110] showed that a reduction of surface related trap density increases V_{oc} by exploring the effect of mid-gap trap states using density functional theory simulations. It is most likely, that at 0.1 nm shell thickness, surface passivation by CdS is sufficient. Thus, additional thickness of CdS do not lead to a substantial increase in passivation and the subsequent rise in V_{oc} is smaller (going from 0.1 nm to 0.2 nm to 0.3 nm shell thickness) and is mostly attributed to the increase in band-gap due to the decrease in PbS core diameter[58]. With reference to *Figure 5-2* , PbS/CdS CQD with 0.1 nm shell as compared to PbS CQD has a band gap increment of 0.08 eV while V_{oc} increases by 0.25 V but as with PbS/CdS CQD with 0.3 nm shell, band gap increment is 0.21 eV while V_{oc} only increases by 0.36 V.

R_{sh} for shell passivation and as the shell thickness increases, J_0 and R_{sh} continue this trend, likely associated with a reduction in overall charge transport, due to the increased quantum confinement imposed by a pure-phase CdS shell and hence reduced delocalization of electronic wavefunctions across neighbouring quantum dots[124]. This is also evident from the rise in series resistance (R_s).

Passivation of defect states can also lead to a lower carrier concentration as the CQD becomes more intrinsic in nature, thereby reducing conductivity and hence increasing the overall series resistance[137]. It has also been reported that cation-exchange tends to be less uniform when thicker shells are formed, i.e. shell growth may be preferential at a certain crystal facet, giving rise to a broader excitonic peak[117] as observed in *Figure* 5-2, and this could be detrimental to device performance[41]. Core/shell CQDs with CdS shells less than 0.1 nm were also synthesized and evaluated as possible solar cell devices but gave no distinct improvement to V_{oc}. Therefore, it could be said that 0.1 nm CdS shell is the thinnest shell layer that can achieve sufficient surface passivation, which is regarded as optimal and further investigation was carried out using this particular core/shell PbS/CdS size.
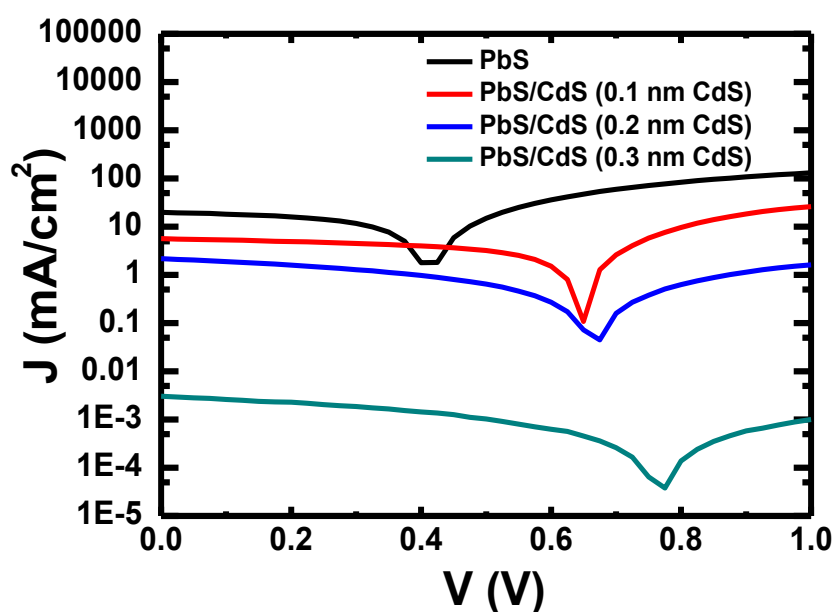
Figure 5-15. Current density versus voltage performance testing of best performing devices under AM1.5 illumination conditions. All devices have the same structure, with similar thickness and underwent the same solid state ligand exchange process using EDT.
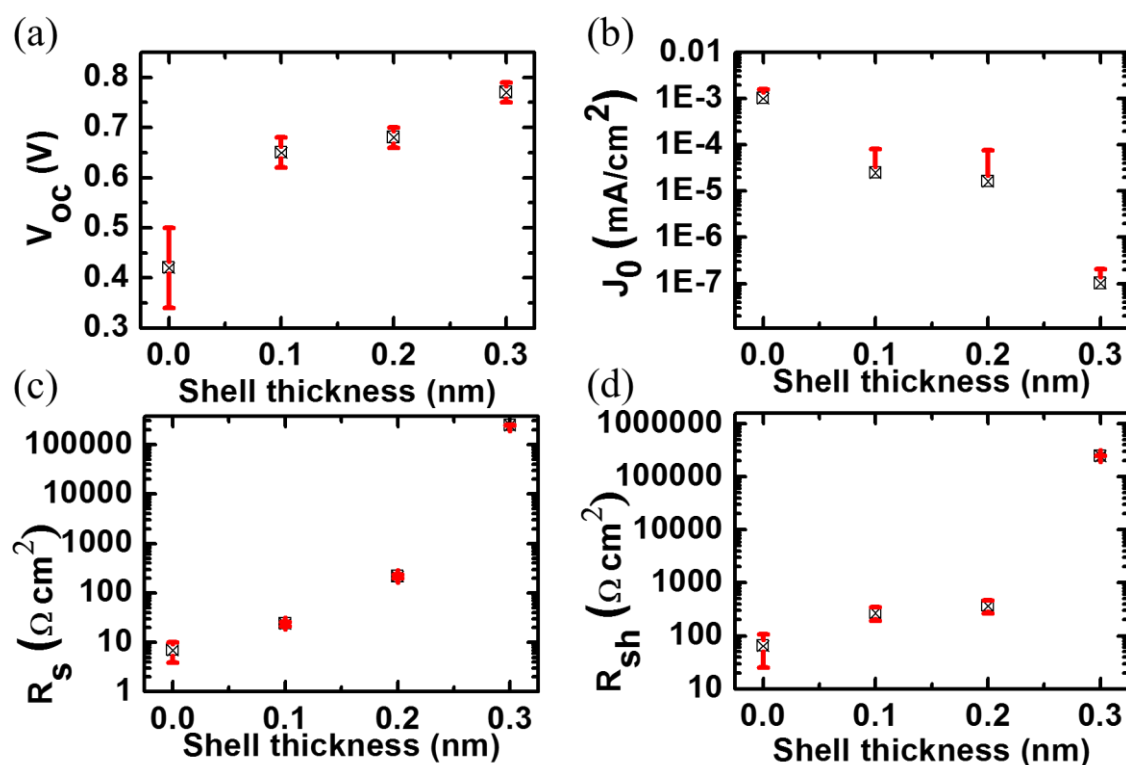
Figure 5-16. (a) Open circuit voltage, (b) Reverse saturation current, (c) Series resistance, (d) Shunt resistance versus thickness of CdS shell layer on PbS/CdS core/shell CQDs. 0 nm shell thickness refers to unshelled PbS CQD and all PbS/CdS CQDs are synthesized from the same batch of PbS.

5.5   Relaxation of charge transport barrier

The benefits of having a passivating CdS shell is illustrated on the band diagrams in *Figure 5-17*. The alignment and the subsequent band bending promotes electron injection from PbS CQD into the ZnO conduction band. Charge carriers might be lost through non-radiative recombination via traps caused by surface defects, which occurs between the

quantum dots as well as across an interface. Therefore, employing core/shell PbS/CdS CQDs may well be an important step forward in addressing the issues with solid state ligand exchanges as mentioned in the introduction, like incomplete passivation. However, it is also apparent (from the figure) that the CdS shell forms an energy barrier which slows charge transport between CQDs.
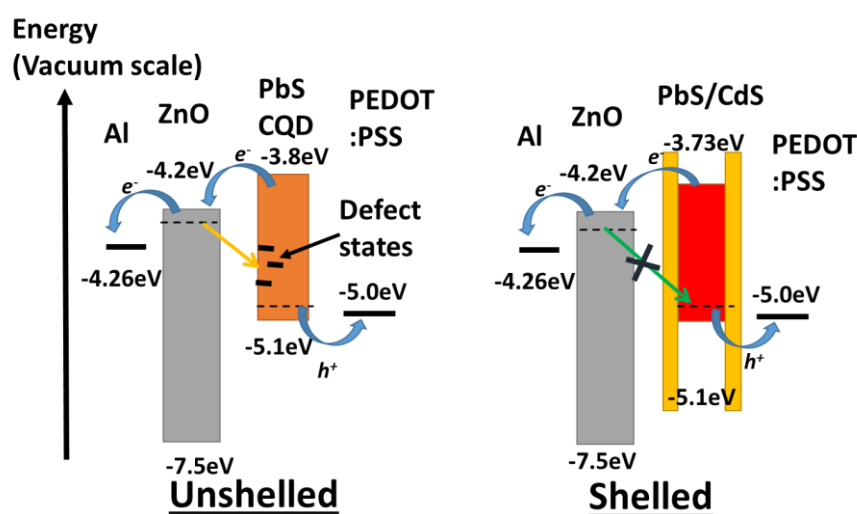
Figure 5-17. Schematic diagram showing the proposed band alignment of the heterojunction cell and the defect mediation effect of a CdS shell on the PbS electronic structure. Defect states promotes non-radiative recombination when charges moves between CQDs or between PbS and ZnO interface. Adding a CdS shell reduces recombination, thus improving V_{oc}.

Our preliminary results confirm that shell passivation comes at the price of lowering charge transport efficacy as shown by the lower overall photocurrent harnessed and the greater series resistance. Charges now have to tunnel through both the shell and the ligand matrix to neighbouring CQDs to make their way to the respective electrodes. EDT, being a bi-functional linker, draws the CQDs closer together and enhances coupling between the quantum dots[114]. However, even with EDT ligands, our observations from photoluminescence studies imply that energetic coupling amongst core/shell CQDs is less

significant compared to their non-shelled counterparts as shown by the minimal redshift of the photoluminescence emission peak. Therefore, to improve charge transport in an array of core/shell CQDs it is necessary to further decrease inter-dot distance or to relax the confinement potential of CdS shell by changing its surface chemistry.

5.5.1 Halide ligand exchange

Two classes of inorganic ligands have been reported to produce CQD films with high carrier mobility, namely metal chalcogenide complexes[76,77] and small molecular[139,140] or atomic ligands[85,141,142]. In this work, halide atomic ligands are investigated since they have been shown to increase the efficiency of PbS CQD devices[65,67]. According to the methodology developed by Tang *et al.*[67], the use of these halide ligands requires a cadmium cation and a long chain phosphonic acid molecule conjugation to deliver the halide ligand to the PbS surface. It was noted through absorption studies that a complete cadmium shell is not formed as cadmium binds only to exposed sulphur atoms and the rest of the exposed lead atoms are bonded to the halide atoms.

Tang *et al.* have also shown that different halide ligands gave different mobility results with the trend being that mobility increases from chlorine, through bromine to iodine. Interestingly, studies have also shown that when halide treatment was performed on PbS without cadmium, PbS with *n*-type character is produced[115]. With cadmium incorporation, the formation of donor states seems to be suppressed while carrier mobility is improved, in similar fashion to atomic ligand passivation[67]. From this, it could be hypothesized that with a cadmium sulphide layer on PbS for our core/shell CQD, there could be a similar effect of improving carrier mobility while reducing the influence on PbS core electronic structure. A more recent work suggests that the thicker the CdS shell, the less influence the ligand has on electron wavefunction[143], showing that the presence of a CdS shell will change how ligands affect the core's electronic structure. To investigate the effect of halide ligands, PL

studies were conducted and PbS/CdS devices were fabricated based on halide ligand exchanges.

5.5.1.1 Alterations to spin coating procedure

To maximize device performance, a halide surface treatment was carried out[67,110], using cadmium chloride (CdCl$_2$) for the chlorine (Cl) source and cetyltrimethylammonium bromide (CTAB) for the bromine (Br) source, on our PbS/CdS (0.1 nm CdS shell) CQD films. In the halide treatment approach, after each layer of PbS/CdS CQD solution was coated, the substrate was stopped from spinning and solid-state ligand exchange was performed by covering the surface of PbS/CdS film with saturated CdCl$_2$ in methanol for Cl exchange and 10 mg/ml CTAB in methanol for Br exchange, over a period of one minute. The sample was then spun dry at 2000 rpm before 60 μL of methanol weas added to wash off excess CdCl$_2$ or CTAB solution. For each layer of PbS/CdS CQD deposited, this procedure was repeated three times before the next layer was deposited, so as to ensure comprehensive ligand exchange. A total of 5 layers were deposited this way which amounts to a CQD film thickness of about 150 nm, before the ZnO layer was deposited. The devices have the same structure as shown in *Figure 5-12(b)*.

5.5.1.2 Results and analysis

Before devices were fabricated, a series of PbS/CdS CQD films of similar thickness were formed with different ligand treatments by spin coating on PEDOT:PSS coated glass substrates. Samples were prepared with and without a ZnO top layer and were studied using PL measurements. PL data (see *Figure 5-18(a)*) show that, without the ZnO layer, halide ligands provide approximately the same level of surface passivation as EDT on the surface of PbS/CdS CQD. This is concluded because they have similar PL intensity with similar film thickness (i.e., no extra non-radiative recombination channels). However, when the

ZnO layer was added, halide ligands show a drop in luminescence intensity, with Br showing a more drastic drop than Cl, while EDT ligand shows the converse.

Photoluminescence quenching is a useful measure to show that charge separation is occurring at an interface[144]. In this case, it could be said that halide ligands promote electron transfer from PbS/CdS into ZnO, thereby reducing the number of free electron-hole pairs in the PbS/CdS CQD layer to radiatively recombine. Also, it is clear that Br enables a more efficient charge transport than Cl as can be inferred from the larger extent of the quenching effect. The anomaly of an increase in PL intensity is explained by the work of Rath *et al*[96]. They have shown the high electron concentration of ZnO results in active movement of electrons into PbS to fill up trap states, thereby reducing losses due to non-radiative recombination. Hence, it could be said that halide ligands help to delocalise electron wavefunction effectively, even at the PbS/CdS and ZnO interface, while EDT might reinforce the confinement effect.

The effect of halide ligands is echoed in PbS/CdS device performance (See *Figure 5-18(b)*). In fact, the delocalization effect rendered by Br ligands is so great that the shell passivation effect is overcome. Recent studies by Brown *et al*. show the effect of different ligands on the Fermi level of PbS[88]. It was concluded that the ligands assert a dipole effect on PbS, thereby shifting the Fermi energy level. Halide ligands cause the Fermi level in PbS to shift closer to the conduction band and the trend is that the larger the halide size, the larger the dipole moment (due to larger inter-nuclear distances), the closer the Fermi level is to the conduction band. Even more recently, it was shown that a halide (iodide) ligand introduces defect states, thereby limiting V_{oc} but improving charge transport[48]. There could be a similar effect when halide ligands bind to the surface of PbS/CdS CQD. Thus, in summary it can be said that the greater the charge delocalization from EDT to Cl to Br, more charges are being extracted and therefore the higher the J_{sc} values while V_{oc} values decrease due to

a loss in confinement potential. To further improve charge transport without losing much of the passivation effect of the shell, a balance is sought between the barrier reinforcement effects of EDT and the barrier relaxation effects of halide treatment.
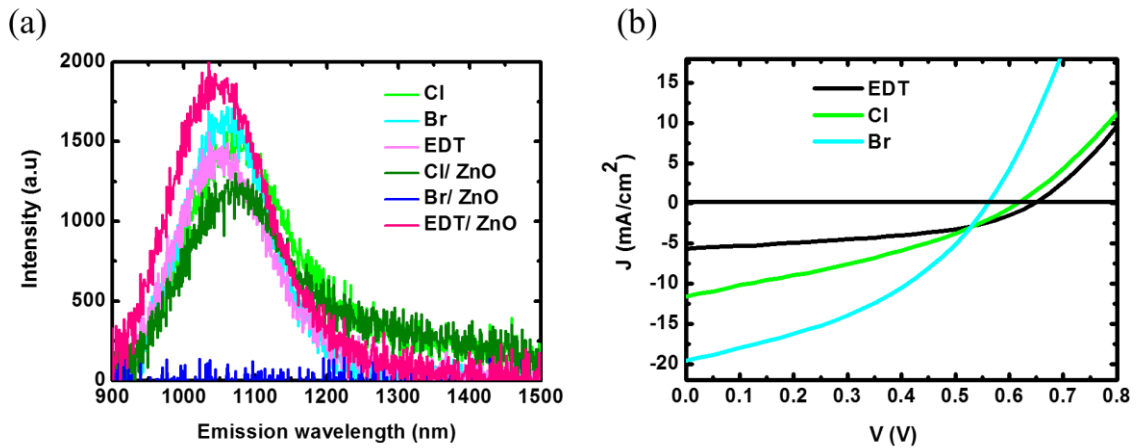
Figure 5-18. (a) Photoluminescence spectra of CQD films, prepared with similar thicknesses, after halide ligand exchange. EDT treated films are added as reference. Films prepared with an extra layer of ZnO deposited on top (as in test device fabrication) are labelled in darker shade of the same colour (b) Current density versus voltage performance testing of the best PbS/CdS devices formed from different halide ligand exchange treatments with EDT ligand exchange sample shown as reference. Refer to Table 5-7 for the device performance statistics.

5.5.2 Hybrid ligand exchange

Ip *et al.* have reported a passivation technique that relies on the use of both organic bi-functional linkers and inorganic halide ligands on PbS CQD for solar cell fabrication[110]. In a similar spirit, EDT and halide ligands could be used synergistically to promote charge transport between PbS/CdS CQDs while at the same time preserving the effect of CdS shell passivation. Furthermore, Ip *et al.* also noticed that the average spacing between quantum dots is much smaller when organic bi-functional linkers are used as compared to purely

inorganic halide ligands[110], suggesting that the use of EDT may enhance the wavefunction delocalisation effect of halide ligands by increasing the proximity between quantum dots. To test this, the spin coating process was adjusted to incorporate dual ligand exchanges. It was observed using FTIR that a single halide flooding step is not sufficient to replace all of the oleic acid native ligand (See *Figure 5-19*). With that knowledge, the remaining oleic acid ligand could be replaced with EDT.
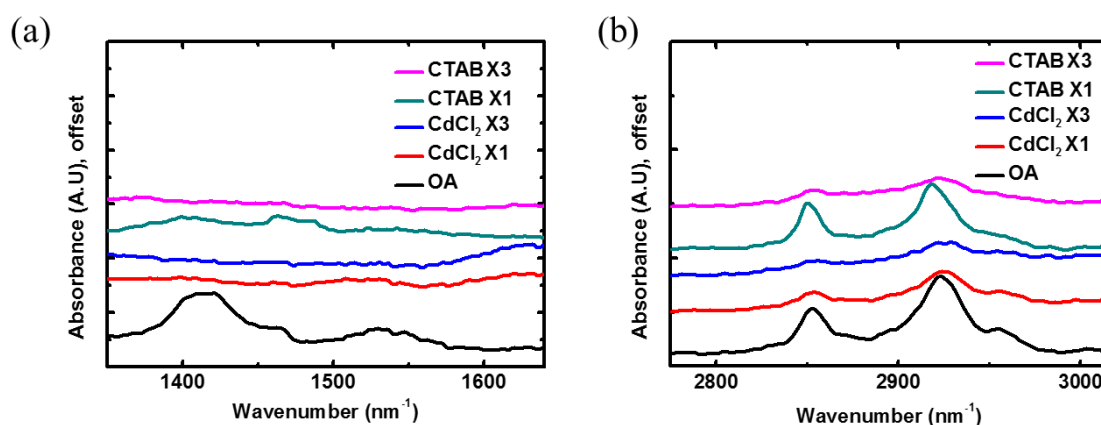
Figure 5-19. FTIR result showing signature peaks of bound oleic acid of (a) COO⁻ and (b) C-H hydrocarbon backbone. OA refers to PbS/CdS CQD with oleic acid ligand (with no ligand exchange) and CTAB X1 refers to PbS/CdS CQD subjected to one CTAB flooding step while CTAB X3 refers to three consecutive flooding steps, etc. Results illustrate that one halide ligand flooding step is not sufficient to remove all bound oleic acid ligands.

5.5.2.1 Alterations to spin coating procedure

In the hybrid ligand exchange approach, the same flooding procedure is followed as in section 5.5.1.2 but was carried out once instead of three times for each PbS/CdS layer to avoid complete ligand exchange (See *Figure 5-19*). After one minute of the halide treatment, the sample was spun dry at 2000 rpm and 60 μL of methanol were added. While spinning, this procedure was followed by 10 μL of 1% v/v EDT in methanol and then 60 μL of methanol and 60 μL of octane. This completes one layer of PbS/CdS CQD

film for the hybrid ligand exchange approach. A total of 5 layers are deposited this way and the total CQD film thickness was about 150 nm before the ZnO layer was deposited. Devices have the same structure as shown in *Figure 5-12(b)*.

5.5.2.2 Results and analysis

Likewise, PL studies were conducted (with PbS/CdS CQD samples on PEDOT:PSS coated glass substrate) to study the effect of hybrid ligand treatment. Results show that even before the ZnO layer was deposited, CQDs with Br + EDT hybrid treatment showed PL quenching. This might be due to the synergistic effect of EDT bringing the CQD closer together and Br relaxing the barrier energy, enabling holes to transported to the underlying PEDOT:PSS layer. Cl + EDT treatment, on the other hand, showed a completely different behaviour. The PL intensity is at a level that is higher than EDT treatment alone. To understand this, the EDX spectrum of PbS/CdS (0.1 nm CdS) after Cl ligand exchange was examined. It was noted that the Cd to Pb ratio rises after Cl ligand exchange, which means that $CdCl_2$ not only supplies Cl atoms as ligands but could also increase the CdS shell thickness slightly, therefore increasing the passivation effect and hence the higher PL intensity. No quenching was observed when a ZnO layer was added, signifying the effectiveness of EDT in preserving shell passivation.

Device *J-V* performance results are shown in *Figure 5-20(b)* and *Table 5-7*. Using a combination of both halide and EDT ligands would result in a concomitant increase in both J_{sc} and V_{oc} with respect to a halide-only treatment. Even though Cl + EDT treatment gave the highest V_{oc}, J_{sc} was limited and series resistance was high, which could be attributed to the effect of increased passivation. In the end, the combination of Br + EDT gave the optimal result of both a suitable extent of shell passivation (retention of higher V_{oc}) and better charge transport properties (higher J_{sc} and *FF*), in which the best device

has an efficiency of 6.05 %. *Figure 5-21* summarises the concept of halide and hybrid

ligand exchange on PbS/CdS core/shell CQD.
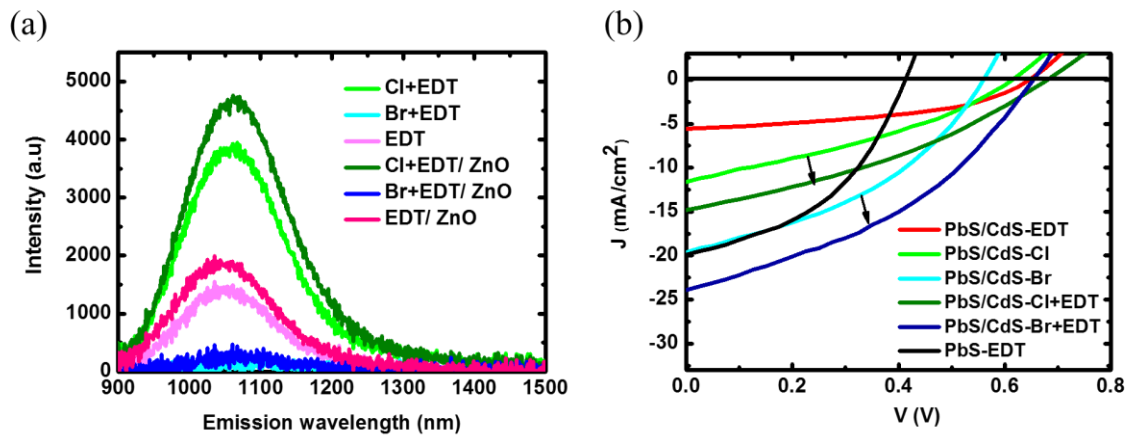
Figure 5-20. (a) Photoluminescence spectra of CQD films, prepared with similar thicknesses, after hybrid ligand exchange. Films prepared with an extra layer of ZnO deposited on top (as in test device fabrication) are labelled in darker shade of the same colour. EDT treated films are added for reference. (b) Current density versus voltage performance testing of the best PbS/CdS devices formed from different ligand exchange treatments with a PbS device performance shown as reference. Arrows highlight the improvement of hybrid treatment over standalone halide treatment for ligand exchange. Refer to Table 5-7 for the device performance statistics.

Table 5-7. A summary of performance data for heterojunction CQD solar cells (ITO/PEDOT:PSS/CQDs/ZnO/Al) under AM 1.5 Spectral illumination (100 mW/cm²).

	Ligand	J_{sc} (mA/cm^2)	V_{oc} (V)	FF	PCE (%)	J_o (mA/cm^2)	R_s (Ωcm^2)	R_{sh} (Ωcm^2)
PbS	EDT	17.9 ± 3.5 (19.8)	0.41 ± 0.09 (0.42)	0.45 ± 0.06 (0.44)	3.40 ± 0.22 (3.66)	(1.2 ± 0.7) × 10^{-3}	6.52 ± 0.93	55.5 ± 14.2
PbS/CdS	EDT	5.9 ± 1.4 (6.2)	0.65 ± 0.04 (0.65)	0.42 ± 0.06 (0.42)	1.37 ± 0.28 (1.69)	(1.3 ± 0.3) × 10^{-5}	23.9 ± 4.3	324 ± 14
	Cl	11.2 ± 2.3 (11.8)	0.63 ± 0.03 (0.61)	0.33 ± 0.04 (0.33)	2.16 ± 0.14 (2.38)	(6.3 ± 0.4) × 10^{-5}	23.6 ± 3.5	69.9 ± 6.3
	Br	17.4 ± 1.2 (19.4)	0.54 ± 0.04 (0.55)	0.39 ± 0.02 (0.39)	3.83 ± 0.30 (4.16)	(5.0 ± 0.4) × 10^{-4}	10.1 ± 2.4	61.0 ± 4.8
	Cl+ EDT	13.8 ± 1.9 (14.8)	0.66 ± 0.03 (0.68)	0.34 ± 0.03 (0.34)	3.12 ± 0.22 (3.42)	(9.4 ± 0.5) × 10^{-5}	24.9 ± 3.3	76.2 ± 5.4
	Br+ EDT	21.9 ± 2.4 (23.9)	0.63 ± 0.04 (0.65)	0.38 ± 0.03 (0.39)	5.61 ± 0.38 (6.05)	(2.0 ± 0.4) × 10^{-4}	11.8 ± 2.6	58.1 ± 3.9

PbS/CdS CQD is with 0.1 nm CdS shell. Results are averaged with standard deviation across 12 samples on 4 different substrates. The J_{sc}, V_{oc}, FF and PCE of champion devices are quoted in brackets.
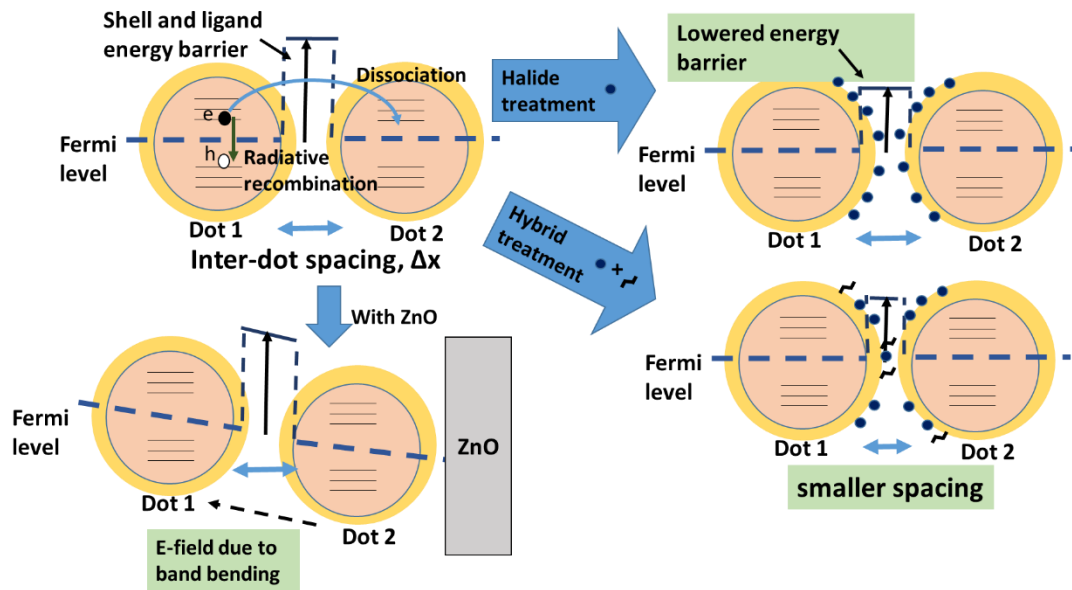
Figure 5-21. Schematic diagram illustrating the competing effect between radiative recombination and electron-hole pair dissociation. Dissociation is aided by a lowering of energy barrier for transport, the reduction of inter-particle spacing and also the band bending effect resulting from a heterojunction formation.

5.6 Conclusion

In conclusion, a cation-exchange method has been developed to produce PbS/CdS core/shell CQD with a thin shell. By controlling the precursor concentration and reaction times, it is possible to have very fine control of CdS shell thickness. TEM reveals no separate CdS phase formation and no obvious size difference statistically, which supports the cation-exchange mechanism. The shell thickness has been probed indirectly by utilizing absorption spectroscopy and XRD coupled with simulation, while its composition is ascertained by EDX analysis and Raman studies. Additionally, the effectiveness of PbS surface passivation by the CdS shell can be shown by increased PL decay lifetime, which indicates a reduction in the concentration of defect states.

The core/shell PbS/CdS CQD was then incorporated into devices and the effect of passivation on device performance is elucidated in terms of V_{oc} improvements. The effect of shell thickness on device performance was then studied and it was determined that 0.1nm of CdS shell thickness is optimal. Lastly, to overcome the charge extraction barrier as imposed by the CdS shell, different ligand exchanges were carried out. It was shown that a combination of EDT and Br ligand helps to both draw the CQDs closer and preserve the shell passivation effect to improve charge extraction. This novel work presents a method to obtain a balance between preserving the passivation effect and improving charge transport. With this, PbS/CdS devices averaging 5.6 ± 0.4 % efficiency were obtained, presenting a significant improvement when compared with 3.4 ± 0.4 % efficiency of the reference PbS devices.

Chapter 6 – Novel device architecture with PbS/CdS core/shell CQD

This chapter presents the use of PbS/CdS core/shell nanocrystals, in two different and novel device structures. Part of this thesis chapter was published in *MRS Proceedings (2014), Volume 1748, Symposium II* as a contribution to Material Research Society Fall 2014 conference and examines the use of PbS/CdS in a *p-i-n* structure. The manuscript for the proceeding was prepared by Darren C. J. Neo with the help of Prof. Hazel E. Assender and Prof. Andrew A. R. Watt. Another part of this chapter was published in Applied Physics Letters (2015) and it presents the concept of quantum funnelling in 3-dimensions used in CQD solar cells. Darren C. J. Neo prepared the manuscript with the help of Dr Giles E. Eperon, Dr. Samuel D. Stranks, Prof. Henry J. Snaith, Prof. Hazel E. Assender and Prof. Andrew A. R. Watt. Dr Giles E. Eperon provided assistance in PL measurements. Ms Philippa C. J. Clark from the Photon Science Institute, University of Manchester, conducted all XPS measurements and analytical fitting.

6.1   Introduction

The first set of relatively efficient solar cells made with PbS/CdS CQDs was presented in chapter 5. However, there could be substantial room for improvement, especially in terms of fill factor, and if the device active layer could be made thicker it could capture more photons to boost J_{sc}. In this chapter, as a first step, the limitations of PbS/CdS core/shell CQDs is first examined. Then using the knowledge and understanding from additional characterisation techniques, novel concepts and device architectures were explored in an attempt to overcome or to circumvent the limitations. Ultimately, the aim is to see whether

device performance of PbS/CdS CQD solar cells could be further improved. This chapter has two main parts.

The first deals with the idea of quantum funnelling – a fast, non-radiative exciton transfer process between two proximal energy states with similar energy levels[145]. This charge transfer process does not rely on an electric field and is beneficial to move excitons rapidly before other competing processes like non-radiative recombination takes precedence[146]. The funnelling process is tailored so as to aid charge extraction even with a thicker device active layer.

The second part describes the use of a *p-i-n* device structure, a concept brought forth from amorphous silicon solar cell technology[147]. The low carrier density and intrinsic nature of PbS/CdS CQD could be overcome by applying layers with higher carrier densities (both *p* and *n*) at opposite ends, thereby creating an internal electric field capable of sweeping charges across the whole intrinsic layer. This therefore helps to mitigate the poorer transport properties of PbS/CdS CQD.

Before the new architectures are introduced, additional characterisation results carried out on PbS/CdS films and devices will be examined so as to confirm the intrinsic nature of PbS/CdS. All PbS/CdS CQD mentioned in this chapter are with 0.1 nm CdS shell thickness.

6.2 Limitations of PbS/CdS

6.2.1 Poor transport properties

The PbS/CdS devices presented in chapter 5 have low fill factors (*FF*) due to high series resistance, which in turn is a result of the extra energetic barrier imposed by the presence of the CdS shell. Therefore, the optimum device thickness is limited – a thicker device active layer would allow more light to be absorbed but a thicker active layer that has poor

transport properties which translate to a higher probability of charge recombination would contribute to less efficient charge extraction. This is especially so when a device is operating at high forward bias, which results in a narrow depletion width, making diffusion the dominant transport mechanism through the active layer. Since the diffusion length in the CQD film is short, there is always a limit as to how thick a device active layer could be if charges were to be extracted effectively.

A series of PbS/CdS – ZnO heterojunction devices, as presented in section 5.5.2, are fabricated with a range of different PbS/CdS layer thickness. 1.3 eV PbS/CdS (0.1 nm CdS) and the best combination of ligands, Br + EDT, are used consistently for all devices. With reference to *Figure 6-1*, the device performance is optimal at 150 nm of PbS/CdS and beyond that, it decreases due to the limited diffusion length of carriers in CQD film, resulting in more charge recombination.
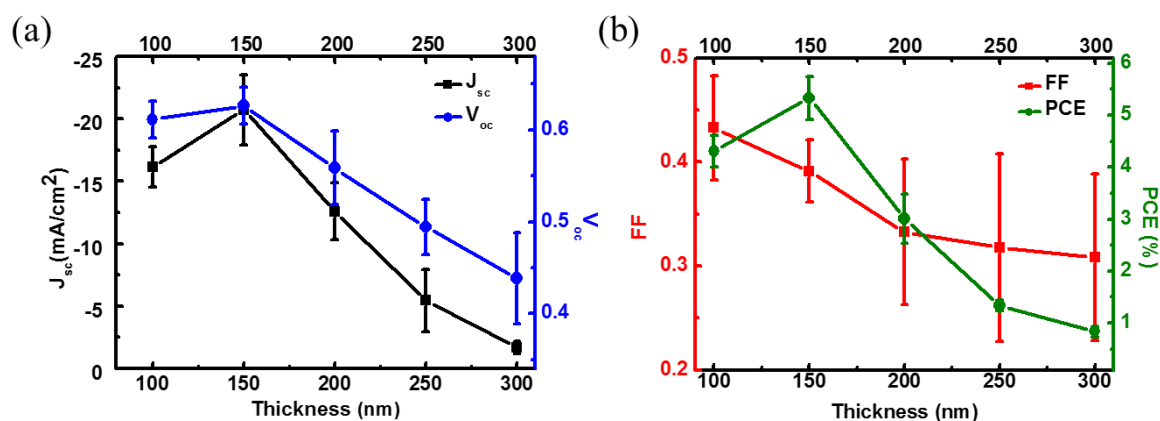
Figure 6-1. Device performance metric (a) J_{sc}, V_{oc}, (b) FF and PCE of PbS/CdS – ZnO heterojunction devices with different PbS/CdS layer thickness. 6 representative devices for each PbS/CdS layer thicknesses were evaluated and the ligand used is kept consistent as Br + EDT.

6.2.2 Intrinsic nature of PbS/CdS CQD film

Besides having low conductivity, another limitation of better surface passivation is the loss in effective carrier concentration. As seen in section 5.3.6, effective surface passivation is

manifested as an increase in photoluminescence (PL) yield with respect to the reference PbS quantum dot, which is indicative of a rise in radiative recombination and conversely a drop in number of non-radiative recombination centres[117]. These non-radiative recombination sites are usually attributed to the surface defect states and these defect states may also serve as donor/acceptor sites, which contribute to the total carrier density. It is known that mild oxidation of PbS introduces shallow trap states which increases the *p*-type character of the CQD[148]. With shell passivation, it could be surmised that such oxidation is less likely, thus resulting in a PbS/CdS film with a lower dopant concentration which is termed "quasi-intrinsic". XPS results affirm that PbS/CdS CQD films are less likely to be oxidised (See *Figure 6-2*). For a more definite measurement, capacitance-voltage (*C-V*) characterisation was performed to yield doping density, which relates to certain defect levels in PbS (due to oxidation[51]). *Figure 6-3* depicts the Mott-Schottky plots of PbS and PbS/CdS Schottky devices from the data gathered using *C-V* measurements. These were the same (best performing) Schottky devices as mentioned in section 5.3. Using the Mott-Schottky equation for Schottky junctions (see *Equation 6-1*),

$$\frac{1}{C^2} = \frac{2(V_{bi} - V)}{A^2 q \varepsilon \varepsilon_0 N_A}$$

Equation 6-1

where V_{bi} is the built-in potential, A is the active area (0.020 cm^2), q is the elementary charge, N_A is the doping density, ε is the dielectric constant of the active layer and ε_0 is the permittivity of free space, the doping density and built-in potentials can be found. The dielectric constant for PbS was estimated to be 20 by Tang *et al.,* using Maxwell-Garnett effective medium theory, and it is also assumed that the dielectric constant of PbS/CdS

with 0.1 nm CdS shell is similar[26]. The calculated results in *Figure 6-3* show that the doping

density in PbS/CdS CQD is an order of magnitude lower than PbS CQD.
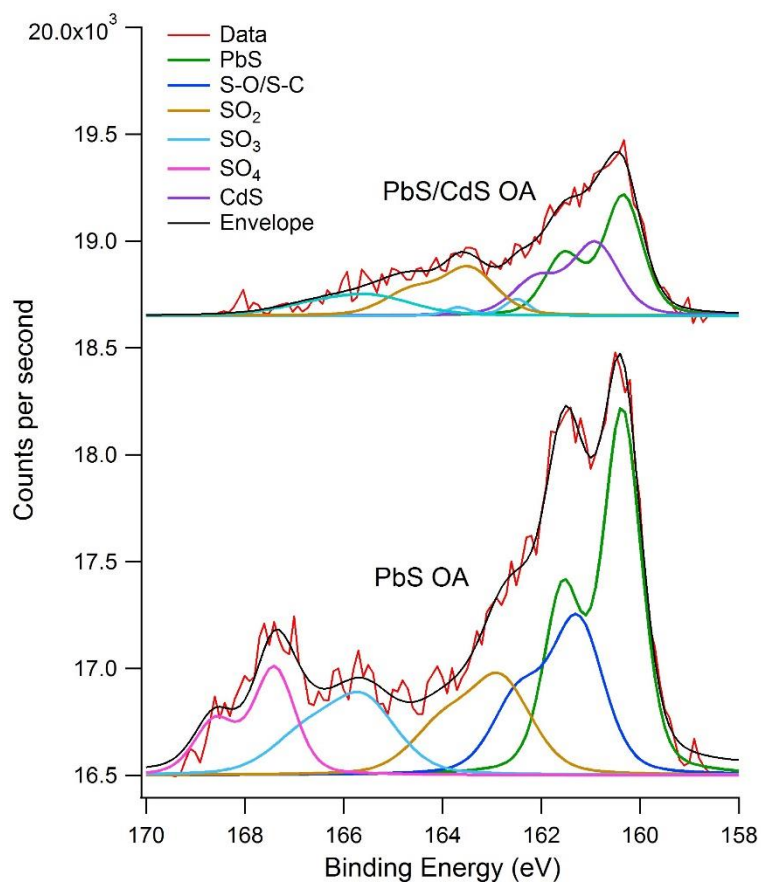
Figure 6-2. XPS data showing that the PbS/CdS CQD are more resistant to oxidation than PbS CQD. Samples of CQD film are stored in air-ambient, kept away from illumination, for a month before XPS measurement. XPS measurement and analysis is done by Ms Phillipa Clark.
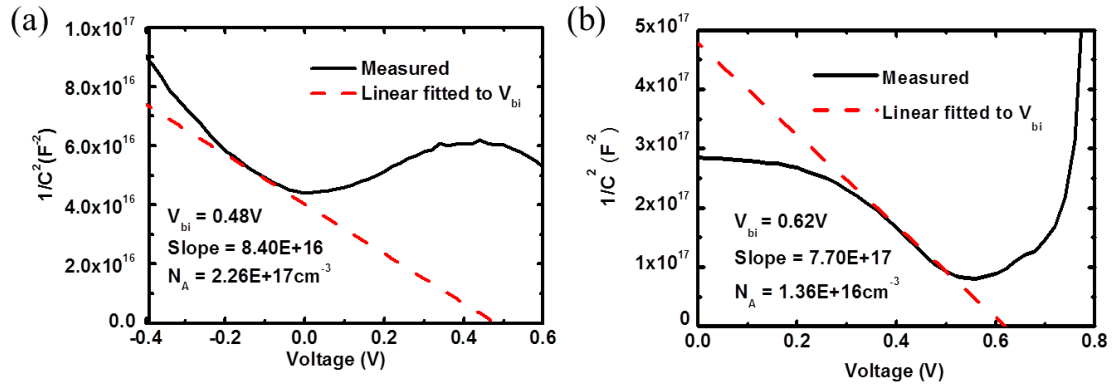
Figure 6-3. C-V measurements of (a) PbS and (b) PbS/CdS Schottky devices. The results show an order of magnitude lower dopant concentration in PbS/CdS CQD film as compared to PbS CQD film.

Now that the evidence of PbS/CdS film as being less conductive and having a lower carrier concentration is presented, two different ways of applying PbS/CdS as an active layer via unique device architecture will be discussed separately in section 6.3 and 6.4. The strategy for devices with thicker active layer is to exploit the intrinsic nature of PbS/CdS– a lower defect concentration reduces the probability of non-radiative recombination.

6.3   3D quantum funnelling

The concept of quantum funnelling is not new. Early works focused mainly on resonance energy transfer between CdSe quantum dots and fluorescence dye acceptor, which is bound to a biological molecule like a DNA or a protein for labelling or assay purposes[116,149,150]. One of the first attempts to couple different layers of CQD with different band gaps was by Klar *et al.* in 2005 who fabricated a cascaded band gap multilayer structure using light-emitting CQD and demonstrated efficient funnelling of excitons from large to small band gap[151]. A similar study was done by Xu *et al.* and showed that efficiency enhancement of charge transfer between small and large band gap PbS CQD could be achieved by using chemical cross-linking ligands[146]. Kramer *et al.* reported the first multi-band gap cascaded

CQD solar cell and showed that it outperformed a single band gap reference device with similar thickness. The improvement was attributed to better charge extraction as the depletion region was created by a graded band-gap structure which channels photogenerated charges into the depletion region. Efficiency enhancement was largely gained through improved fill factor[152]. Even more recently, Kim *et al.* fabricated a quantum funnel PbS CQD solar cell via a one-step centrifugal colloidal casting technique and showed an improvement in J_{sc} and *FF* over ungraded control devices. Using the concepts of funnelling and resonant energy transfer, similar strategies have been exploited in organic photovolatics (OPV) to increase absorption without compromising charge extraction[153].

Another strategy of OPV is to improve charge extraction through the formation of bulk heterojunctions where short diffusion lengths are mitigated by increasing the heterojunction's interfacial area[98]. Recently, Rath *et al.* demonstrated a CQD bulk heterojunction between *p*- type PbS CQD and *n*-type bismuth sulphide (Bi_2S_3)[97] CQD which consists of a blend of these two types of quantum dots sandwiched between a layer of pure PbS and Bi_2S_3. The performance of the bulk heterojunction device triumphed over a reference bilayer heterojunction device, and this was attributed to improved carrier lifetimes[97]. This provides the motivation to extend the quantum funnel process into 3 dimensions by blending different sized CQDs to increase interfacial area in which funnelling can occur. To date, blending different sized CQD to form a multi-band gap heterojunction device has largely been unexplored due to the smaller band gap CQDs acting as recombination centres[154] and interfacial trap states[155] which limit performance. Zhitomirsky *et al.* showed that beyond 10% inclusion of larger sized PbS in a population of smaller PbS, the device open-circuit voltage (V_{oc}) would drop significantly[41] and thus, blending PbS populations of different sizes beyond that blend ratio proved to be ineffective in the case of significant charge recombination.

To reduce non-radiative carrier recombination resulting from a bimodal CQD population, a core/shell PbS/CdS blend is used instead of PbS blend. Results from Chapter 5 show the effectiveness of CdS shell passivation on a PbS core, reducing surface related defects and charge recombination. Studies from Spiers *et al.*[156] and Lai *et al.*[157] independently showed, via spectroscopic techniques, that the presence of a CdS shell acts to passivate trap states and reduces trap density, thereby improving carrier lifetime, while Wheeler *et al.* were able to show the reduced trap densities in PbS/CdS core/shell quantum dots as compared to PbS cores[158], via a combination of ultra-fast absorption spectroscopy and photoluminescence. Therefore, it could be surmised that blends of CQD could still work if the charge transport after the quantum funnelling process is not heavily affected by charge recombination. This might be possible by using a blend of PbS/CdS CQD of different sizes where trap-related recombination processes are reduced due to effective shell passivation. In this section, the use of a blend of 1.2 eV and 1.4 eV core/shell PbS/CdS CQDs for the fabrication of a cascaded heterojunction photovoltaic device with an optimized thin film layer composition is described.

6.3.1   Properties of CQD blend films

The same concentration (40 mg/ml) of 1.2 eV and 1.4 eV PbS/CdS CQD solution is mixed in a 1:1 volume ratio. Devices were also made with the same procedure with each of 1.2 eV and 1.4 eV PbS CQD for reference. Under TEM (See *Figure 6-4*), it can be observed that the CQD blends are well percolated and do not form separate phases when cast as films. UV-Vis-NIR measurements (see *Figure 6-5*) confirm the presence of both components even after ligand exchange. A photoluminescence (PL) study is also performed on films formed from CQD blends to understand energy transfer[41,146]. The PL spectra of the core and core/shell blends show only the emission from the larger quantum dots with

peaks around 1140 nm and 1150 nm for Br + EDT ligand exchanged PbS/CdS and PbS CQD, respectively, as shown in *Figure 6-6*. This quenching effect of the larger band gap PL is not due to exciton dissociation but rather an energy transfer of the exciton from the larger to smaller band gap CQDs, because there is a rise in PL of the smaller band gap CQD, which is due to increased exciton population as a result from the transfer. The same phenomenon is also observed in other reports[145,146,159].

The PL intensity of the core/shell blend emission is much greater than that of the core-only blend (see *Figure 6-6*), implying that the shell reduces non-radiative recombination[117]. The PbS/CdS blends have a longer PL decay lifetime for both components, τ_1 and τ_2, (*Figure 6-7*), compared to PbS blends, which again serves as an indicator of reduced carrier recombination through non-radiative processes[118]. The rate of the PL process is a sum of both radiative and nonradiative recombination rates, and PL lifetime is inversely proportional to this rate, hence any decrease in non-radiative recombination component would result in an increased PL lifetime[160].

$$\boldsymbol{\tau} = \frac{1}{k_r + k_{nr}}$$ *Equation 6-2*

where τ is the PL lifetime and k_r and k_{nr} are the radiative and nonradiative recombination rates, respectively. Further, increased PL lifetime has been shown to correlate with better material quality and device performance in other material systems[161–164].
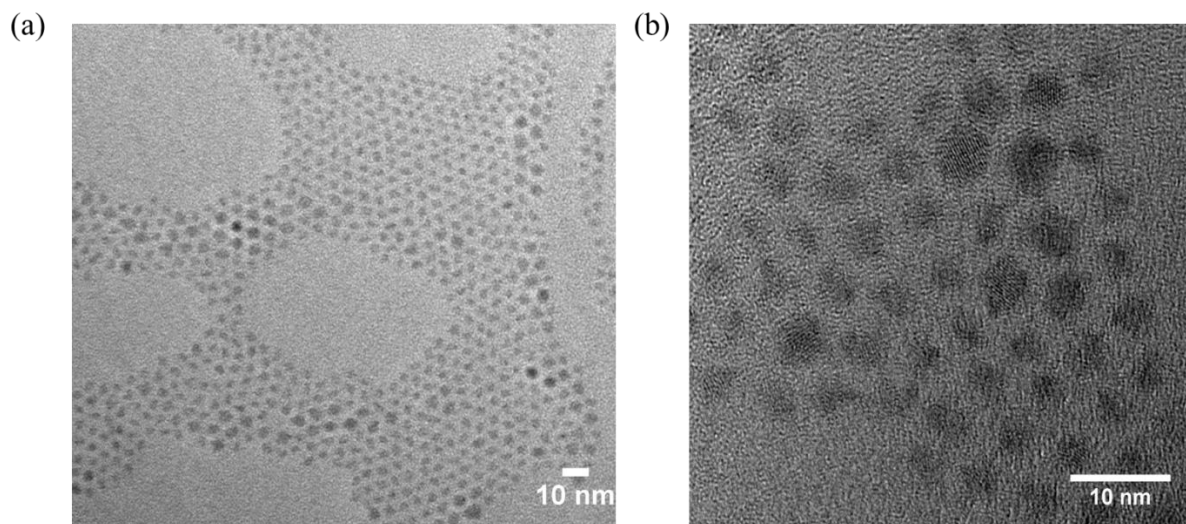
Figure 6-4. (a) Low magnification and (b) high magnification TEM images of 1.2 eV and 1.4 eV PbS/CdS CQD blend.
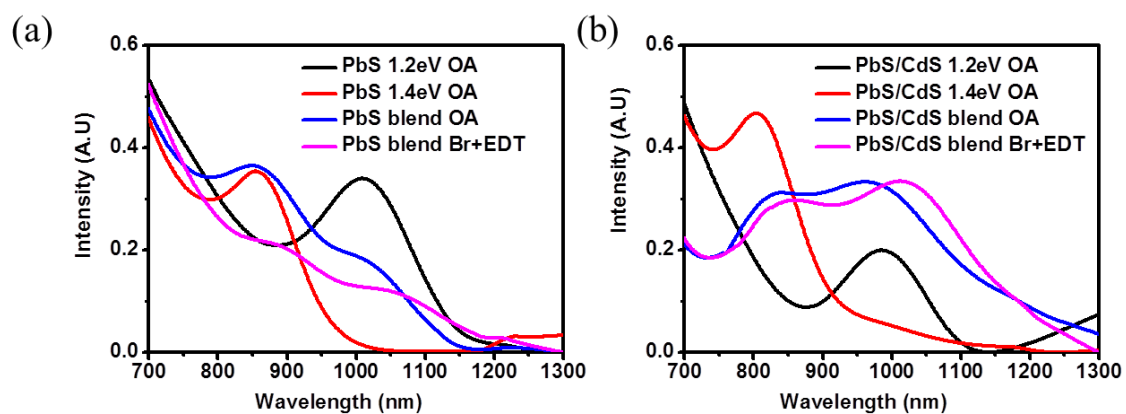
Figure 6-5. UV-Vis-NIR of (a) PbS blends and (b) PbS/CdS blends, comprising of 1.2 eV and 1.4 eV components.
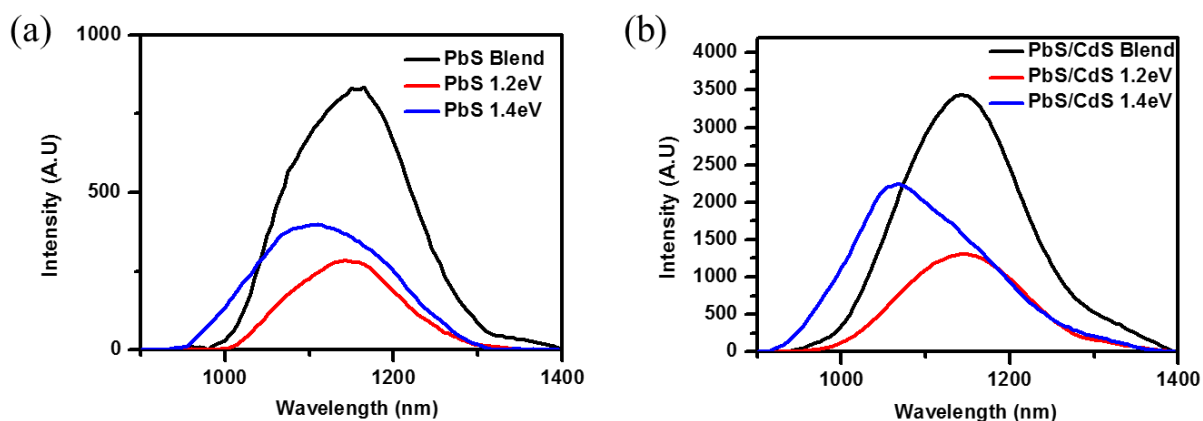
Figure 6-6. PL spectrum of (a) PbS blends and its components, and (b) PbS/CdS blends and its components. Both spectra indicate quantum funnelling of excitons from the 1.4 eV component to the 1.2 eV component as seen from the quenching of 1.4 eV peak. Graphs in (b) and (c) has been intentionally smoothed to make the peak position more obvious.
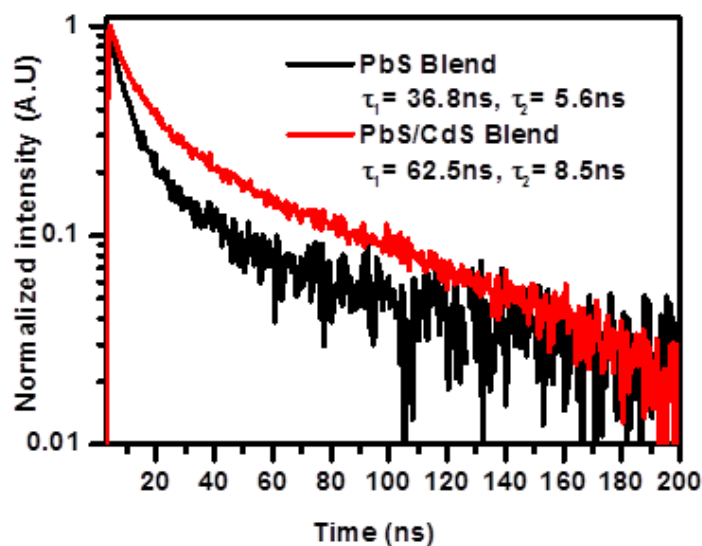
Figure 6-7. PL decay measurements showing a longer lifetime of PbS/CdS blend compared to PbS blend.

6.3.2   First trial of CQD blend devices

The current-voltage and external quantum efficiency of both blends forming heterojunctions with ZnO are shown in *Figure 6-8*. Devices have a similar structure to the heterojunction devices presented in section 5.5 and likewise the active layers are formed by a layer by layer spin coating process, where the ligand used here is fixed as Br + EDT (see Section 5.5.2). A 40 mg/ml CQD blend solution, spin cast at 2000 rpm and then subjected to ligand exchange, yields a film thickness of 25 ± 3 nm as measured using a profiliometer. A total of 8 layers of CQD blends were deposited and then finally topped with ZnO solution spin cast at 2000 rpm. The device structure is also illustrated in the insert of *Figure 6-8(a)*. The power conversion efficiency of both devices is poor, reaching 2.4 % for the core blend and 2.1 % for the core/shell blend. For the purpose of this study, an active layer thickness of about 200 nm was fixed and devices were intentionally made much thicker than the optimal (of 150 nm) afforded by the heterojunction so as to demonstrate that quantum funnelling does occur to alleviate the problems of a limited depletion width and contributes to charge extraction. Photogenerated charges outside of the depletion width may be funnelled into it, thereby increasing the probability that they would be extracted. The external quantum efficiency (EQE) of the PbS/CdS device is worse than the PbS-only blend due to the lower J_{sc}. However, the PbS/CdS device has a more distinct excitonic band edge which could indicate improved preservation of quantum confinement. Photogenerated charges in PbS/CdS layer experience higher resistance[157] and lower mobility and with a 200 nm thick active layer, this impedes charge extraction, resulting in lower quantum efficiencies. Best device performances with a 200 nm thick active layer comprising individual component CQD and CQD blends are illustrated in *Figure 6-9*. At this juncture, it might seem that blending CQD might not be beneficial and may even deteriorate device performance. Nevertheless, an investigation was done on the open-

circuit voltage and reverse saturation current of devices to examine the extent of carrier recombination (which is affected by trap densities).
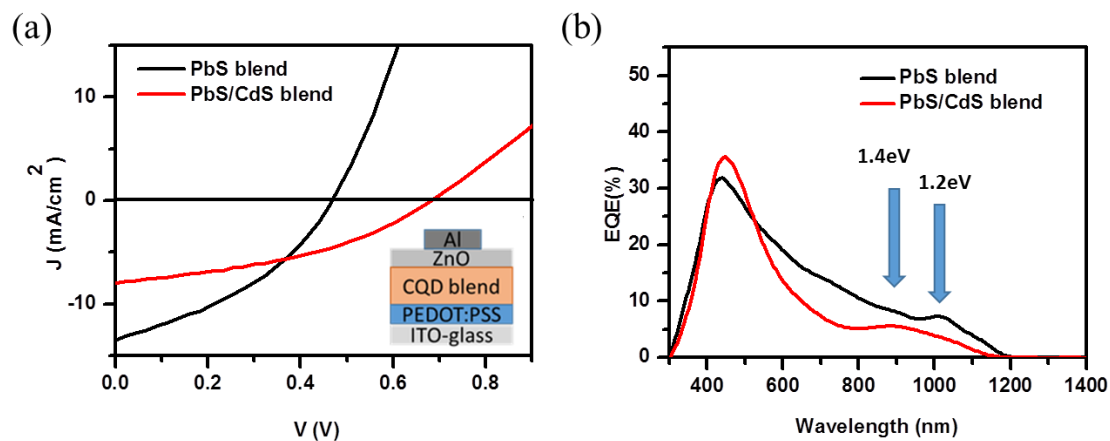
Figure 6-8. (a) J-V performance curve of blend devices which have a 200 nm thick layer of CQD blend films, topped with a ZnO layer. Insert depicts the device structure (b) External quantum efficiency characterization of the devices described in (a). Arrows point to the first excitonic peak energy of 1.2 eV and 1.4 eV PbS and PbS/CdS CQD.
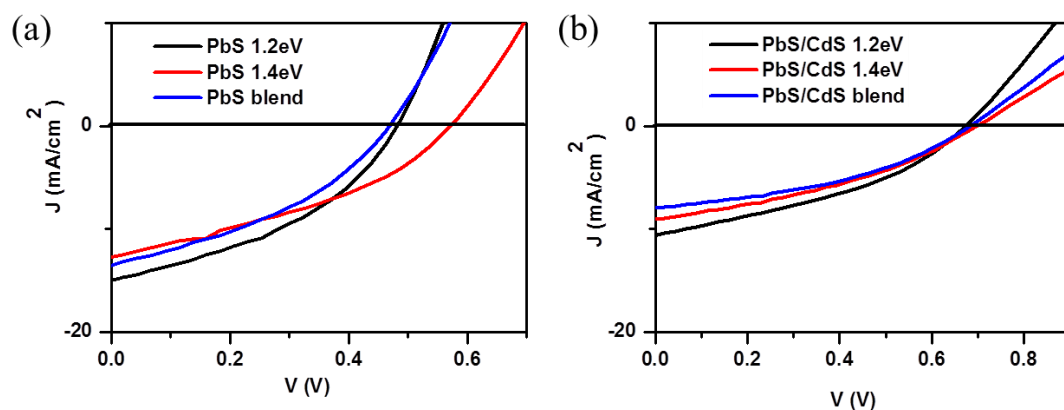
Figure 6-9. J-V characterization of the best devices (with 200 nm thick active layer) of (a) PbS blends and their components, (b) PbS/CdS blends and their components.
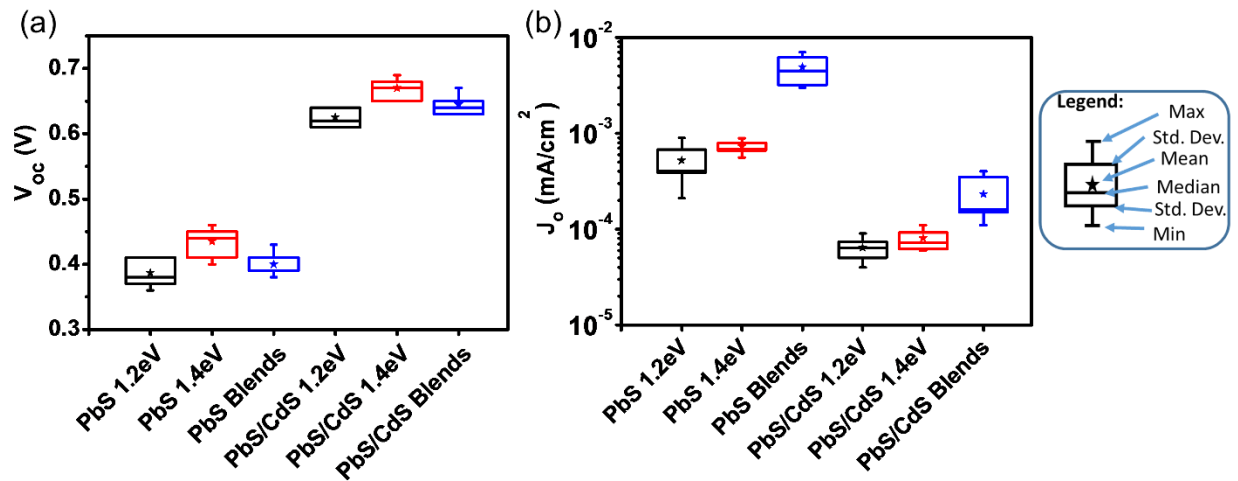
Figure 6-10. (a) Open-circuit voltage and (b) reverse saturation current of devices fabricated with n-type ZnO layer on top of 200 nm PbS and PbS/CdS blends respectively. Each sample statistic is built upon 18 devices, with 3 devices on each substrate.

Figure 6-10 compares the open circuit voltage (V_{oc}) and reverse saturation current (J_o) for single CQD materials and blends with and without shells. It is hypothesised that quantum funnelling is efficient from large to small band gap CQDs but the subsequent extraction of charges is dependent on the electric field created by the ZnO heterojunction or charge diffusion to an electrode. The success of charge extraction is reliant on charge transport efficiency which is in turn dependent on carrier recombination rates. *Figure 6-10(b)* shows that reverse saturation current, which is a good metric for recombination, is much lower in the PbS/CdS blend compared to the PbS blends, and that for both materials the reverse saturation current is greater in the case of the blend, compared to the corresponding single band-gap materials. Charge transport is impeded by trap states which can be thought of as 1) crystallographic defects on the surface of the CQD and 2) in a blend the small band gap CQD acts as a trap for the large band gap CQD, creating energy disorder[41]. Thus, devices comprising of blends, as compared to single-component systems, show a higher trap density (and higher recombination current). However, if a comparison is made solely on

the devices comprising of CQD blends, PbS/CdS core/shell blends have lower recombination current compared to PbS blends as CdS presents itself as an epitaxial shell of larger band gap semiconductor material around the PbS cores, mitigating surface trap states. This idea is illustrated in *Figure 6-11*.

Therefore, quantum funnelling is happening in the blends and recombination is supressed in PbS/CdS blends as compared to PbS blends but PbS/CdS blend devices are not performing well simply because funnelled charges (from 1.4 eV to 1.2 eV CQD) still have to make their way to the electrode to be extracted and 200 nm is too thick for most charges to be transported to the electrode. Also, resonance energy transfer processes takes place at short range distances (~ 10nm) and the contribution towards extra charge extraction might not be significant for the case of a 200 nm thick active layer. As discussed above, the trap density of CQD blend films is higher than single component films and thus, there is need to combine the benefit of quantum funnelling from PbS/CdS blend and necessity to extract funnelled charges successfully.
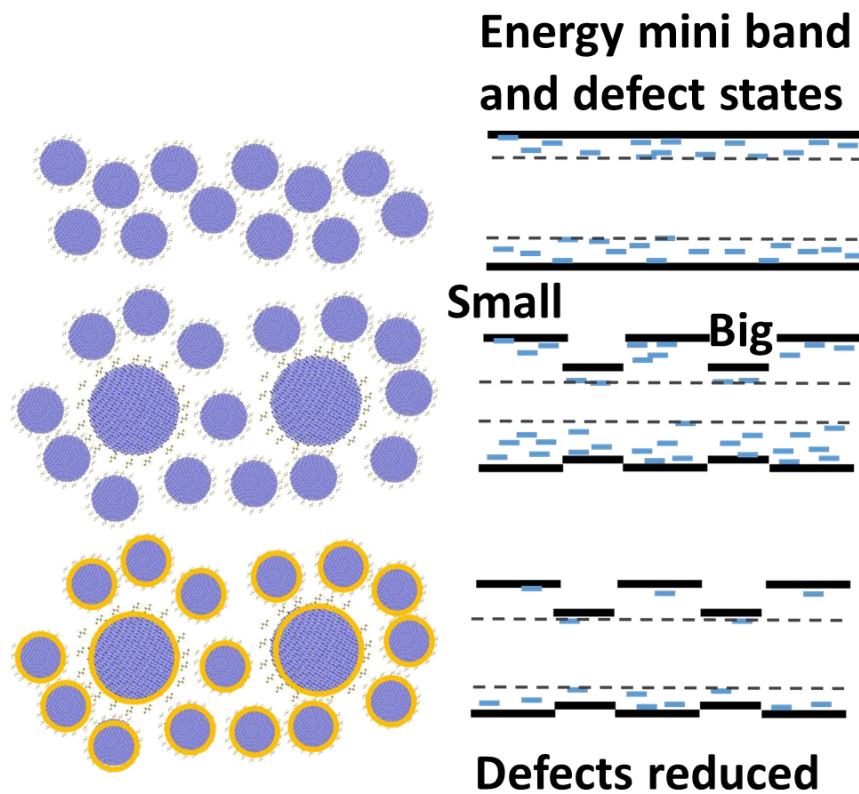
Figure 6-11. An illustration of mini band formation of pure phase PbS, the bimodal PbS blend and the bimodal PbS/CdS blend. The CdS shell passivates surface states that form trap level states as compared to pure phase PbS such that charges funnelled into the big (smaller band gap) quantum dots would be less likely to recombine.
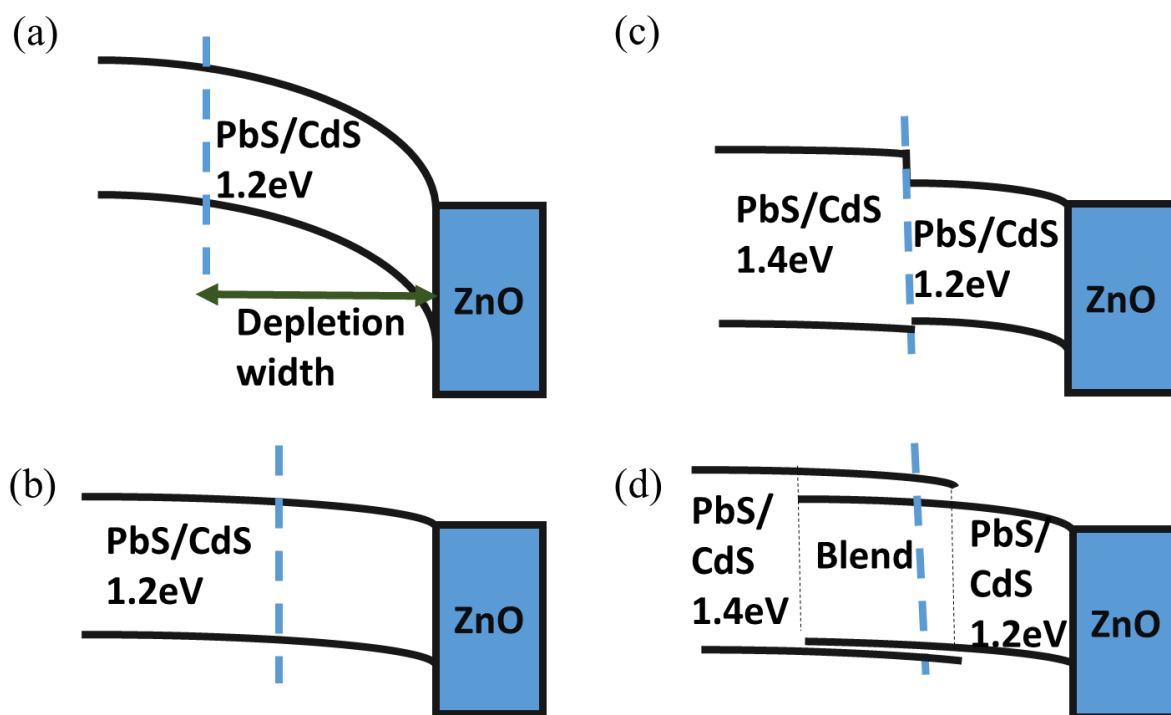
Figure 6-12. Band bending of heterostructure device (a) at short circuit current and (b) at forward bias, at maximum power point. Band bending, at maximum power point, of (c) a bilayer device and (d) a blend device in "sandwich" configuration.

6.3.3   CQD blends in a sandwich structure

The next challenge is to further improve the core/shell blend device performance by modifying the device architecture. CQD solar cells rely heavily on the depletion zone to separate charges by drift because the innate disorder in nanocrystalline systems results in short carrier diffusion lengths[165]. Therefore, at high forward bias (for example at the maximum power point), the depletion width is very much reduced and diffusive transport dominates, resulting in fewer charges being successfully extracted at the electrodes (refer to *Figure 6-12(a) and (b)*). This is reflected in the low fill factors observed for CQD solar

cells[137]. A bilayer structure (*Figure 6-12(c)*) would fare better than the usual heterostructure due to a potential difference that serves as an electron blocking layer and also some amount of charge funnelling at the interfacial region between the 1.2 eV and 1.4 eV layers. To maximize the effect of funnelling, a blend layer could be incorporated to improve the interfacial area so that charges can be cascaded very quickly from any 1.4 eV CQD to a neighbouring 1.2 eV CQD, even without the presence of band bending or internal electric field from the depletion width (*Figure 6-12(d)*). Improving charge transport at near flatband potential situations would help to improve device fill factor.

Assuming that the 1.2 eV CQD is well percolated throughout the blend as shown on TEM samples (see *Figure 6-4*), funnelled charges could follow a continuous pathway towards their respective electrodes. However, the charge transport of charges after the process of funnelling is problematic. Based on the energy levels measured and calculated by Hyun *et al.*[33], energy barriers will be formed between small band-gap CQD in the vicinity of large band-gap CQD, both at the HOMO and LUMO energy level states (*Figure 6-11*). These could be overcome by the internal electric field provided by the band-bending effect of the heterojunction but the depletion width is limited, which calls for the need to optimize the thickness of the blend region. To harness the advantage of the funnelling mechanism and not to be restricted by charge transport issues, layers of pure 1.2 eV and 1.4 eV PbS/CdS are used to act as electron collecting and electron blocking layers respectively, in an effort to also reduce the blend layer thickness (*Figure 6-12(d)*). By keeping the entire CQD layer thickness constant, the composition of layers was varied from a completely blended film to a blend layer being sandwiched between 1.2 eV and 1.4 eV CQD films and finally to a 1.2 eV and 1.4 eV bilayer, as illustrated in *Figure 6-13(a)*. It was observed that the sandwich configurations gave better fill factors and with that, the optimum device (*Figure 6-13*) gave an efficiency of 4.62 %, almost a threefold improvement over devices made of

only 1.2 eV or 1.4 eV PbS/CdS CQD of the same thickness. Therefore, even though an active layer consisting of PbS/CdS CQD blends alone performs poorly, using the blend region as part of a sandwich structure allows both a reduction in recombination and a thicker active layer thickness with less loss in photocurrent. The device performances of various device architectures are summarized in *Table 6-1*.
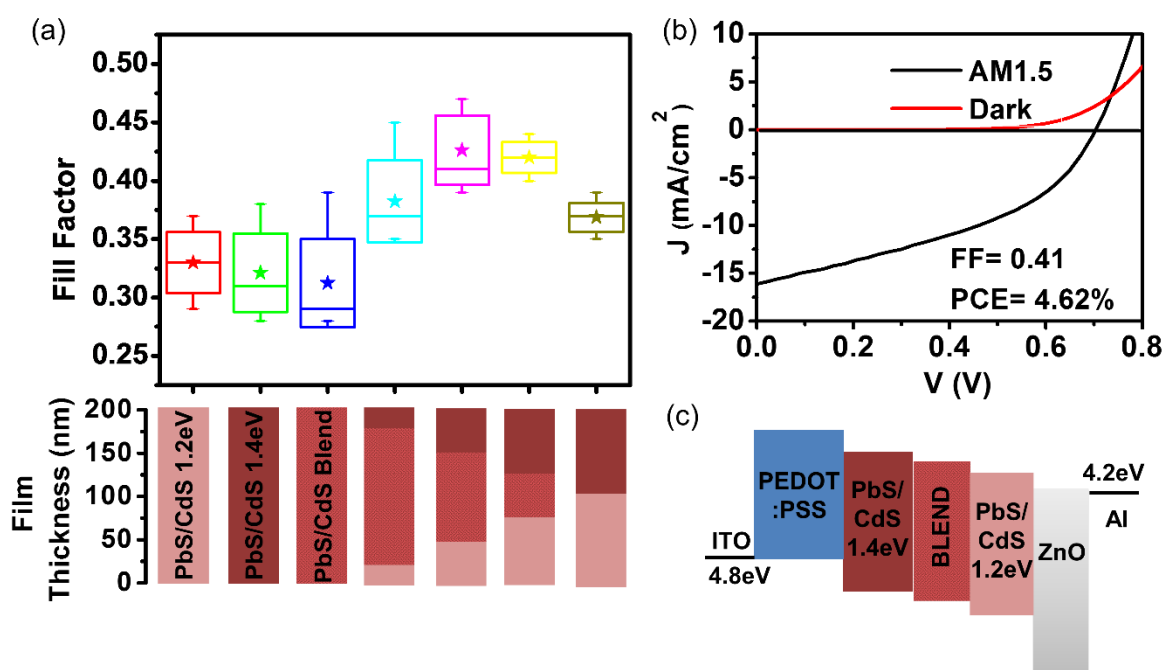
Figure 6-13. (a) Fill factor recorded for devices fabricated with n-type ZnO layer on top of PbS/CdS CQDs and blends with various architectures. The total thickness of the CQD film was fixed at 200 nm. Colours correspond to the components depicted in part (c) Best fill factors were achieved with a 100nm blend sandwiched between 1.2 eV and 1.4 eV PbS/CdS layers, each 50nm thick. (b) Device performance of the champion cell made with this architecture. (c) Band alignment diagram of the champion device.

Table 6-1. Data statistics for heterojunction, full blend, sandwich configuration and bilayer structures. Data is averaged over 36 devices across 12 separate substrates, with standard deviation reported. Refer to Figure 6-13(a) for the schematics of the individual structures. 1 blend 6L 1 refers to 25 nm of 1.2 eV PbS/CdS layer, 150 nm of blend layer and 25 nm of 1.4 eV PbS/CdS layer, etc.

Structures	PbS/CdS 1.2eV	PbS/CdS 1.4eV	PbS/CdS blend	1 blend 6L 1	2 blend 4L 2	3 blend 2L 3	PbS/CdS Bilayer
J_{sc} *(mA/cm^{-2})*	8.9 ± 0.8	5.9 ± 1.8	6.8 ± 0.7	12.5 ± 2	14.3 ± 1.3	13.5 ± 1.2	11.8 ± 1.9
V_{oc} *(V)*	0.63 ± 0.02	0.68 ± 0.02	0.65 ± 0.02	0.66 ± 0.01	0.68 ± 0.02	0.68 ± 0.01	0.64 ± 0.02
FF	0.33 ± 0.02	0.32 ± 0.03	0.31 ± 0.04	0.38 ± 0.04	0.43 ± 0.03	0.42 ± 0.01	0.37 ± 0.01
PCE (%)	1.9 ± 0.4	1.3 ± 0.6	1.4 ± 0.3	3.1 ± 0.3	4.1 ± 0.3	3.9 ± 0.5	2.8 ± 0.5

In all, a multi-band gap quantum cascade photovoltaic device has been demonstrated using a blend of PbS/CdS core/shell CQD with 1.2 eV and 1.4 eV band gap. The inclusion of a semiconductor shell around the core allows the formation of blended multi gap structures with subtle device performance improvements associated with a reduction in non-radiative recombination. The idea of charge funnelling from large to small band gap CQD was hypothesised to alleviate the problem of short carrier diffusion length. To test this hypothesis, a blended active layer is included as part of a sandwich structure of low gap-blend-wide gap CQDs in a bid to improve device performances. The quantum funnel effect acts in tandem with the depletion width to extract charges, with the aid of a bulk heterojunction-like sandwich structure. Even with an active layer thickness of 200 nm, power conversion of up to 4.6 % was achieved primarily by improvements to fill factor. Although PbS/CdS device performance was unable to be enhanced beyond what was established in chapter 5, this section illustrates a novel concept which minimizes deterioration in device performance with thicker layers. Quantum funnelling provides an alternative pathway to extract charges which are otherwise lost by recombination due to the limited carrier diffusion length, therefore preserving V_{oc} and FF. However, the performance of the devices with a PbS/CdS blend exhibits limited current extraction due to its fundamental intrinsic character as compared to thinner non-blend devices (150 nm, as described in chapter 5). As such, the drop in overall J_{sc} due to limited charge extraction outweighed the benefit of the funnelling effect. In the next section, a different device architecture will be presented.

6.4   *p-i-n* devices

It was shown in section 6.2.1 that thicker PbS/CdS layers hamper device performance, in particular, the fill factor is low and series resistance is higher, consistent with the studies of Kim *et al.*[167]. Although a low defect concentration is favoured, the direct consequence is lower carrier concentration and lower conductivity. It is likely that this is responsible for the deteriorated performance of the device when the active layer (PbS/CdS) is made thicker. Another technique to afford a thicker PbS/CdS layer with a wide region promoting drift of charges is adopting a *p-i-n* device structure.

The notion of a *p-i-n* junction is common in amorphous silicon photovolatics and has only recently been implemented in colloidal quantum dot solar cells by Ko *et al.*[168]. Copper (I) iodide and ZnO were used as the *p*-type and *n*-type material respectively, sandwiching a lead selenide CQD layer in between them. Ko showed an improvement of device performance as compared to heterojunction devices and suggested that the *p-i-n* architecture helps to extend the depletion width, aiding current extraction. Therefore, photogenerated charges that are created further away from the ZnO/CQD junction can still be swept away by the extended potential gradient created by this *p-i-n* architecture, reducing recombination that lowers both V_{oc} and fill factor.

In this section, devices made using the *p-i-n* architecture will be explored. 1.3 eV PbS/CdS and 1.3 eV PbS CQD are used in this section. Till now, ZnO has always been deposited as the top layer, just before the metal electrode and this is termed an "inverted structure". Here, the other variant of switching the *n*-type material from top to bottom is also presented, which is termed an "upright structure". The proposition for the "upright structure" and the difference in device performance will also be discussed in this section.

6.4.1 Inverted structure

From the *C-V* results, it can be concluded that PbS CQD film is more *p*-type (higher doping/ acceptor concentration) than the PbS/CdS CQD film. Therefore, having a more *p*-type PbS and a *n*-type ZnO provides a larger Fermi energy difference than PbS/CdS- ZnO and therefore creates a wider potential gradient or a larger depletion width for the same extent of band bending. Therefore, sandwiching the intrinsic PbS/CdS layer between ZnO and PbS would overcome its disadvantage of lower conductivity and at the same time benefit from lesser non-radiative recombination due to lower defect concentration (see *Figure 6-14*).

6.4.1.1 Device fabrication

First, control heterojunction devices were made using 40 mg/ml PbS/CdS solution. Each layer was formed by spin coating the CQD solution at 2000 rpm and then performing a Br + EDT ligand exchange, giving a thickness of 25 ± 3 nm. The control device consists of 8 layers of PbS/CdS (which is about 200 nm) on a PEDOT:PSS coated ITO substrate and then topped with ZnO. Then the inverted *p-i-n* devices were made. Keeping the total film thickness similar, the first bottom two layers formed by spin coating 40 mg/ml PbS CQD solution, exchanged with EDT ligands only. Then the next 6 layers is comprised of PbS/CdS, deposited using the same spin coating procedure as the control and Br + EDT as the ligand, before the ZnO layer is deposited. To take the *p-i-n* concept even further, another batch of devices were fabricated with the bottom PbS film annealed at 90 °C for 3 minutes in air after EDT exchange and before PbS/CdS and ZnO deposition. The mild oxidation of PbS has been shown to improve *p*-type characteristics[169]. This should result in a greater difference in doping concentration between the *p* and *i* layers, changing the structure from *p-i-n to p$^+$-i-n,* where p+ indicates a higher p-type doping level. This gives

enhanced band bending at the interface and thus further aiding charge extraction. Device structures and band banding concepts are illustrated in *Figure 6-14.*
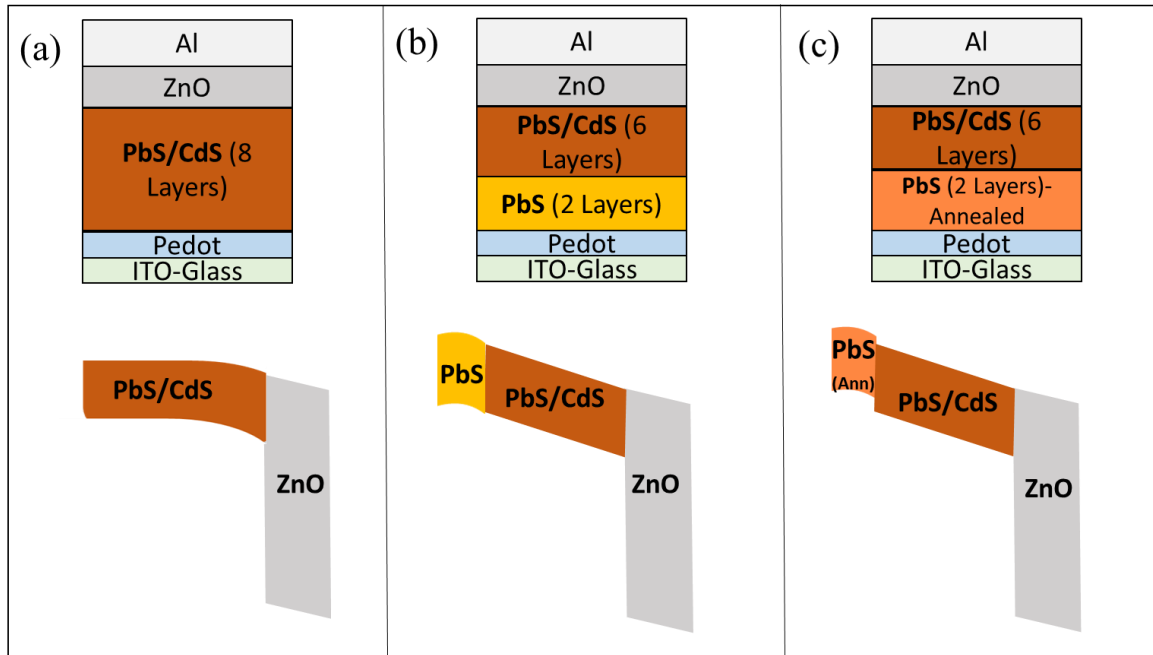
Figure 6-14. Diagram illustrating device structures, (a) PbS/CdS-ZnO heterojunction, (b) PbS-PbS/CdS-ZnO p-i-n structure, (c) PbS(ann)-PbS/CdS-ZnO p⁺-i-n structure and their proposed band bending due to equilibrating Fermi level.

6.4.1.2 Device performance

J-V characterisation of best performing devices of each architecture is presented in *Figure 6-15* and device performance statistics are summarised in *Table 6-2*. It is obvious the 200 nm thick PbS/CdS heterojunction device suffers from low fill factor and limited photocurrent due to the intrinsic and highly resistive nature of the PbS/CdS film. Therefore, replacing 50nm of it with PbS first reduces the resistance of the device by making the PbS/CdS segment thinner (as evident on the slope of the graph near V_{oc}). Then the insertion of PbS further increases internal electric field due to band alignment, therefore improving drift transport. Further evidence of reduced recombination with the introduction of a graded structure can be seen in the dark *J-V* curve (*Figure 6-15(b)*), in which the y-intercept gives

the reverse saturation current. Since reverse saturation current increases with increased carrier recombination, the obtained results are indicative of a reduced carrier recombination with increased doping gradient (transiting from *i-n* to *p-i-n* to *p+-i-n*) possibly due to enhanced band bending and thus the extra driving force to separate and extract the charges. *p+-i-n* would be even better at reducing recombination as the annealed-PbS is potentially poised to block electrons and to allow the transport of holes. This charge selectivity would further reduce charge recombination[170]. These results justify the dependence of relatively thick devices on the depletion region or potential gradient due to band bending to supplement the short carrier diffusion length typical of quantum dot film system[170].
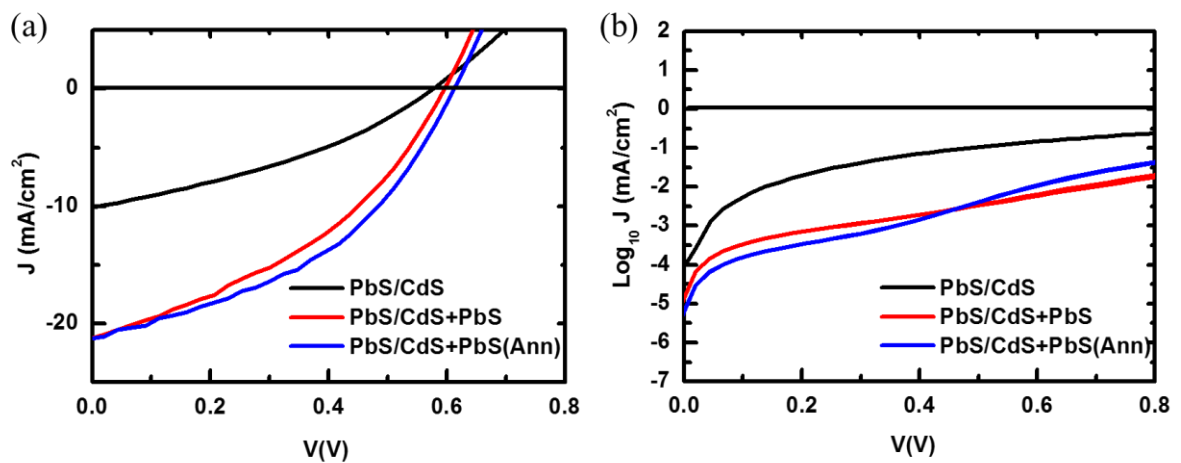
Figure 6-15. (a) J-V curves of the best performing device of PbS/CdS-ZnO heterojunction, PbS-PbS/CdS-ZnO p-i-n structure and PbS(ann)-PbS/CdS-ZnO p+-i-n structure compared. (b) Dark current of the sane devices in (a).

Table 6-2. Device performance statistics for PbS/CdS-ZnO heterojunction, PbS-PbS/CdS-ZnO p-i-n structure and PbS(ann)-PbS/CdS-ZnO p+-i-n structure. All devices have roughly 200nm of active layer thickness.

Structure	J_{sc} (mA/cm^2)	V_{oc} (V)	FF	PCE (%)
PbS/CdS	7.9 ± 2.0 (10.0)	0.60 ± 0.02 (0.59)	0.33 ± 0.03 (0.34)	1.56 ± 0.36 (2.01)
PbS/CdS- PbS	19.9 ± 2.4 (21.9)	0.60 ± 0.03 (0.61)	0.38 ± 0.02 (0.38)	4.54 ± 0.48 (5.08)
PbS/CdS- PbS (Ann)	19.1 ± 4.3 (22.1)	0.61 ± 0.03 (0.62)	0.43 ± 0.03 (0.42)	5.01 ± 0.74 (5.75)
Results are averaged with standard deviation across 12 samples on 4 different substrates. The J_{sc}, V_{oc}, FF and PCE of champion devices are quoted in brackets.				

Despite the effort made to improve device performance with thicker device active layer thickness, the efficiencies are still lower than those recorded for the 150 nm active layer. If the *p-i-n* strategy is applied to devices with 150 nm thick active layer, there could be minor or no improvement at all. The stronger band bending would improve current extraction capability and the *FF* of devices might be better than those of 200 nm thick active layer but a thinner absorber layer would set an upper limit to how much photogenerated charges is produced. Yet another strategy is to place the PbS/ n-type material junction closer to the side of illumination. This will be discussed in the following section.

6.4.2   Upright device

There are 3 main reasons to place the charge separating junction closer to the side of illumination:

(i)   Most of the incident light is being absorbed at the front of the device,
        especially the higher energy wavelengths. If the charge separating junction is
        at the side of illumination, most of the photogenerated carriers would be
        within the depletion width of the junction and hence they would have a higher
        extraction efficacy.

(ii)   Wide band gap semiconductors like ZnO and TiO_2 rely on UV absorption for photodoping, which increases n-type carrier density, conductivity and also the depth of the depletion width[171]. When they are used to form a rear junction, if the device active layer is thick, most of the UV photons would be absorbed before reaching the n-type material.

(iii)   It has been shown that the upright structure offers better device stability due to the presence of the wide band gap semiconductor that helps to absorb much of the UV light component of sunlight[172]. UV rays, in the presence of air, has been shown to accelerate the degradation of colloidal quantum dots[173], so the wide band gap semiconductor could afford some protection.

Reasons (i) and (ii) mean that a thicker active layer could be accommodated and with the added benefits of a *p-i-n* structure, an improvement beyond 6 % efficient devices should be possible. In this section, a bottom layer of mesoporous TiO_2 was used instead of a ZnO layer because at the time when this work was conducted, mesoporous TiO_2 as a bottom layer was used for the best depleted heterojunction reported[60]. Mesoporous TiO_2 was thought to be able to increase the surface area of contact between itself and the quantum dots and therefore decreasing the overall distance need for charges to reach the TiO_2/CQD junction. In this case, the ligand 3-mercaptopropionic acid (MPA) was used in place of EDT for both PbS and PbS/CdS CQD as a cross-linking ligand as it is known to give a higher mobility-lifetime product and a comparatively lower trap density due to its different functional groups being able to passivate more diverse types of surface defects[174].

6.4.2.1 Device fabrication

FTO substrates were used in this case and they are cleaned, dried and O_2 plasma treated as described in section 4.4.1.3. A compact layer of TiO_2 was first formed on FTO by spin coating TiO_2 precursor sol-gel (preparation is discussed in section 4.2.4) at 2000 rpm for

45 seconds. Next, a small portion of TiO$_2$ sol-gel on the corners of the FTO was cleared away to allow contact during testing by using a cotton tip. The coated substrates were then sintered in air at 450°C for 30 minutes. After the substrates have cooled down, a mesoporous TiO$_2$ layer was deposited by spin coating TiO$_2$ paste (Dyesol 18NR-T) diluted in anhydrous ethanol at 1:4 by weight at 2000 rpm for 45 seconds. Similarly, contacts were cleared and substrates were sintered in air at 450 °C for another 30minutes. The total thickness of compact and mesoporous TiO$_2$ after sintering is 445 ± 21 nm. After the preparation of the *n*-type bottom layer, the PbS and PbS/CdS control heterojunction devices were made using 40 mg/ml of PbS and PbS/CdS solution respectively. Each layer was formed by spin coating the CQD solution at 2000 rpm and then performing a Br + MPA ligand exchange. The control device consists of 12 layers of CQD deposited on the mesoporous TiO$_2$, giving a total thickness of 710 ± 27 nm (and so the total CQD film thickness is about 250 nm). Each layer of CQD deposition after ligand exchange on a smooth substrate should give a thickness of about 25 nm and 12 layers would total to about 300 nm. However, it can be said that there is some penetration of PbS/CdS CQD into the TiO$_2$ mesoporous layer which therefore gives a smaller than expected total film thickness. Then for *p-i-n* devices, keeping the total film thickness similar, the first 10 layers are formed by spin coating 40 mg/ml PbS/CdS CQD solution, exchanged with Br + MPA ligands and the next 2 layers are comprised of films formed with spin coated 40 mg/ml PbS CQD, exchanged with MPA ligand. *Figure 6-16* shows the device structures described in this section and their respective proposed band alignment.
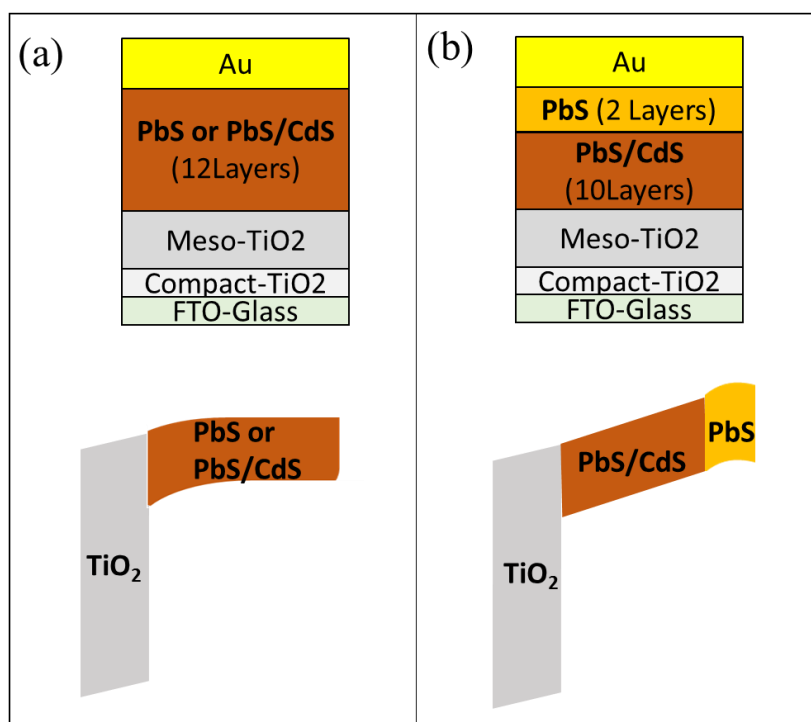
Figure 6-16. Diagram illustrating device structures, (a) PbS-TiO$_2$ or PbS/CdS-TiO$_2$ heterojunction (b) PbS-PbS/CdS-TiO$_2$ p-i-n structure and their proposed band alignment due to the equilibration of Fermi level.

6.4.2.2 Device performance

With reference to the results in *Figure 6-17(a)* and *Table 6-3*, devices with PbS as the only active material form our baseline control device and the best control device fared within 10 % range of previously published results (the best reported for 1.3 eV PbS was 5.1 % PCE). However, with the same total device thickness, the PbS/CdS heterojunction device performed poorly, even with improved V_{oc} compared to the PbS reference device. The low fill factors and the high series resistance shows that the 250 nm thick PbS/CdS layer limits the device performance because of its poorer charge transport properties. This is mitigated by replacing the top two layers of PbS/CdS with PbS exchanged with MPA ligands to form a *p-i-n* structure. In doing so, the performance of the device improved dramatically, due to the concomitant improvement of fill factor, V_{oc} and J_{sc}. The *p*-type doped PbS creates a

more pronounced difference in Fermi level as compared to TiO_2 and forms part of the *p-i-n* structure, providing a larger internal electric field to transport charges through the intrinsic PbS/CdS region via drift transport. The PbS/CdS heterojunction device shows lower V_{oc} values than the *p-i-n* device primarily because more charges recombine before extraction. Comparing the EQE of the PbS/CdS heterojunction device and the *p-i-n* device, the latter gave a higher EQE response in almost all regions of wavelength, confirming the presence of a stronger internal electric field across the majority of the active material. Therefore, the results obtained are consistent with the idea that forming a *p-i-n* device architecture would help alleviate the problem of PbS/CdS films having poorer charge transport properties. From this, the best device obtained gave an efficiency of 6.4%, which represents a 40% improvement over baseline PbS heterojunction devices and shows a relatively high V_{oc} stemming from the improved passivation of the PbS/CdS film.
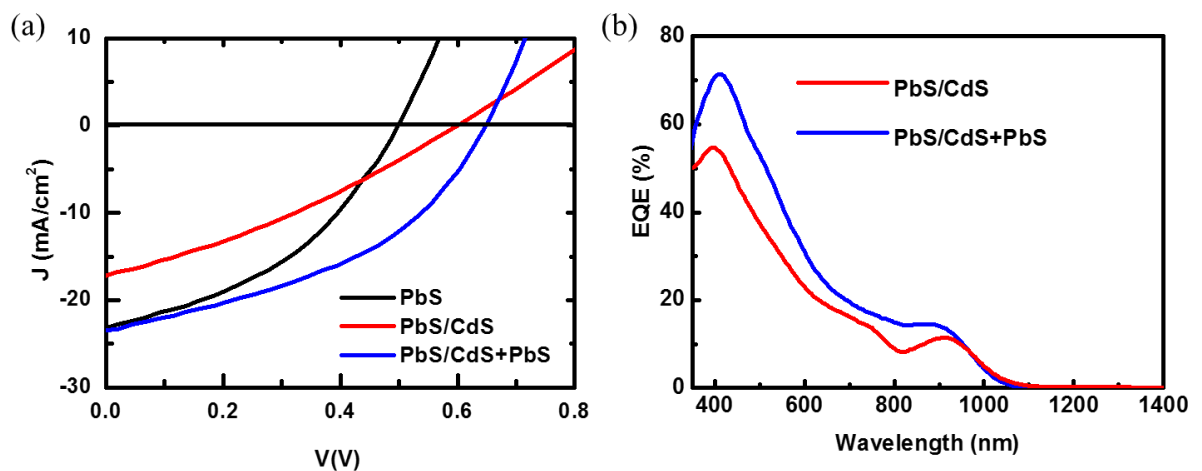
Figure 6-17. (a) J-V curves of the best performing device of the PbS-TiO₂, PbS/CdS-TiO₂ heterojunction and PbS-PbS/CdS-TiO₂ p-i-n structure compared. (b) EQE of the PbS/CdS-TiO₂ heterojunction and PbS-PbS/CdS-TiO₂ p-i-n structure. All devices have roughly the same overall thickness. Refer to Table 6-3 for device performance statistics.

Table 6-3. Device performance statistics for the heterojunctions and p-i-n structure.

Structure	J_{sc} (mA/cm^2)	V_{oc} (V)	FF	PCE (%)
TiO$_2$-PbS	20.9 ± 3.5 (23.5)	0.52 ± 0.04 (0.50)	0.36 ± 0.06 (0.39)	3.91 ± 0.72 (4.58)
TiO$_2$-PbS/CdS	15.9 ± 2.4 (17.4)	0.55 ± 0.04 (0.58)	0.28 ± 0.04 (0.29)	2.45 ± 0.58 (2.92)
TiO$_2$-PbS/CdS-PbS (*p-i-n*)	21.2 ± 2.3 (23.5)	0.65 ± 0.03 (0.65)	0.43 ± 0.04 (0.42)	5.93 ± 0.64 (6.42)

Results are averaged with standard deviation across 12 samples on 4 different substrates. The J_{sc}, V_{oc}, FF and PCE of champion devices are quoted in brackets.

6.5   Conclusion

In conclusion, having a CdS shell confers better surface passivation and improves device V_{oc} but deteriorates device performance due to its intrinsic nature and poorer charge transport properties. This confines devices to have a thinner active layer which in turn limits the amount of light being absorbed. Therefore to overcome that, two different approaches were proposed. The first approach deals with utilizing the quantum funnel effect, which channels charge towards sites of equal or lower energy level regardless of the direction of the internal electric field. By blending CQDs of two different sizes together, this increases the extent of interface between the two differently sized populations of CQD and the quantum funnel effect could occur in 3 dimensions. However, by blending PbS/CdS CQD instead of PbS, a pronounced increased in PL lifetime is observed, which is attributed to a reduction in non-radiative recombination due to CdS shell passivation. With the PbS/CdS blended film sandwiched between low gap and wide gap PbS/CdS CQD to form the active layer, device performance improved over devices with 200 nm thick of mono-sized PbS/CdS layer as the blend aids to extend the depletion width in the device by quantum funnel effect. The second approach utilizes the concept of *p-i-n* solar cell to create a graded structure based on the wide band metal oxide semiconductor as the *n*-type material, PbS

film as the *p*-type material and PbS/CdS film as the intrinsic material. Two scenarios were considered: putting *p*-type PbS as the bottom layer or by forming an upright device structure with *p*-type PbS on top. Both *p-i-n* device structure showed improvement over their respective control devices of the same extended active layer thickness. However, the upright structure gave the best performance due to a more highly doped *n*-type material and junction being closer to the illumination source. In both cases, it could be said that the improvement in device performance even with thicker active layer comes from the stronger internal electric field created by the Fermi- energy difference between the n-type material and p-type PbS. The internal electric field increases the extent of drift transport and helps to overcome the poor charge transport properties of the PbS/CdS layer. Nevertheless, it has to be acknowledged that the fill factor of devices are still relatively low (<0.50). For further improvement in device performance, that has to be looked into.

Chapter 7 – Improving fill factor with P3HT as a hole transport layer

This chapter presents the use of P3HT as a hole transport material for the purpose of enhancing diffusive transport of charges in a solar cell device in an effort to reduce the reliance of depletion width for photocurrent extraction. Enhanced charge extraction due to the balanced charge extraction rate that minimises space charge built up and the extra charge selectivity imparted by the hole transport material, is shown to benefit PbS CQD solar cells in terms of improving fill factors. The approaches to achieve devices with high fill factors include optimisation of hole transport material and understanding the effect of hole transport layer inclusion via optoelectronic characterisation. Mr Yujiro Tazawa carried out all Kelvin probe measurements while Dr Haibo Jiang handled all secondary ion mass spectrometry (SIMS) measurements.

7.1   Introduction

Chapter 5 examines the importance of surface defect passivation by introducing a core/shell passivation strategy in a bid to cut down recombination losses and to gain open-circuit voltage (V_{oc}). However, low defect concentration meant a lower carrier concentration, resulting in poorer charge transport properties. Therefore in chapter 6, attempts were made to circumvent the low defect density and intrinsic nature of PbS/CdS core/shell CQD by incorporating them into devices with novel architectures and applying concepts which aided in overcoming the poor charge transport properties of PbS/CdS CQD. Yet, the fill factor (FF) of all devices discussed so far is below 0.50. In this chapter, the aim is to address the issues of low fill factors by first understanding the mechanism leading to it and then by exploring the options for engineering the interface between the CQD layer and the top

electrode to improve hole extraction. By adding a suitable hole transport material, the charge transport could be improved due to a more balanced hole and electron extraction rate at both electrodes, coupled with reduced rear contact recombination by forming a charge selective contact and reduced shunt pathways due to better interface morphology between gold and PbS.

At voltages around the maximum power point, charge transport by drift is very much reduced due to a reduction in depletion width generated at the heterojunction. Since the diffusion length of carriers in PbS systems are short (<100 nm)[174], shifting from a drift dominated to a diffusion dominated charge transport mechanism results in poor fill factors for devices thicker than the diffusion length due to more charges recombining before extraction[165]. *Figure 7-1* illustrates the concept of a diminishing depletion width at higher forward bias, which results in diffusion becoming the dominant transport mechanism. At the same time, unbalanced charge extraction[170] causes space charge to accumulate just before the electrode, hence increasing recombination. Also, parasitic resistance losses arising from film inhomogeneities creates shunt pathways[175], and there is contact resistance between the CQD film and metal electrode[100]. All these lead to low *FF*. For further efficiency enhancement, it could be proposed that CQD devices need to shift away from relying principally on drift transport and to look at ways to improve diffusive charge extraction[170].
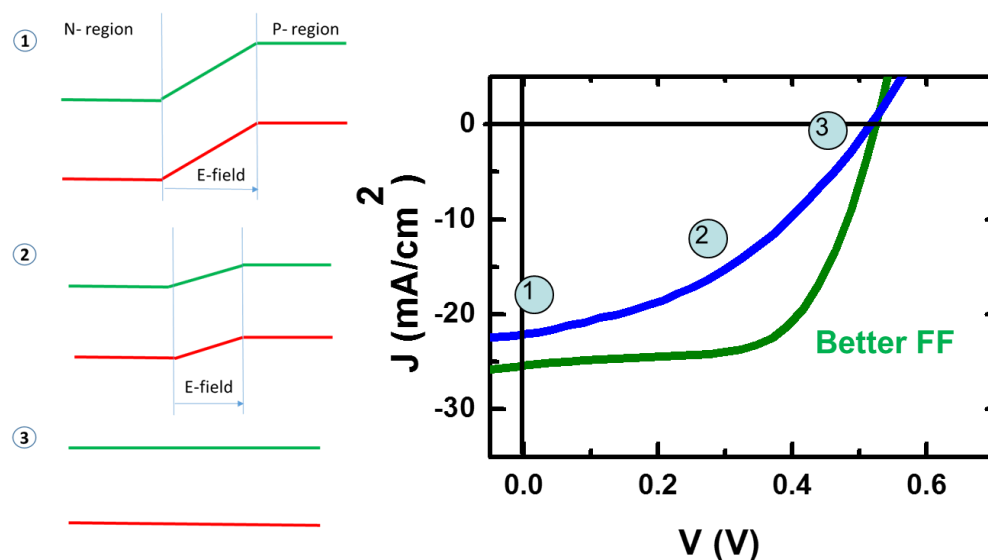
Figure 7-1. A diagram illustrating a solar cell that has poor carrier diffusion length (blue line) versus one that has superior carrier diffusion length (green line). When the solar cell is operating at higher forward bias, carrier extraction drops because drift transport is limited (smaller depletion width) and with lower carrier diffusion length, carries tends to recombine before extraction, as reflected by the lower photocurrent (position 2 of blue curve)

Even before the discussion on inserting a hole transport layer, the first step toward making a device with high *FF* is the preparation of a one-step deposition PbS ink, derived using a solution phase ligand exchange approach. The benefit of a solution-phase ligand-exchanged CQD solution is discussed in section 3.2.1. To prepare the one-step deposition PbS ink, 1.3 eV PbS CQDs in octane with oleic acid as their native ligand are first subjected to a solution phase ligand exchange to yield iodide-capped PbS (henceforth termed PbS-Iodide), which is finally dissolved in butylamine to a concentration of approximately 200mg/ml according to the procedure as described by Ning *et al.*[70] (see section 4.2.5 for more details). The iodide ligand is much smaller sterically as compared to native oleic acid (OA) ligand, allowing the quantum dots to be much closer together. Films of PbS-Iodide are formed by spincoating 3000 rpm on a substrate and then annealing at 90°C for 3 minutes. The success of ligand exchange is shown in *Figure 7-2*, where the retention of the exciton

peak signifies that the quantum dots still exhibit quantum confinement and aggregation of the quantum dots is absent. The redshift in the exciton peak after ligand exchange implies there is wavefunction delocalisation and energetic coupling[176] amongst the PbS CQD since they are now much closer to one another. The benefit of a solution-phase ligand-exchanged CQD solution is that a secondary ligand exchange step while spin coating is not needed, and this ensures improved film homogeneity and reduces macro defects which would otherwise deteriorate the *FF*. Using a Dektak profiliometer, for a 220 nm thick PbS-Iodide film, average roughness is 7 nm while a EDT- exchanged PbS CQD film of about 200nm thick has an average roughness of 17 nm.
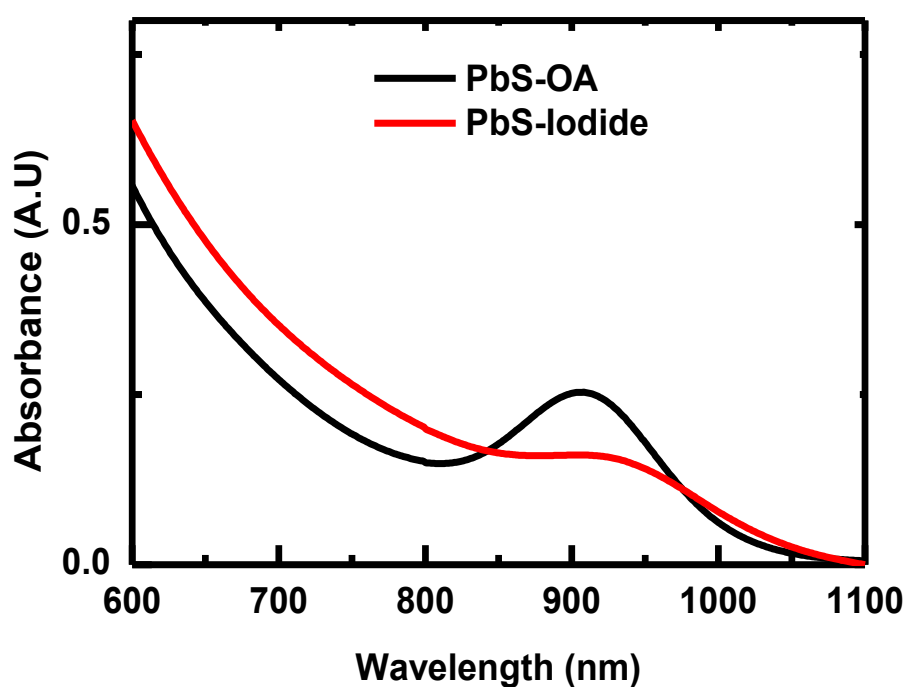
Figure 7-2. UV-Vis spectrum of PbS CQD before and after solution phase ligand exchange. The redshift of the excitonic peak is attributed to the delocalisation of the wavefunction between quantum dots.

Further improvement to *FF* is sought by the use of semiconducting polymer Poly(3-hexylthiophene-2,5-diyl) (P3HT). The insertion of P3HT as an interfacial layer between

PbS-Iodide CQD film and the top electrode, to create efficient CQD devices is described. Also, the physicochemical properties of P3HT were altered to optimise device performance and more characterisation was carried out to understand the role of P3HT in improving device performance. With P3HT, improved fill factors of up to 0.72 and air-stable devices of up to 8.1 % efficiency were fabricated. In the next section, further details on how the selection of hole transporter material was made are discussed.

7.2   Choice of organic hole transport material

Recently, Chuang *et al*. made devices which consist of 10 layers of iodide- exchanged PbS and two layers of EDT exchanged PbS before the gold electrode. The PbS film with EDT ligand has a more *p*-type nature (lower Fermi energy) than the iodide- exchanged PbS film, resulting a local band bending that aids in blocking electrons and allowing hole transport. The improvement to diffusive transport by imparting charge selectivity has raised the fill factor (*FF*) to 0.6[65]. Another approach is to use a different hole transport material to balance charge extraction rates[177–179], which could simultaneously play a role as a smoothing interfacial layer between the active material and the top electrode. In organic photovoltaics, a common choice of hole transport is PEDOT:PSS or molybdenum trioxide (MoO_3)[180]. In the case of organo-lead halide perovskite solar cells, $N^2,N^2,N^{2\prime},N^{2\prime},N^7,N^7,N^{7\prime},N^{7\prime}$-octakis(4-methoxyphenyl)-9,9′-spirobi[9H-fluorene]-2,2′,7,7′-tetramine (SPIRO OMeTAD) is often used[181] although other alternatives have been explored[179,182,183]. In the context of PbS CQD solar cells, PEDOT:PSS and MoO_3 have been used. For PEDOT:PSS, it is often applied as a bottom layer on the transparent conducting electrode as a smoothing layer as well as an interface to help bind PbS to the substrate[167]. MoO_3 is usually applied, via evaporation, as a top layer on PbS and before the top metal electrode deposition. The benefit of MoO_3 is that it removes the Fermi pinning effect of the metal on PbS, enabling even metals with smaller work function (like silver and aluminium) to serve as an ohmic rear contact[184].

Mora-Sero *et al*. stressed the importance of using charge selective contacts to improve charge extraction [170]. However, much attention has been focused on the electron collecting component of the device, for example providing a depleted heterojunction[185] and engineering the *n*-type material to improve electron collection[101]. Less attention has been given to hole collection.

For this work, P3HT was chosen as a hole transporter for the PbS active layer because it is a well-known *p*-type organic semiconductor with a relatively high hole mobility and literature suggests that its HOMO and LUMO levels with respect to 1.3 eV PbS CQD are suitable to perform the role of hole extraction and electron blocking[186]. Furthermore, the conductivity of P3HT can be modified [187,188] which is very useful for optimising carrier extraction, fill factor and hence power conversion efficiency.

Before fabricating devices with P3HT as a hole transport layer, a photoluminescence (PL) quenching trial is carried out to validate its hole transporting efficacy. Here, PEDOT:PSS and SPIRO OMeTAD are also selected to be tested in this trial against P3HT, based on their HUMO-LUMO level suitability. PEDOT:PSS (Clevios™ P VP AI 4083) was used as-purchased, SPIRO OMeTAD (Solaronix™) was prepared in chlorobenzene together with its standard dopant with concentration specified by reference[189] and P3HT was prepared by dissolution in chlorobenzene to a concentration of 10 mg/ml. First, PbS-Iodide films are formed on a microscopic glass side and broken into two smaller pieces to ensure similar thickness (of about 220 ± 7 nm). One sample is kept as a control (without any hole transport materials) and the other is coated with a hole transport material. PL results showed that P3HT performs the best in terms of acting as a hole transport material for PbS as can be seen by the extent of PL quenching. The quench in PL intensity implies that charge separation is occurring at the interface[144] and in this case, holes are being extracted into the hole transport material, reducing the number of free photo-excited carriers left in PbS-

Iodide film to radiatively recombine. A further trial was done by utilizing the different hole transport materials in actual devices. This will be described in the next two sections.
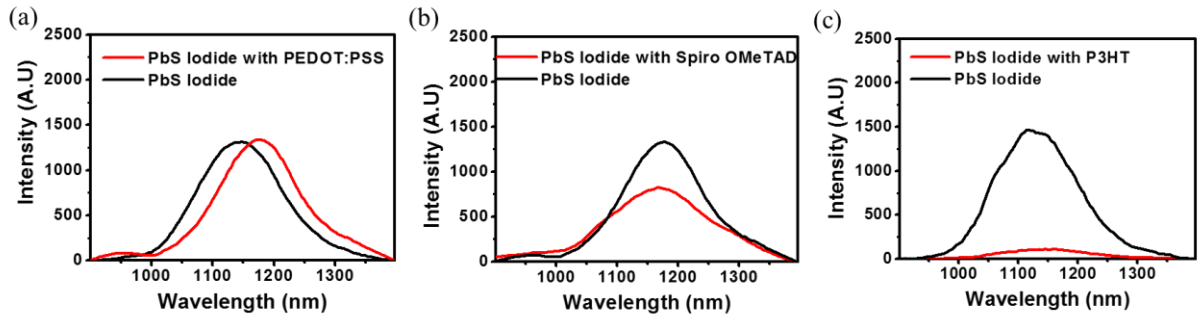
Figure 7-3. PL quenching experiments with the various hole transport materials on PbS-Iodide film, namely (a) PEDOT:PSS (b) SPIRO OMeTAD (c) P3HT.

7.3   Device fabrication
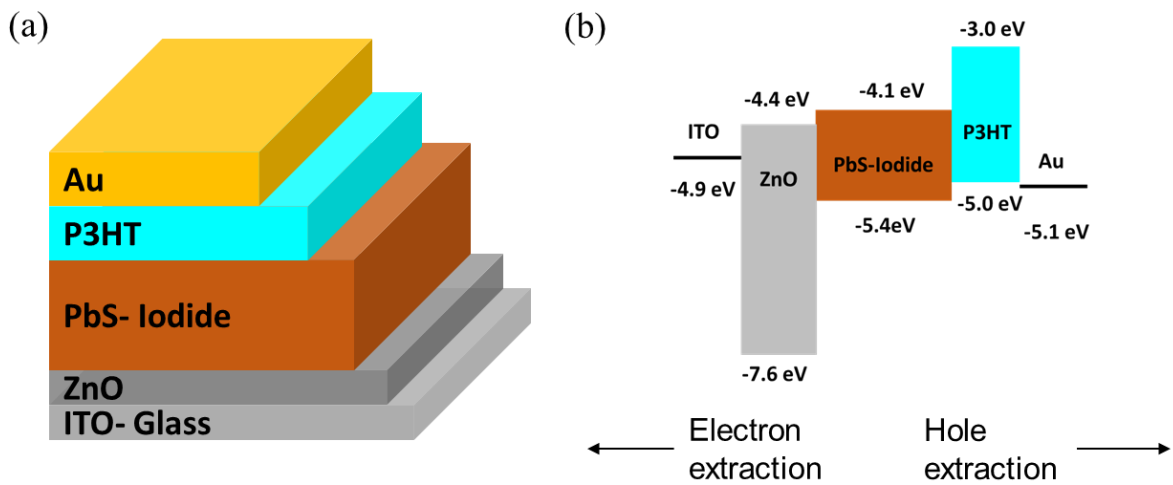
Figure 7-4. (a) Schematic representation of solar cell device architecture containing P3HT as hole transport material and (b) the corresponding proposed band alignment (values for ZnO, PbS-Iodide, and P3HT are taken from references [190], [80], [186] respectively). Control samples exclude the P3HT layer.

Patterned ITO substrates were cleaned thoroughly and then treated with O_2 plasma as described in section 4.4.1.3. A 100 ± 7 nm ZnO layer was deposited by spin-coating the

prepared ZnO nanocrystal colloidal solution onto ITO at 2000 rpm for 30 s. A PbS-Iodide film is then deposited on the ZnO film by spin coating 10 μL of PbS-Iodide solution at 3000 rpm for 30 s and then annealed at 90°C for 3 mins. For devices with P3HT as the hole transporter, a 10mg/mL P3HT in chlorobenzene solution is spin-coated above the PbS-iodide layer at 1000 rpm for 45 s to form a 100 ± 5 nm film. For O_2 plasma treatment, the P3HT coated film is exposed to O_2 partial pressure of 120 mTorr for the required amount of time. Finally top electrodes were formed by depositing gold by thermal evaporation, as detailed in section 4.4.3. The device structure and the proposed band diagram are illustrated in *Figure 7-4*. For devices with SPIRO OMeTAD and PEDOT:PSS, the procedure is the same as that for P3HT devices but they are spun at 6000 rpm and 2000 rpm, giving thicknesses of 143 ± 6 nm and 84 ± 9 nm respectively. For comparison with the devices prepared by Chuang *et al*., another set of devices are coated with two more layers of oleic acid terminated PbS CQD (of the same band gap) but exchanged with EDT ligands.

7.4   Initial results

As a first trial, devices with different hole transport material and interfaces were made and compared. The samples were left in air (but in the dark) for a day before gold electrode evaporation. *Figure 7-5* shows the performances of the best devices represented in this trial. The results show that P3HT performs the best as a hole transport material, based on overall device performance. This supports the conclusion made in section 7.2. Specifically, devices with P3HT gave remarkably high *FF*, which signifies that the charge transport and extraction processes have been improved. Conversely, even with suitable HUMO-LUMO levels, SPIRO OMeTAD and PEDOT:PSS result in poorer device performance than the control and this shows that firstly the choice of hole transport material is crucial and secondly, the ultimate band alignment is affected by the interfacial interaction between the

two materials. In this case, SPIRO OMeTAD and PEDOT:PSS may not align favourably

with PbS-Iodide therefore resulting in low currents and *FF*.
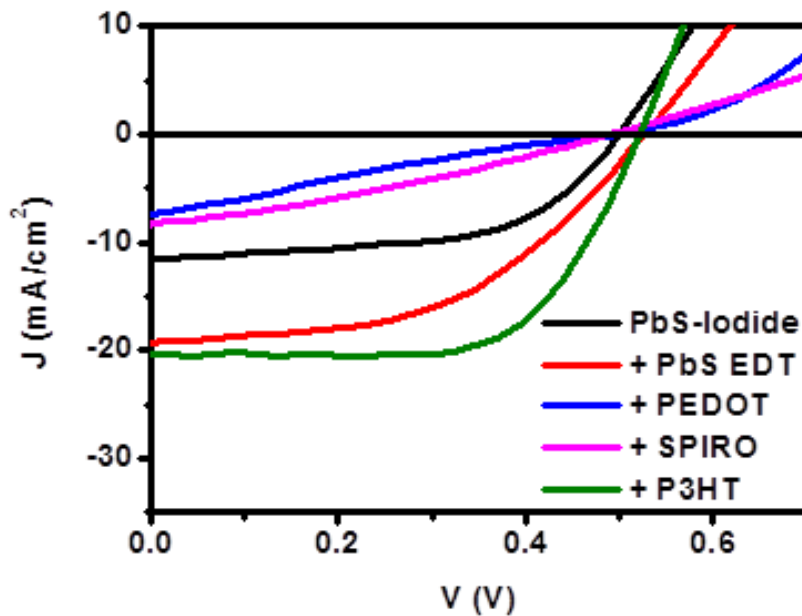
Figure 7-5. J-V curves of the best devices with different hole transport material/interfaces. PbS-Iodide curve represents the sample with no hole transport material added.

Next, the focus is shifted towards P3HT and this time, another set of devices were made

and the standard *J-V* characterisation was carried out as soon as devices were fabricated. A

comparison of performances for the best devices with and without P3HT is shown in *Figure*

7-6. The device with P3HT has improved short-circuit current (J_{sc}) and open-circuit voltage

(V_{oc}) over the control device. However, the as-fabricated devices exhibit a "roll-over effect"

or a kink in the power quadrant of the *J-V* curve, thereby limiting *FF* and overall *PCE*. This

effect has been discussed by a number of authors and it was suggested that the abnormal

shape of the *J-V* curve is due to the existence of a barrier to charge injection[100,191,192]

However, when devices are stored in the dark and in air-ambient for one full day, this roll-

over effect is eliminated, leading to a marked improvement in fill factor and overall device

performance *Figure 7-6(b)*. It is hypothesised that this improvement upon ageing is due to P3HT oxidation, which has been previously shown to cause *p*-type doping, shifting its HUMO-LUMO levels and increasing its work function[193]. To explore this further, Kelvin probe measurements were used to track the Fermi energy (E_F) or work function position of PbS-Iodide and P3HT as produced in an inert glove box atmosphere and after exposure to air. After two days, there is little change in the PbS-Iodide E_F and it remains at -4.91 ($\pm$0.02) eV while the P3HT drops from -4.75 ($\pm$0.02) eV to -4.80 ($\pm$0.02) eV bringing it closer to the PbS value. This, together with a systematic energy shift of core-levels and HOMO levels on the oxidation of P3HT as observed by Hintz *et al.*[193], makes hole injection more favourable at the interface (see *Figure 7-7*).
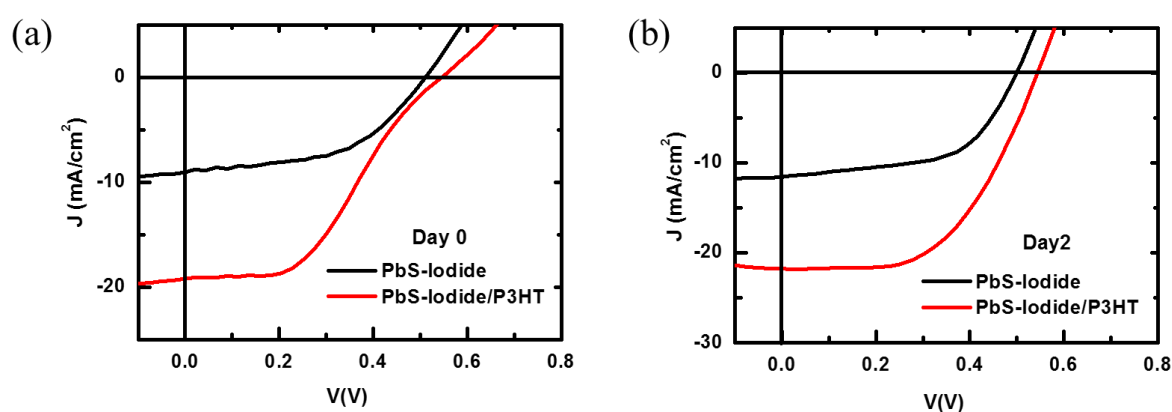
Figure 7-6. Device performance comparison, with and without the untreated P3HT hole transport layer, (a) as fabricated and (b) after 2 days of storage in air.
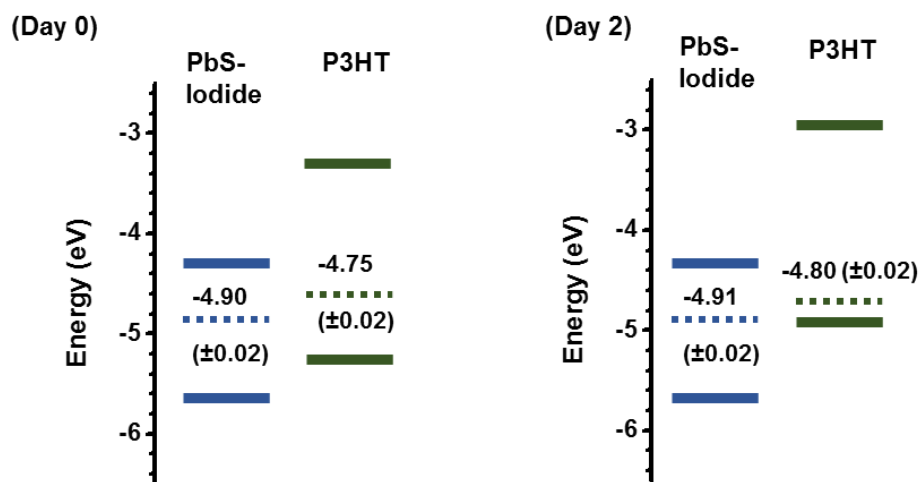
Figure 7-7. Energy level diagram and position of Fermi level of the PbS active layer and P3HT as measured by scanning Kelvin probe on the day of fabrication and after 2 days of storage in air. The associated uncertainties are quoted in parenthesis.

The origin of improved device performance will be investigated based on the hypothesis that P3HT is acting as a combination of: i) an electron blocking layer minimizing rear contact recombination[179]; ii) a hole transport layer to improve the balance of carrier extraction rate (as opposed to only having a ZnO layer) and thus reducing the formation of space charge at the electrodes[170]; iii) a smoothing layer between the PbS-Iodide film and the gold contact to minimise shunt pathways; and iv) an optical spacer layer increasing reabsorption of light that is reflected off the rear electrode[194]. However before doing so, devices are optimized by controlling the extent of beneficial oxidation of P3HT and then characterising the physical and chemical changes to P3HT.

7.5   Optimization and characterisation

7.5.1   Intentional oxidation of P3HT

To control the extent of oxidation, an O_2 plasma treatment was employed to physicochemically etch the P3HT. Keeping the O_2 partial pressure constant at 120 mTorr, various plasma exposure times were used and *Figure 7-8(a)* shows how the *J-V*

characteristics change as a function of treatment time. A three second treatment gives optimal device performance (J_{sc} 20.7 mA/cm^{-2}, V_{oc} 0.52V, *FF* 0.63 and *PCE* 6.8%). Kelvin probe measurements (*Figure 7-8(b)*) go some way to explain this observation, as a three second treatment results in a E_F value of -5.04 ($\pm$ 0.01) eV as compared to the pristine value of -4.80 ($\pm$0.02) eV which, after band alignment, means that the HOMO level of P3HT might be at a more ideal level to encourage hole injection from the PbS-Iodide layer. *J-V* characterisation exhibits no rollover effect on devices tested immediately after fabrication (see *Figure 7-9*), which is not the case for devices without the P3HT O$_2$ plasma treatment (compare with *Figure 7-6*). The plasma treatment also thins the P3HT layer, as shown in *Figure 7-8(c)*, and for the three second treatment, the P3HT thickness reduces from 102nm to 67.5nm (as measured using Dektak Profiliometer). This most likely plays a secondary but still an important role in optimising charge transport and collection in the device. Even though work function continues to increase with increasing treatment time, the P3HT layer becomes too thin and degradation of the device performance ensues. In the next section, the importance of P3HT thickness is investigated.
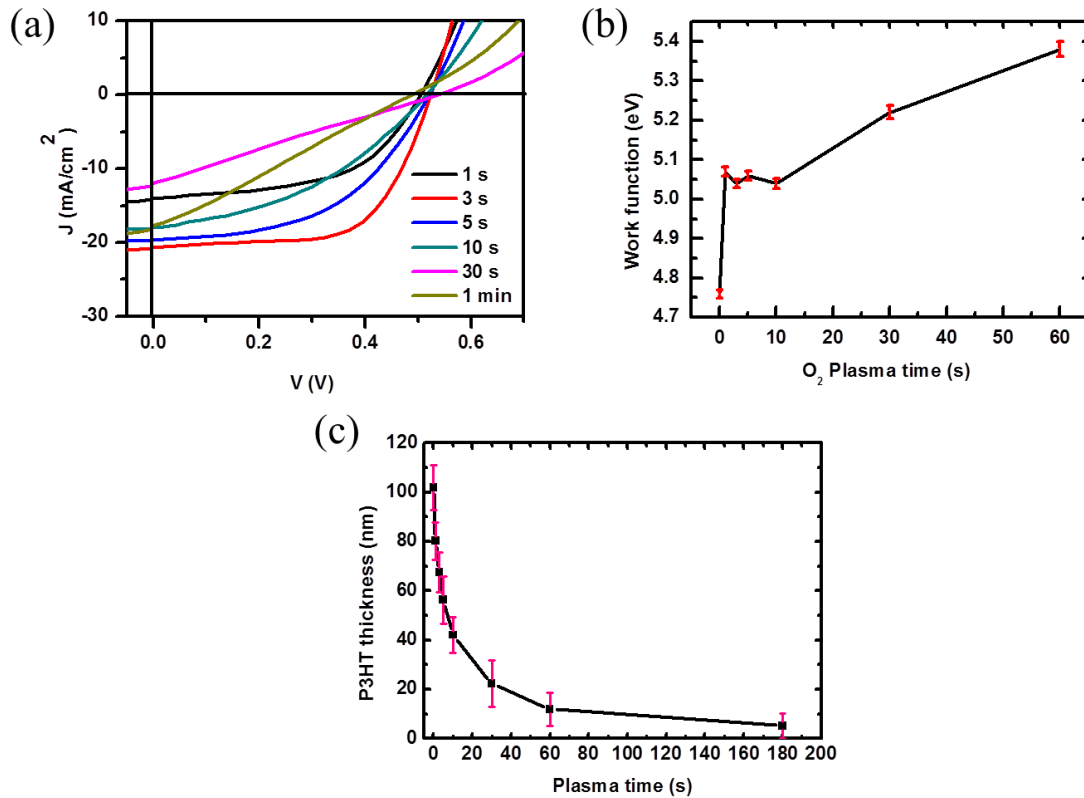
Figure 7-8. (a) J-V characterisation of device with P3HT layer exposed to increasing O_2 plasma treatment times. 3 s is found to be the optimal treatment time for PCE. (b) Scanning Kelvin probe measurements on P3HT with increasing O_2 plasma treatment time. (c) Graph of P3HT thickness versus length of O_2 plasma treatment.
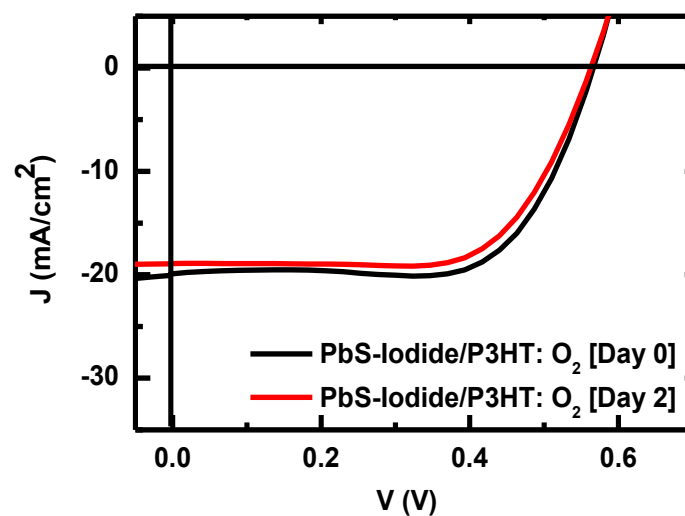
Figure 7-9. Device performance, with P3HT layer exposed to 3 s O_2 plasma treatment, when as-fabricated and then tested again after two days of air-ambient storage in the dark.

7.5.2 P3HT thickness optimization

To investigate the effect of P3HT thickness on device performance, devices with the same PbS-Iodide thickness but with different thicknesses of P3HT layer were fabricated. To vary the thickness of P3HT, the spin rate was altered and a calibration curve was obtained as shown in *Figure 7-10(a)*. Devices were tested after 2 days exposure to air and the performance results are shown in *Figure 7-10(b), (c)*. V_{oc}, J_{sc} and *FF* all decrease with thinner P3HT layers, while too thick a P3HT layer gives high J_{sc} but much lower *FF*. These trends follow very closely the work of Tress *et al.*[195], who show that a sufficiently thick (~400nm) layer of Spiro-OMeTAD is required to form an interface between the perovskite layer and top electrode. The reason for that thickness is due to the relatively rough perovskite surface, so as to ensure that the hole transporter is able to form a smooth uniform contact with the top electrode, thus reducing shunt pathways. However, it is also shown that beyond the optimal thickness, a thicker hole transport layer reduces *FF* due to increased series resistance. In the case of PbS-Iodide, it has a much smoother surface than the perovskites conferred by the solution phase ligand exchange method. It is established that the optimum P3HT thickness for device *PCE* was about 100 nm as shown in *Figure 7-10(c)*.
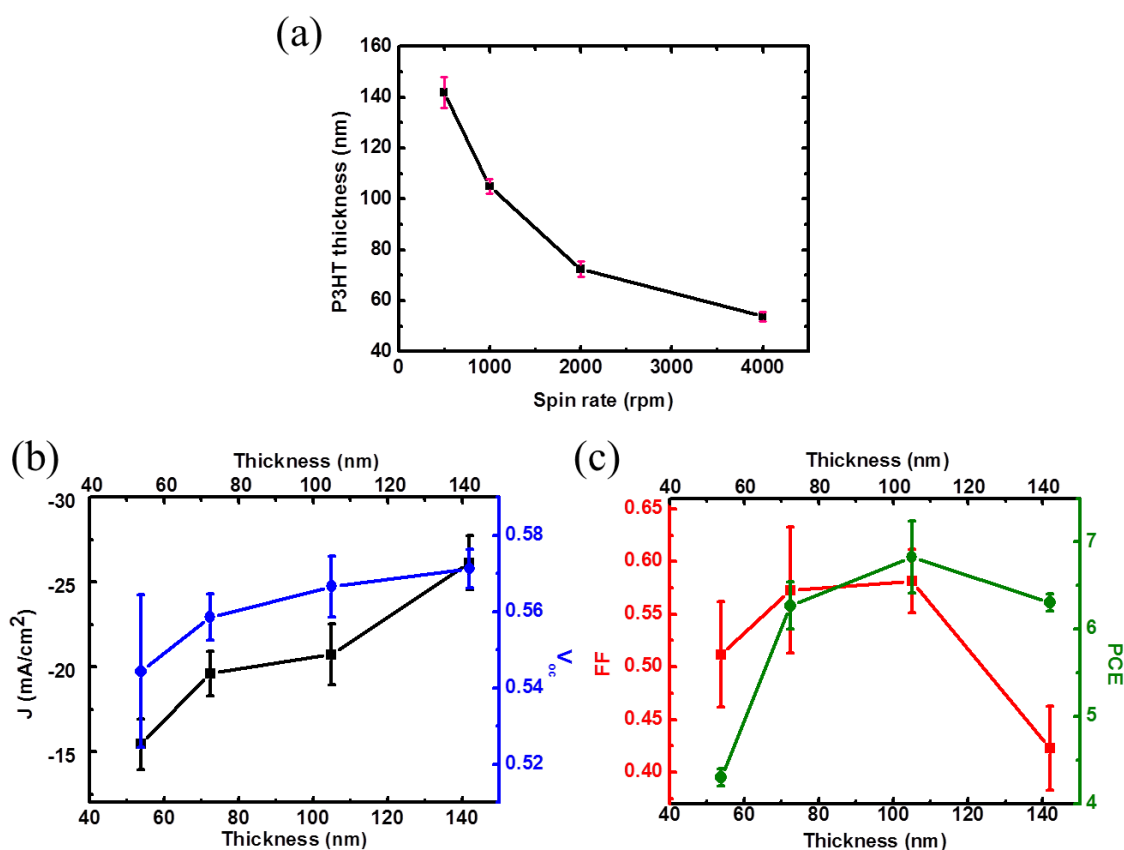
Figure 7-10. (a) Graphs of P3HT thickness versus spin rate. (b) Device J_{sc} and V_{oc}, (c) FF and PCE with different thicknesses of P3HT layer. Results are obtained two days after fabrication for the elimination of the "roll-over" effect.

7.5.3 Material characterization

To understand the chemical effect of the O_2 plasma, UV-Vis-NIR absorption, Fourier Transform Infrared Spectroscopy (FTIR) and Secondary Ion Mass Spectrometry (SIMS) have been employed. The UV-Vis-NIR spectra in *Figure 7-11* shows how the absorption changes in the P3HT with various O_2 plasma treatment times. The magnitude of absorbance is reduced with plasma treatment time, consistent with layer thinning, but the effect could also be ascribed to chemical degradation of the P3HT thiol ring due to oxidation. Oxidative degradation is also known to result in a blueshift in the absorption spectrum due to the reduction in molecular weight of the polymer chain[196]. However, in this case, the blue shift

is minimal, which means that any oxidative effect of plasma mainly changes the chemical moiety in the polymer rather than cleaving it into to smaller fragments. This would be consistent with a *p*-type doping effect and Fermi level shift of P3HT[193]. Further, FTIR measurements (*Figure 7-12*) show evidence of increased oxidation of P3HT with 3 s O_2 plasma treatment: The O-H bonds at 3360cm^{-1} and C=O bonds at 1718cm^{-1} appear upon plasma treatment while there is slight degradation of the hydrocarbon peaks at 2800-2900cm^{-1} (*Figure 7-12(c)*)[19,24].
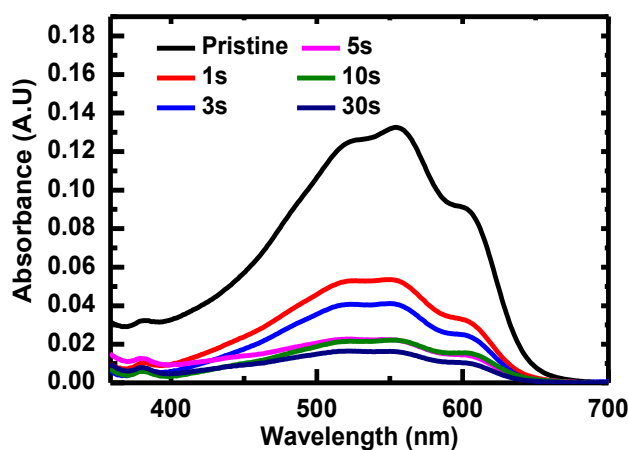
Figure 7-11. UV-Vis absorbance spectra of P3HT films cast on glass slides which have been exposed to various O_2 plasma treatment times.
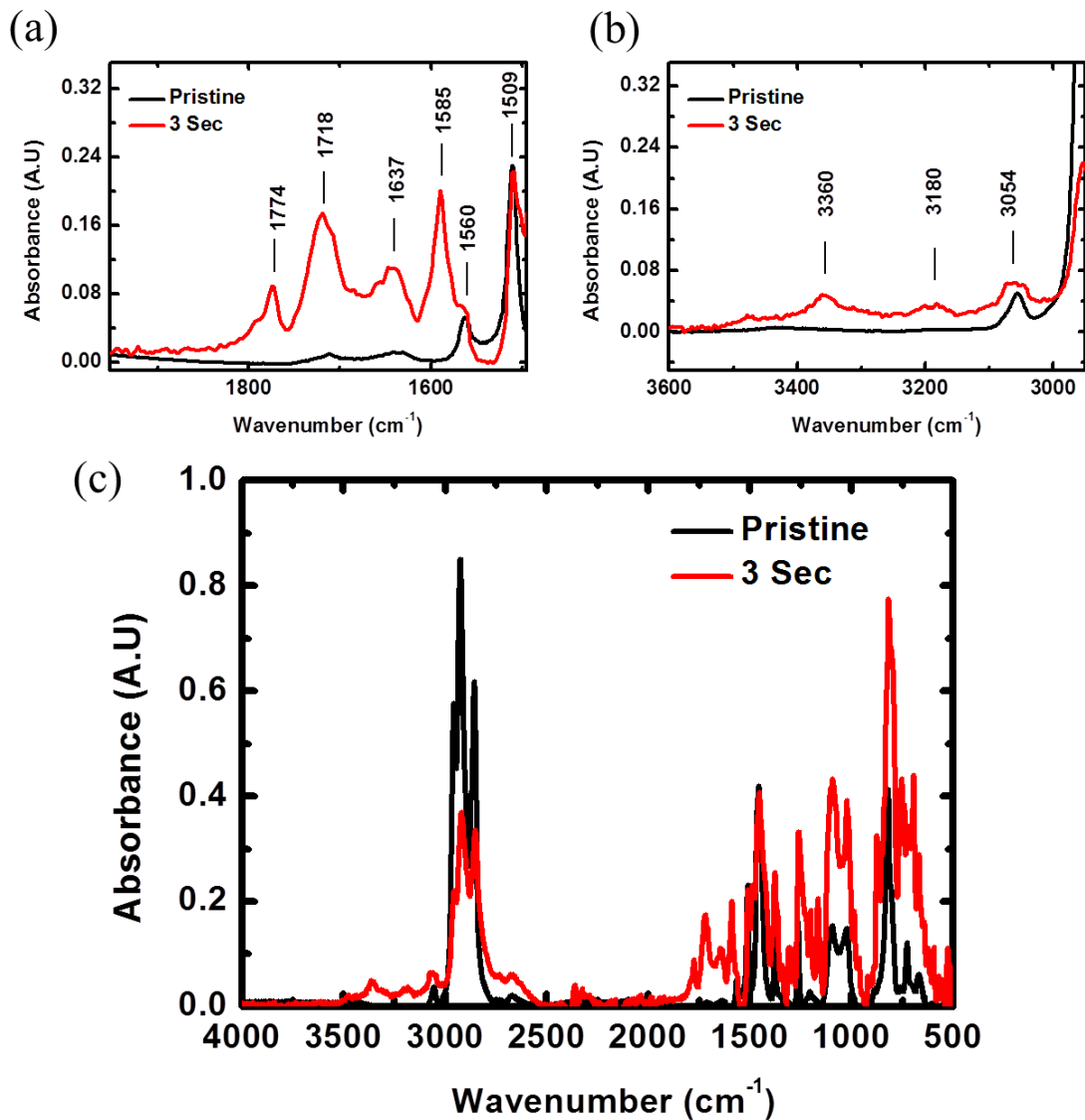
Figure 7-12. (a) FTIR spectra showing the range of wavenumbers attributed to C=O stretching (1774 cm^{-1}, 1718 cm^{-1}, 1637 cm^{-1}, 1585 cm^{-1}) while 1560 cm^{-1} and 1509 cm^{-1} are associated with aromatic components in P3HT, and (b) O-H stretching (3360 cm^{-1} and 3180 cm^{-1}) while 3054 cm^{-1} is associated with aromatic C-H bonds[197]. (c) The full range of the FTIR spectra.

SIMS was used, in the depth profile mode, to investigate the extent of oxidation, as illustrated in *Figure 7-13*. The different regions in the depth profile for each device under different conditions are estimated as such: (i) using the minimum of ^{12}C depth profile (*Figure 7-13(d)*) to demarcate the boundary between P3HT and PbS-Iodide, and (ii) using the increase in ZnO counts in each depth profile to indicate the start of the ZnO layer.

Further information can be garnered by comparing the ratio of oxygen to sulphur counts between pristine, air-aged, and O$_2$ plasma treated P3HT-devices under the same experimental conditions (*Figure 7-14*). The oxygen-sulphur ratio is higher in the air-aged sample and even greater in the O$_2$ plasma-treated sample. More oxygen is present throughout the thickness of the P3HT layer in the plasma treated sample as compared to the air-aged sample. From this, it can be concluded that the extent of oxidation with plasma treatment is significantly greater than from air ageing alone. This increased oxygen to sulphur ratio has been similarly reported using X-ray photoelectron spectroscopy (XPS) with oxidized P3HT by Hintz *et al.*[193]. Therefore, this supports the hypothesis that it is oxidation of the P3HT that increases the work function [193], and reduces the charge injection barrier and "heals" the device performance.
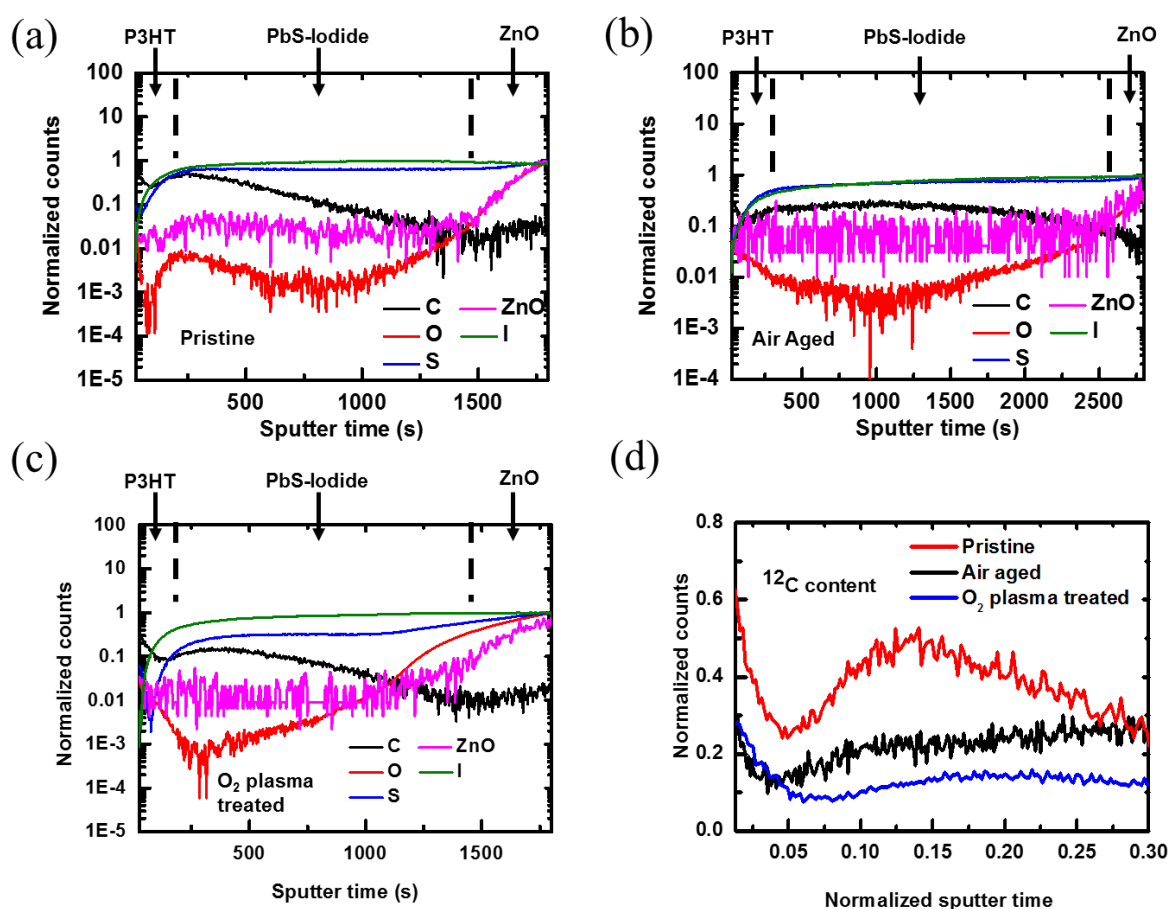
Figure 7-13. SIMS depth profiles of (a) Pristine ZnO/PbS-Iodide/P3HT sample, (b) ZnO/PbS-Iodide/P3HT sample that has been air aged for 2 days and (c) ZnO/PbS-Iodide/P3HT sample after 3 second O₂ plasma treatment. The approximate zones of each component are demarcated with dotted lines. d. Carbon content trace of each device, normalized also in the time component. The minimum of carbon trace indicates the interface between P3HT and PbS-Iodide (at time= 0.05).
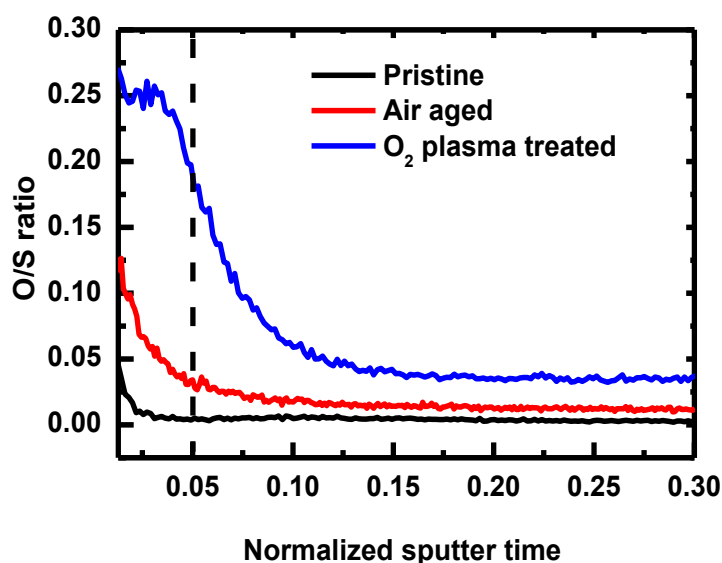
Figure 7-14. Ratio of oxygen to sulphur counts as determined by SIMS, dotted line shows the approximate position of the end of P3HT component and the start of PbS-Iodide, which is determined from depth profile analysis as shown in Figure 7-13(d).

7.5.4 Electronic characterization

To show the importance of using a hole transport layer to improve the balance of charge collection rate, the optoelectronic properties of test devices with and without the P3HT layer, and with O₂ plasma treated P3HT (hereby termed P3HT:O₂) are investigated. *Figure 7-15(a)* depicts the dependence of J_{sc} on light intensity of devices with and without the P3HT layer; the measurements of all these devices are taken at day 2 of storage in air-ambient and dark. Results are fitted to a power law relation,

$$J = bI^a \hspace{4cm} \textit{Equation 7-1}$$

177

where *J* refers to current density, *I* is the light intensity and *a*, *b* are constants. If *a*=1, it implies that device is operating under the condition that charge extraction rate is balanced and therefore there is minimal bimolecular recombination. For *a* <1, it indicates a deviation from balanced charge transport resulting in the formation of space charge[198]. Devices with the hole transporter layer have values of *a* approaching the value of 1, which is consistent with the high fill factors observed. On the other hand, the lack of hole transport results in space charge-limited current extraction, which results in devices having more bimolecular recombination[199]. Open-circuit voltage decay measurements were also performed as shown in *Figure 7-15(b)*. Under open-circuit conditions, photogenerated charges build up under illumination and the eventual decay of the voltage is a result of recombination of those charges. If the lifetime of the photovoltage decay is long, it signifies a pronounced reduction in carrier recombination rate[200], and this is seen in the case when P3HT is used.
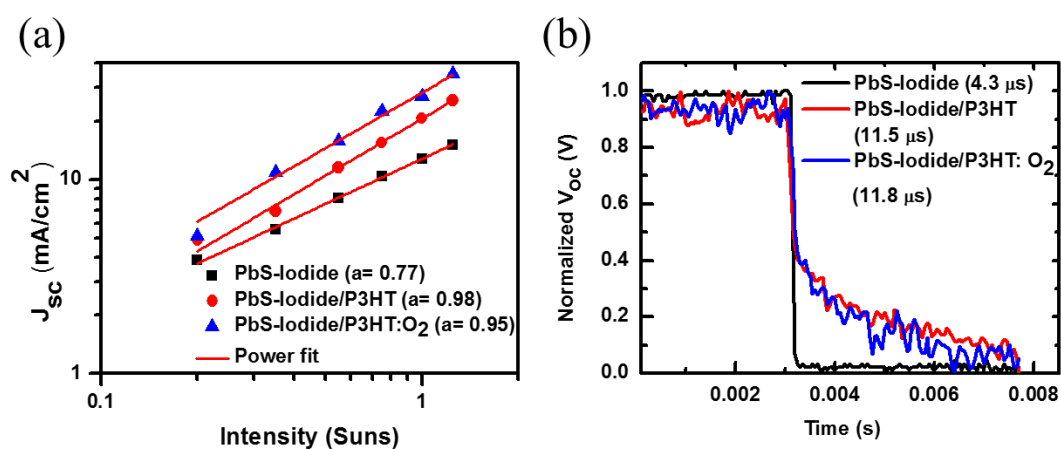
Figure 7-15. (a) Intensity dependent short-circuit current trace of the devices with and without P3HT and O₂ treated P3HT, with proposed power law fit. Fitted power exponent with standard errors are: a=0.77 ± 0.01 for PbS-Iodide, a=0.98 ± 0.03 for PbS-Iodide/P3HT and a=0.95 ± 0.05 for PbS-Iodide/P3HT:O₂. (b) Open-circuit voltage decay of the same devices with lifetime quoted in parentheses.

7.6   Device performance and stability

N-type ZnO thin films are known to possess high carrier density[201] and are commonly used as electron selective contacts. In the control devices (without P3HT), symmetry is absent: with the electron collection process dominating over hole collection, it is very likely that space charge accumulates near the regions of the electrodes. This limits charge transport and promotes charge recombination[170]. Suitably doped P3HT has a Fermi energy level that allows a more ideal band alignment to extract holes from PbS layers and with a relatively high LUMO position, P3HT effectively blocks electrons at the rear electrode, thus reducing recombination. Therefore, having both electron and hole selective contacts aids charge extraction in the diffusive transport regime[170]. Thus, at high forward bias, where the internal field is weaker and the depletion width is small, diffusive transport takes precedence and with charge selective contacts a higher photocurrent can be sustained, leading to higher fill factors. Another interpretation of these results is that P3HT acts as a buffer layer eliminating Fermi level pinning effects that are known to exist between gold and PbS[100]. All these factors lead to improved charge extraction compared to device without P3HT, leading to better J_{sc}, V_{oc} and *FF* values as evident in *Figure 7-16(a)*.
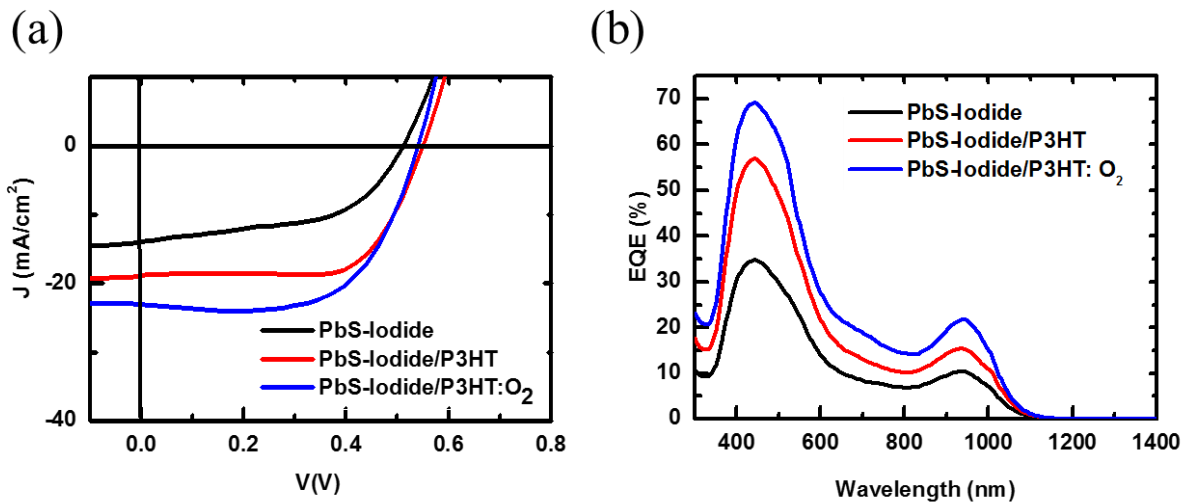
Figure 7-16. (a) J-V sweeps showing photovoltaic performance under AM1.5 illumination of device with 100 nm of P3HT, without P3HT and with O_2 treated P3HT. Measurements were taken two weeks after fabrication, where device performance has stabilized. (b) External quantum efficiencies of the corresponding devices.

Devices with fill factors as high as 0.72 were fabricated, which is by some margin the highest reported for PbS CQD solar cells (refer to *Table 7-1* for device performance summary). It could be said that using an O_2 plasma treatment allows a simultaneous control over both the extent of P3HT oxidation and film thickness. The external quantum efficiency measurement in *Figure 7-16* shows a higher photocurrent extracted across the whole wavelength range, in particular near 600nm where photogenerated charges occur mainly in the middle of the device. The improvement of charge extraction in the middle regions of the device supports the hypothesis that an improvement in carrier lifetimes and reduced charge recombination in devices which use P3HT is due to the charge selectivity of P3HT and the elimination of space-charge limited transport. It is also worth noting that there is still a huge deficit in quantum efficiency at higher wavelength regions, which is most likely due to insufficient absorption of light due to the limited thickness of active layer. However, in our studies, the PbS layer is fixed at about 220nm and has not been optimised. That would be a future research task.

Table 7-1. Photovoltaic device performance statistic. Samples are tested in AM 1.5 conditions.

Structure	J_{sc} (mA/cm^2)	V_{oc} (V)	*FF*	*PCE* (%)
ZnO/PbS-Iodide/Au	12.6 ± 2.3 (13.8)	0.51 ± 0.06 (0.51)	0.49 ± 0.05 (0.56)	3.1 ± 0.4 (3.9)
ZnO/PbS-Iodide/P3HT/Au	18.4 ± 1.5 (18.7)	0.55 ± 0.03 (0.55)	0.68 ± 0.04 (0.70)	6.9 ± 0.9 (7.2)
ZnO/PbS-Iodide/P3HT-O_2 treated 3s/Au	19.7 ± 1.7 (21.9)	0.56 ± 0.02 (0.54)	0.67 ± 0.03 (0.68)	7.4 ± 0.4 (8.1)

In addition, the devices are stable in air: device performance metrics as a function of time are shown in *Figure 7-17*. P3HT is susceptible to oxidation and this oxidation causes *p*-type doping and shifts the Fermi energy level, resulting in favourable band alignment and hole injection. Therefore, when P3HT is fully oxidized, the device performance stabilizes and this can be seen in the O_2 plasma treated P3HT devices where the performance is stable on storage. Studies have shown that devices including interfacial transport layers like MoO_3 work well as-fabricated, but changes in work function over time degrade device performance[65].
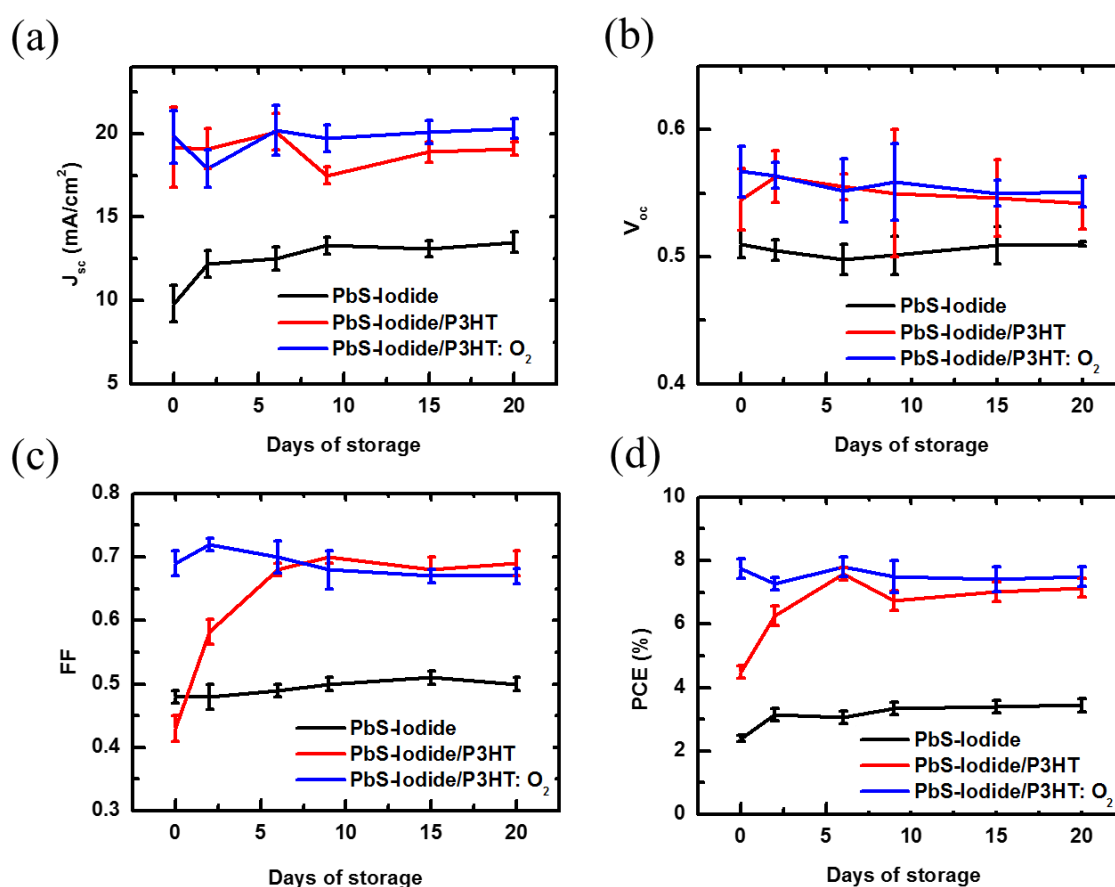
Figure 7-17. The variation of photovoltaic performance metrics of devices, with and without P3HT and O₂ treated P3HT, with storage time. (a) short-circuit current, (b) open-circuit voltage, (c) fill factor and (d) power conversion efficiency. The devices were unencapsulated and were stored in air between each measurement in a dark environment without any humidity control. The standard deviation (error bars) and the average (data point) were calculated from a sample of 9 devices on 3 separate substrates.

7.7 Conclusion

In summary, it was shown that P3HT could be manipulated to be an effective hole transport layer in between the PbS CQD and the gold contact, to balance the rate of charge extraction of both carriers in a device with ZnO as the electron acceptor. P3HT could also act as a smoothing layer, capping the PbS CQD film and thus reducing possible shunt pathways. Lastly, P3HT could serve as a charge selective contact- to block electrons and to allow holes to be transported and this would reduce charge recombination. By oxidising P3HT, its Fermi energy level is found to be lowered, resulting in improved band alignment and sustaining hole injection from the PbS layer even at high forward biases. In addition, devices can be stored in air in the dark for an extended period of time without significant device deterioration and in fact, mild oxidation is beneficial to device performance. An investigation of controlled oxidation via O_2 plasma treatment indicates that oxidised P3HT serves as an excellent hole transport material. It was shown the treatment gave a more uniform oxidation and also thins the P3HT layer. By optimising the conditions, suitably thick and suitably oxidised P3HT contribute to better performing devices with a concomitant improvement to J_{sc}, V_{oc} and FF values when compared to devices without a P3HT layer. Optimised oxidation conditions and P3HT thickness are used to maximise fill factors up to 0.72. Relatively efficient devices with high FF and air stability are made possible with the inclusion of P3HT as the hole transport layer. Nonetheless, the V_{oc} of

these devices are still limited to below 0.6V and it needs to be improved to attain higher

device efficiency.

Chapter 8 – Conclusion and future work

8.1   Conclusion of thesis findings

PbS CQD technology is still in the midst of rapid progress and it is a potential candidate for the low cost, high efficiency third generation photovoltaics. At the beginning of this work, devices for PbS CQD photovoltaics were reported to be about 7 % efficient[60]. Then upon the completion of this thesis, the certified record device efficiency stands at 9.9 %[20]. Along with this came discovery of n-type PbS[70,202], use of solution phase ligand exchange to create one step deposited PbS colloidal ink[69,70,75] and air-stable PbS devices[65,202].

The present work represents a significant contribution to an improvement in V_{oc} and FF of devices and a better understanding of PbS CQD photovoltaics. The key contributions are as follows:

(i) The first part of this work presented a strategy to utilise core/shell PbS/CdS CQDs as the main absorber material in a solar cell. The CdS shell imparts surface passivation as seen from the improvement in PLQY and PL lifetime as compared to unshelled PbS CQDs but the extra shell layer results in an impediment to charge transport. By systematically thinning the shell layer and then incorporating the resultant core/shell CQDs in a solar cell device, V_{oc} as high as 0.7 V is achieved with a CQD of 1.3 eV band gap, which is unprecedented at the time of this work. This is also the first report in which a core/shell CQD is utilised as the main photoactive material (both light absorption and charge transport) in a solution processed solar cell. With further surface chemistry improvements and device optimisation, solar cells with PCE as high as 6 % were fabricated.

(ii) Even with the optimised PbS/CdS CQD, the charge transport properties of PbS/CdS CQD film were limited compared to PbS CQD films due to lower carrier concentration.

Nevertheless, the second part of this work encompasses device architectural strategies used to overcome the lower conductivity of PbS/CdS as well as to take advantage of its lower defect concentration (or intrinsic nature). A new concept of 3-dimensional quantum funnelling was demonstrated and it was shown to help improve the length of possible carrier extraction across the device thickness. This is also the first time where blends of two different sized quantum dots of the same material are shown to be utilised in a solar cell device to improve charge extraction based on quantum funnelling. Further, another strategy which involves a *p-i-n* solar cell architecture was adopted to improve charge extraction. Although *p-i-n* CQD solar cells are not entirely a new concept at the time of this work[168], the use of intrinsic PbS/CdS and *p*-type PbS via the same spin coating film fabrication procedure is a simplistic and yet unique way to introduce extra band bending at the hole collecting region. Via this approach, the highest efficiency attained is 6.4 %.

(iii) The final part of this work addressed the low fill factors persistent in PbS CQD solar cell devices. The addition of a suitable hole transport material, P3HT, provided the understanding that the over-reliance on the depletion region for charge extraction and the unbalanced charge transport rates are the main reasons responsible for low fill factors. With suitable thickness and controlled oxidation of P3HT, devices with high *FF* were obtained, with the best *FF* of 0.72 recorded, which is the highest ever to be reported in the literature to date for PbS CQD solar cells. A champion device of 8.1 % *PCE* is obtained and devices are reported to be stable with air storage.

8.2   Future works

(i)   A deeper understanding on PbS/CdS core/shell CQD surface chemistry.

It was shown that the optimised CdS shell is 0.1 nm, which in theory is a sub-monolayer of CdS or partial CdS coverage on PbS CQD. It would be useful to understand why a

submonolayer of CdS shell is still providing a viable extent of passivation that it does, as seen in the substantial improvements of V_{oc} and a reduction in J_o. Another potentially interesting aspect of partial CdS coverage is the understanding of how ligands are bound to the surface of these core/shell CQD. XPS studies could potentially reveal how ligands are bound by examining Pb and Cd bonding states.

(ii)   Combining quantum funnels with the *p-i-n* strategy

The quantum funnel layer comprising PbS/CdS blends of two different band gaps could potentially be sandwiched between *n*-type TiO$_2$ and *p*-type PbS to reap the benefits of a stronger electric field formed within the device so as to overcome to poorer charge transport properties of the PbS/CdS blend layer. This could also mean that the active layer could be made thicker than the upright *p-i-n* structure discussed in chapter 6 due to quantum funnelling.

(iii)   Developing other solution phase ligand exchange that provides better passivation than iodine

Although the formation of a one-step deposition PbS ink is highly useful and allows the formation of smooth CQD films, the exchange process carried out with iodine-based ligands and passivation by iodine ligands has recently been reported to limit the device V_{oc} due to the formation of radiative sub-band levels[48]. Therefore, there is an urgent task to find an alternative that provides the same level of passivation and air-stability, but also introduces less sub-band levels.

(iv)   PbS-Iodide thickness optimization

As discussed at the end of Chapter 7, the EQE measurement illustrates that there is a limited amount of photoconversion in the longer wavelength regions, which could be attributed to

insufficient absorption of longer wavelength photons. Therefore, a further study can be done to see whether a thicker PbS-Iodide layer would improve the amount of photoconversion without sacrificing charge extraction through transport loses.

(v) Tandem/Multi-junction solar cells

Building upon the discovery of P3HT as a viable interfacial hole transport layer, P3HT could be integrated to form a graded recombination layer[203,204] that would be used to electrically connect the component cells of a multi-junction PbS solar cell in series. The fabrication of a tandem/multi-junction PbS solar cell, consisting of a bottom cell that incorporates larger band gap PbS and a top cell with smaller band gap PbS, would better utilise the solar spectrum and also improve the V_{oc} of the device.

References

1. Smil, V. *General energetics: energy in the biosphere and civilization.* (Wiley, 1991).

2. Fröhlich, C. & Lean, J. Solar radiative output and its variability: evidence and mechanisms. *Astron. Astrophys. Rev.* **12,** 273–320 (2004).

3. Gueymard, C. A., Myers, D. & Emery, K. Proposed reference irradiance spectra for solar energy systems testing. *Sol. Energy* **73,** 443–467 (2002).

4. Perez, R. A Way to the Most Abundant Energy. *Scientific American* (2013). at <http://www.scientificamerican.com/article/a-way-to-the-most-abundant-energy/>

5. Maps of Irradiation, Irradiance, and UV, Solar Radiation Data (SoDa). at <http://www.soda-is.com>

6. Christiana Honsberg & Stuart Bowden. PV CDROM- A collection of resources for the photovoltaic educator. at <http://www.pveducation.org/pvcdrom/properties-of-sunlight/blackbody-radiation>

7. World energy outlook 2015. (2015). at <http://www.iea.org/publications/freepublications/publication/WEO2015SpecialReportonEnergyandClimateChange.pdf>

8. Galen Barbose, Naïm Darghouth, Samantha Weaver & Ryan Wiser. Tracking the Sun IV: A Historical Summary of the Installed Costs of Photovoltaics in the United States from 1998 to 2010. *Lawrence Berkeley National Laboratory, Report No. LNL-5047e* (2011). at <https://emp.lbl.gov/sites/all/files/lbnl-6350e.pdf>

9. U.S. Solar Market Insight: Q2 2012. (July2012). at <http://www.seia.org/cs/research/SolarInsight>

10. Levelized Cost and Levelized Avoided Cost of New Generation Resources in the Annual Energy Outlook 2015. (2015). at <http://www.eia.gov/forecasts/aeo/pdf/electricity_generation.pdf>

11. Renewables 2015 Global Status Report. (2015). at <http://www.ren21.net/status-of-renewables/global-status-report/>

12. Beard, M. C., Luther, J. M. & Nozik, A. J. The promise and challenge of nanostructured solar cells. *Nat. Nanotechnol.* **9,** 951–954 (2014).

13. Photovoltaics report 2015. (2015). at <https://www.ise.fraunhofer.de/en/downloads-englisch/pdf-files-englisch/photovoltaics-report-slides.pdf>

14. Tekin, E., Smith, P. J. & Schubert, U. S. Inkjet printing as a deposition and patterning tool for polymers and inorganic particles. *Soft Matter* **4,** 703 (2008).

15. Choi, K.-H. *et al.* Characteristics of flexible indium tin oxide electrode grown by continuous roll-to-roll sputtering process for flexible organic solar cells. *Sol. Energy Mater. Sol. Cells* **93,** 1248–1255 (2009).

16. Tang, J. & Sargent, E. H. Infrared Colloidal Quantum Dots for Photovoltaics: Fundamentals and Recent Progress. *Adv. Mater.* **23,** 12–29 (2011).

17. Hillhouse, H. W. & Beard, M. C. Solar cells from colloidal nanocrystals: Fundamentals, materials, devices, and economics. *Curr. Opin. Colloid Interface Sci.* **14,** 245–259 (2009).

18. Semonin, O. E., Luther, J. M. & Beard, M. C. Quantum dots for next-generation photovoltaics. *Mater. Today* **15,** 508–515 (2012).

19. McDonald, S. A. *et al.* Solution-processed PbS quantum dot infrared photodetectors and photovoltaics. *Nat. Mater.* **4,** 138–142 (2005).

20. NREL. Best Research-Cell Efficiency Chart. (2015). at <http://www.nrel.gov/ncpv/images/efficiency_chart.jpg>

21. Carey, G. H. *et al.* Materials processing strategies for colloidal quantum dot solar cells: advances, present-day limitations, and pathways to improvement. *MRS Commun.* **3,** 83–90 (2013).

22. Murray, C. B., Norris, D. J. & Bawendi, M. G. Synthesis and characterization of nearly monodisperse CdE (E = sulfur, selenium, tellurium) semiconductor nanocrystallites. *J. Am. Chem. Soc.* **115,** 8706–8715 (1993).

23. Moreels, I. *et al.* Size-Dependent Optical Properties of Colloidal PbS Quantum Dots. *ACS Nano* **3,** 3023–3030 (2009).

24. Shockley, W. & Queisser, H. J. Detailed Balance Limit of Efficiency of p-n Junction Solar Cells. *J. Appl. Phys.* **32,** 510 (1961).

25. Nelson, J. *The Physics of Solar Cells*. (Imperial College Press, 2003).

26. Tang, J. *et al.* Quantum Dot Photovoltaics in the Extreme Quantum Confinement Regime: The Surface-Chemical Origins of Exceptional Air- and Light-Stability. *ACS Nano* **4,** 869–878 (2010).

27. Mott, N. F. *Conduction in non-crystalline materials*. (Clarendon Press ; Oxford University Press, 1993).

28. Efros, A. L. & Shklovskii, B. I. Coulomb gap and low temperature conductivity of disordered systems. *J. Phys. C Solid State Phys.* **8,** L49–L51 (1975).

29. Efros, A. L. Coulomb gap in disordered systems. *J. Phys. C Solid State Phys.* **9,** 2021–2030 (1976).

30. Mott, N. F. Electrons in disordered structures. *Adv. Phys.* **16,** 49–144 (1967).

31. Vanmaekelbergh, D. & Liljeroth, P. Electron-conducting quantum dot solids: novel materials based on colloidal semiconductor nanocrystals. *Chem. Soc. Rev.* **34,** 299–312 (2005).

32. Koole, R., Liljeroth, P., de Mello Donegá, C., Vanmaekelbergh, D. & Meijerink, A. Electronic Coupling and Exciton Energy Transfer in CdTe Quantum-Dot Molecules [*J. Am. Chem. Soc.* **2006** , *128* , 10436−10441]. *J. Am. Chem. Soc.* **129,** 10613–10613 (2007).

33. Zabet-Khosousi, A. & Dhirani, A.-A. Charge Transport in Nanoparticle Assemblies. *Chem. Rev.* **108,** 4072–4124 (2008).

34. Chandler, R., Houtepen, A., Nelson, J. & Vanmaekelbergh, D. Electron transport in quantum dot solids: Monte Carlo simulations of the effects of shell filling, Coulomb repulsions, and site disorder. *Phys. Rev. B* **75,** (2007).

35. Yin, Y. & Alivisatos, A. P. Colloidal nanocrystal synthesis and the organic–inorganic interface. *Nature* **437,** 664–670 (2005).

36. Haug, H. *Quantum theory of the optical and electronic properties of semiconductors*. (World Scientific, 1994).

37. Fulton, T. & Dolan, G. Observation of single-electron charging effects in small tunnel junctions. *Phys. Rev. Lett.* **59,** 109–112 (1987).

38. Beenakker, C. W. J. Theory of Coulomb-blockade oscillations in the conductance of a quantum dot. *Phys. Rev. B* **44,** 1646–1656 (1991).

39. Hanrath, T. Colloidal nanocrystal quantum dot assemblies as artificial solids. *J. Vac. Sci. Technol. Vac. Surf. Films* **30,** 030802 (2012).

40. Fu, H. *et al.* Impact of the Growth Conditions of Colloidal PbS Nanocrystals on Photovoltaic Device Performance. *Chem. Mater.* **23,** 1805–1810 (2011).

41. Zhitomirsky, D. *et al.* Colloidal Quantum Dot Photovoltaics: The Effect of Polydispersity. *Nano Lett.* **12,** 1007–1012 (2012).

42. Hines, M. A. & Scholes, G. D. Colloidal PbS Nanocrystals with Size-Tunable Near-Infrared Emission: Observation of Post-Synthesis Self-Narrowing of the Particle Size Distribution. *Adv. Mater.* **15,** 1844–1849 (2003).

43. Zhang, J. *et al.* Synthetic Conditions for High-Accuracy Size Control of PbS Quantum Dots. *J. Phys. Chem. Lett.* **6,** 1830–1833 (2015).

44. Pan, J. *et al.* Automated Synthesis of Photovoltaic-Quality Colloidal Quantum Dots Using Separate Nucleation and Growth Stages. *ACS Nano* **7,** 10158–10166 (2013).

45. Cademartiri, L. & Ozin, G. A. Emerging strategies for the synthesis of highly monodisperse colloidal nanostructures. *Philos. Trans. R. Soc. Math. Phys. Eng. Sci.* **368,** 4229–4248 (2010).

46. Yuan, M. *et al.* High-Performance Quantum-Dot Solids via Elemental Sulfur Synthesis. *Adv. Mater.* **26,** 3513–3519 (2014).

47. Moreels, I. *et al.* Size-Tunable, Bright, and Stable PbS Quantum Dots: A Surface Chemistry Study. *ACS Nano* **5,** 2004–2012 (2011).

48. Chuang, C.-H. M. *et al.* Open-Circuit Voltage Deficit, Radiative Sub-Bandgap States, and Prospects in Quantum Dot Solar Cells. *Nano Lett.* 150430101741001 (2015). doi:10.1021/acs.nanolett.5b00513

49. Kim, S. *et al.* Air-stable and efficient inorganic–organic heterojunction solar cells using PbS colloidal quantum dots co-capped by 1-dodecanethiol and oleic acid. *Phys. Chem. Chem. Phys.* **14,** 14999 (2012).

50. Im, S. H., Kim, H.-J., Kim, S., Kim, S.-W. & Seok, S. I. Improved air stability of PbS-sensitized solar cell by incorporating ethanedithiol during spin-assisted successive ionic layer adsorption and reaction. *Org. Electron.* **13,** 2352–2357 (2012).

51. Tang, J. *et al.* Quantum Dot Photovoltaics in the Extreme Quantum Confinement Regime: The Surface-Chemical Origins of Exceptional Air- and Light-Stability. *ACS Nano* **4,** 869–878 (2010).

52. Konstantatos, G., Levina, L., Fischer, A. & Sargent, E. H. Engineering the Temporal Response of Photoconductive Photodetectors via Selective Introduction of Surface Trap States. *Nano Lett.* **8,** 1446–1450 (2008).

53. Konstantatos, G. & Sargent, E. H. PbS colloidal quantum dot photoconductive photodetectors: Transport, traps, and gain. *Appl. Phys. Lett.* **91,** 173505 (2007).

54. Choi, H., Ko, J.-H., Kim, Y.-H. & Jeong, S. Steric-Hindrance-Driven Shape Transition in PbS Quantum Dots: Understanding Size-Dependent Stability. *J. Am. Chem. Soc.* **135,** 5278–5281 (2013).

55. Sykora, M. *et al.* Effect of Air Exposure on Surface Properties, Electronic Structure, and Carrier Relaxation in PbSe Nanocrystals. *ACS Nano* **4,** 2021–2034 (2010).

56. Foos, E. E. The Complex Interaction of Spectroscopic Shifts and Electronic Properties in Semiconductor Nanocrystal Films. *J. Phys. Chem. Lett.* **4,** 625–632 (2013).

57. Choi, H., Kwan Kim, J., Hoon Song, J., Kim, Y. & Jeong, S. Increased open-circuit voltage in a Schottky device using PbS quantum dots with extreme confinement. *Appl. Phys. Lett.* **102,** 193902 (2013).

58. Yoon, W. *et al.* Enhanced Open-Circuit Voltage of PbS Nanocrystal Quantum Dot Solar Cells. *Sci. Rep.* **3,** (2013).

59. Zhang, J., Gao, J., Miller, E. M., Luther, J. M. & Beard, M. C. Diffusion-Controlled Synthesis of PbS and PbSe Quantum Dots with *in Situ* Halide Passivation for Quantum Dot Solar Cells. *ACS Nano* **8,** 614–622 (2014).

60. Ip, A. H. *et al.* Hybrid passivated colloidal quantum dot solids. *Nat. Nanotechnol.* **7,** 577–582 (2012).

61. Thon, S. M. *et al.* Role of Bond Adaptability in the Passivation of Colloidal Quantum Dot Solids. *ACS Nano* **7,** 7680–7688 (2013).

62. Crisp, R. W. *et al.* Metal Halide Solid-State Surface Treatment for High Efficiency PbS and PbSe QD Solar Cells. *Sci. Rep.* **5,** 9945 (2015).

63. Marshall, A. R., Young, M. R., Nozik, A. J., Beard, M. C. & Luther, J. M. Exploration of Metal Chloride Uptake for Improved Performance Characteristics of PbSe Quantum Dot Solar Cells. *J. Phys. Chem. Lett.* **6,** 2892–2899 (2015).

64. Zhang, J. *et al.* PbSe Quantum Dot Solar Cells with More than 6% Efficiency Fabricated in Ambient Atmosphere. *Nano Lett.* **14,** 6010–6015 (2014).

65. Chuang, C.-H. M., Brown, P. R., Bulović, V. & Bawendi, M. G. Improved performance and stability in quantum dot solar cells through band alignment engineering. *Nat. Mater.* **13,** 796–801 (2014).

66. Labelle, A. J. *et al.* Colloidal Quantum Dot Solar Cells Exploiting Hierarchical Structuring. *Nano Lett.* **15,** 1101–1108 (2015).

67. Tang, J. *et al.* Colloidal-quantum-dot photovoltaics using atomic-ligand passivation. *Nat. Mater.* **10,** 765–771 (2011).

68. Johnston, K. W. *et al.* Schottky-quantum dot photovoltaics for efficient infrared power conversion. *Appl. Phys. Lett.* **92,** 151115 (2008).

69. Fischer, A. *et al.* Directly Deposited Quantum Dot Solids Using a Colloidally Stable Nanoparticle Ink. *Adv. Mater.* **25,** 5742–5749 (2013).

70. Ning, Z., Dong, H., Zhang, Q., Voznyy, O. & Sargent, E. H. Solar Cells Based on Inks of n-Type Colloidal Quantum Dots. *ACS Nano* **8,** 10321–10327 (2014).

71. Talapin, D. V. PbSe Nanocrystal Solids for n- and p-Channel Thin Film Field-Effect Transistors. *Science* **310,** 86–89 (2005).

72. Yu, D. n-Type Conducting CdSe Nanocrystal Solids. *Science* **300,** 1277–1280 (2003).

73. Liu, Y. *et al.* Dependence of Carrier Mobility on Nanocrystal Size and Ligand Length in PbSe Nanocrystal Solids. *Nano Lett.* **10,** 1960–1969 (2010).

74. Barkhouse, D. A. R., Pattantyus-Abraham, A. G., Levina, L. & Sargent, E. H. Thiols Passivate Recombination Centers in Colloidal Quantum Dots Leading to Enhanced Photovoltaic Device Efficiency. *ACS Nano* **2,** 2356–2362 (2008).

75. Yang, Z. *et al.* Colloidal Quantum Dot Photovoltaics Enhanced by Perovskite Shelling. *Nano Lett.* 151006155612009 (2015). doi:10.1021/acs.nanolett.5b03271

76. Kovalenko, M. V., Scheele, M. & Talapin, D. V. Colloidal Nanocrystals with Molecular Metal Chalcogenide Surface Ligands. *Science* **324,** 1417–1420 (2009).

77. Kovalenko, M. V., Bodnarchuk, M. I., Zaumseil, J., Lee, J.-S. & Talapin, D. V. Expanding the Chemical Versatility of Colloidal Nanocrystals Capped with Molecular Metal Chalcogenide Ligands. *J. Am. Chem. Soc.* **132,** 10085–10092 (2010).

78. Lee, J.-S., Kovalenko, M. V., Huang, J., Chung, D. S. & Talapin, D. V. Band-like transport, high electron mobility and high photoconductivity in all-inorganic nanocrystal arrays. *Nat. Nanotechnol.* **6,** 348–352 (2011).

79. Liu, H. *et al.* Systematic optimization of quantum junction colloidal quantum dot solar cells. *Appl. Phys. Lett.* **101,** 151112 (2012).

80. Ning, Z. *et al.* Air-stable n-type colloidal quantum dot solids. *Nat. Mater.* **13,** 822–828 (2014).

81. Anderson, N. C., Hendricks, M. P., Choi, J. J. & Owen, J. S. Ligand Exchange and the Stoichiometry of Metal Chalcogenide Nanocrystals: Spectroscopic Observation of Facile Metal-Carboxylate Displacement and Binding. *J. Am. Chem. Soc.* **135,** 18536–18548 (2013).

82. Oh, S. J. *et al.* Stoichiometric Control of Lead Chalcogenide Nanocrystal Solids to Enhance Their Electronic and Optoelectronic Device Performance. *ACS Nano* **7,** 2413–2421 (2013).

83. Luther, J. M. & Pietryga, J. M. Stoichiometry Control in Quantum Dots: A Viable Analog to Impurity Doping of Bulk Materials. *ACS Nano* **7,** 1845–1849 (2013).

84. Ning, Z. *et al.* Graded Doping for Enhanced Colloidal Quantum Dot Photovoltaics. *Adv. Mater.* **25,** 1719–1723 (2013).

85. Ning, Z. *et al.* All-Inorganic Colloidal Quantum Dot Photovoltaics Employing Solution-Phase Halide Passivation. *Adv. Mater.* **24,** 6295–6299 (2012).

86. Tang, J. *et al.* Quantum Junction Solar Cells. *Nano Lett.* **12,** 4889–4894 (2012).

87. Voznyy, O. *et al.* A Charge-Orbital Balance Picture of Doping in Colloidal Quantum Dot Solids. *ACS Nano* **6,** 8448–8455 (2012).

88. Brown, P. R. *et al.* Energy Level Modification in Lead Sulfide Quantum Dot Thin Films through Ligand Exchange. *ACS Nano* **8,** 5863–5872 (2014).

89. Luther, J. M. *et al.* Schottky Solar Cells Based on Colloidal Nanocrystal Films. *Nano Lett.* **8,** 3488–3492 (2008).

90. Johnston, K. W. *et al.* Efficient Schottky-quantum-dot photovoltaics: The roles of depletion, drift, and diffusion. *Appl. Phys. Lett.* **92,** 122111 (2008).

91. Tang, J. *et al.* Schottky quantum dot solar cells stable in air under solar illumination. *Adv. Mater.* **22,** 1398–1402 (2010).

92. Mai, X.-D. *et al.* Inverted Schottky quantum dot solar cells with enhanced carrier extraction and air-stability. *J Mater Chem A* **2,** 20799–20805 (2014).

93. Jean, J. *et al.* ZnO Nanowire Arrays for Enhanced Photocurrent in PbS Quantum Dot Solar Cells. *Adv. Mater.* **25,** 2790–2796 (2013).

94. Kramer, I. J. *et al.* Ordered Nanopillar Structured Electrodes for Depleted Bulk Heterojunction Colloidal Quantum Dot Solar Cells. *Adv. Mater.* **24,** 2315–2319 (2012).

95. Cheng, C. *et al.* Polystyrene Templated Porous Titania Wells for Quantum Dot Heterojunction Solar Cells. *ACS Appl. Mater. Interfaces* **6,** 14247–14252 (2014).

96. Rath, A. K. *et al.* Remote Trap Passivation in Colloidal Quantum Dot Bulk Nano-heterojunctions and Its Effect in Solution-Processed Solar Cells. *Adv. Mater.* **26,** 4741–4747 (2014).

97. Rath, A. K. *et al.* Solution-processed inorganic bulk nano-heterojunctions and their application to solar cells. *Nat. Photonics* **6,** 529–534 (2012).

98. Heeger, A. J. 25th Anniversary Article: Bulk Heterojunction Solar Cells: Understanding the Mechanism of Operation. *Adv. Mater.* **26,** 10–28 (2014).

99. Brown, P. R. *et al.* Improved Current Extraction from ZnO/PbS Quantum Dot Heterojunction Photovoltaics Using a MoO_3 Interfacial Layer. *Nano Lett.* **11,** 2955–2961 (2011).

100. Gao, J. *et al.* Quantum Dot Size Dependent $J - V$ Characteristics in Heterojunction ZnO/PbS Quantum Dot Solar Cells. *Nano Lett.* **11,** 1002–1008 (2011).

101. Liu, H. *et al.* Electron Acceptor Materials Engineering in Colloidal Quantum Dot Solar Cells. *Adv. Mater.* **23,** 3832–3837 (2011).

102. Yuan, M., Voznyy, O., Zhitomirsky, D., Kanjanaboos, P. & Sargent, E. H. Synergistic Doping of Fullerene Electron Transport Layer and Colloidal Quantum Dot Solids Enhances Solar Cell Performance. *Adv. Mater.* **27,** 917–921 (2015).

103. Ehrler, B. *et al.* Preventing Interfacial Recombination in Colloidal Quantum Dot Solar Cells by Doping the Metal Oxide. *ACS Nano* **7,** 4210–4220 (2013).

104. Hoye, R. L. Z. *et al.* Improved Open- Circuit Voltage in ZnO-PbSe Quantum Dot Solar Cells by Understanding and Reducing Losses Arising from the ZnO Conduction Band Tail. *Adv. Energy Mater.* **4,** n/a–n/a (2014).

105. Neo, M. S., Venkatram, N., Li, G. S., Chin, W. S. & Ji, W. Synthesis of PbS/CdS Core−Shell QDs and their Nonlinear Optical Properties. *J. Phys. Chem. C* **114,** 18037–18044 (2010).

106. Pacholski, C., Kornowski, A. & Weller, H. Self-assembly of ZnO: from nanodots to nanorods. *Angew. Chem. Int. Ed Engl.* **41,** 1188–1191 (2002).

107. Li, P. *et al.* Solvents Induced ZnO Nanoparticles Aggregation Associated with Their Interfacial Effect on Organic Solar Cells. *ACS Appl. Mater. Interfaces* **6,** 18172–18179 (2014).

108. Docampo, P. *et al.* Solution Deposition-Conversion for Planar Heterojunction Mixed Halide Perovskite Solar Cells. *Adv. Energy Mater.* **4,** (2014).

109. Bakulin, A. A. *et al.* Charge Trapping Dynamics in PbS Colloidal Quantum Dot Photovoltaic Devices. *ACS Nano* **7,** 8771–8779 (2013).

110. Ip, A. H. *et al.* Hybrid passivated colloidal quantum dot solids. *Nat. Nanotechnol.* **7,** 577–582 (2012).

111. Moreels, I., Fritzinger, B., Martins, J. C. & Hens, Z. Surface Chemistry of Colloidal PbSe Nanocrystals. *J. Am. Chem. Soc.* **130,** 15081–15086 (2008).

112. Turyanska, L. *et al.* Tailoring the physical properties of thiol-capped PbS quantum dots by thermal annealing. *Nanotechnology* **20,** 315604 (2009).

113. Klem, E. J. D. *et al.* Impact of dithiol treatment and air annealing on the conductivity, mobility, and hole density in PbS colloidal quantum dot solids. *Appl. Phys. Lett.* **92,** 212105 (2008).

114. Law, M. *et al.* Structural, Optical, and Electrical Properties of PbSe Nanocrystal Solids Treated Thermally or with Simple Amines. *J. Am. Chem. Soc.* **130,** 5974–5985 (2008).

115. Zhitomirsky, D. *et al.* N-type colloidal-quantum-dot solids for photovoltaics. *Adv. Mater. Deerfield Beach Fla* **24,** (2012).

116. Dai, N. & Chen, J. CdSe/ZnS core/shell quantum dots for bio-application. in (eds. Lu, W. & Young, J.) 602904–602904–6 (2006). doi:10.1117/12.667661

117. Zhao, H., Chaker, M., Wu, N. & Ma, D. Towards controlled synthesis and better understanding of highly luminescent PbS/CdS core/shell quantum dots. *J. Mater. Chem.* **21,** 8898 (2011).

118. Pietryga, J. M. *et al.* Utilizing the lability of lead selenide to produce heterostructured nanocrystals with bright, stable infrared emission. *J. Am. Chem. Soc.* **130,** 4879–4885 (2008).

119. Ghosh Chaudhuri, R. & Paria, S. Core/Shell Nanoparticles: Classes, Properties, Synthesis Mechanisms, Characterization, and Applications. *Chem. Rev.* **112,** 2373–2433 (2012).

120. Fern e, M. J. *et al.* Inorganic surface passivation of PbS nanocrystals resulting in strong photoluminescent emission. *Nanotechnology* **14,** 991–997 (2003).

121. Lifshitz, E. *et al.* Air-stable PbSe/PbS and PbSe/PbSexS1-x core-shell nanocrystal quantum dots and their applications. *J. Phys. Chem. B* **110,** 25356–25365 (2006).

122. Ning, Z. *et al.* Solar cells sensitized with type-II ZnSe–CdS core/shell colloidal quantum dots. *Chem. Commun.* **47,** 1536 (2011).

123. Vinayakan, R., Shanmugapriya, T., Nair, P. V., Ramamurthy, P. & Thomas, K. G. An Approach for Optimizing the Shell Thickness of Core-Shell Quantum Dots Using Photoinduced Charge Transfer. *J. Phys. Chem. C* **111,** 10146–10149 (2007).

124. Kinder, E. *et al.* Fabrication of All-Inorganic Nanocrystal Solids through Matrix Encapsulation of Nanocrystal Arrays. *J. Am. Chem. Soc.* **133,** 20488–20499 (2011).

125. Moroz, P. *et al.* Suppressed Carrier Scattering in CdS-Encapsulated PbS Nanocrystal Films. *ACS Nano* **7,** 6964–6977 (2013).

126. Liu, T.-Y. *et al.* Non-Injection and Low-Temperature Approach to Colloidal Photoluminescent PbS Nanocrystals with Narrow Bandwidth. *J. Phys. Chem. C* **113,** 2301–2308 (2009).

127. Rivest, J. B. & Jain, P. K. Cation exchange on the nanoscale: an emerging technique for new material synthesis, device fabrication, and chemical sensing. *Chem. Soc. Rev.* **42,** 89 (2013).

128. Zhao, H., Wang, D., Zhang, T., Chaker, M. & Ma, D. Two-step synthesis of high-quality water-soluble near-infrared emitting quantum dots via amphiphilic polymers. *Chem. Commun.* **46,** 5301 (2010).

129. Wyckoff, R. W. G. *Crystal Structures*. **1,** (Wiley, 1971).

130. Zhao, H., Chaker, M. & Ma, D. Effect of CdS shell thickness on the optical properties of water-soluble, amphiphilic polymer-encapsulated PbS/CdS core/shell quantum dots. *J. Mater. Chem.* **21,** 17483 (2011).

131. Fairclough, S. M. *et al.* Growth and Characterization of Strained and Alloyed Type-II ZnTe/ZnSe Core–Shell Nanocrystals. *J. Phys. Chem. C* **116,** 26898–26907 (2012).

132. Balasubramanian, S., Ceder, G. & Kolenbrander, K. D. Three-Dimensional Epitaxy: Thermodynamic Stability Range of Coherent Germanium Nanocrystallites in Silicon Host. *MRS Proc.* **405,** (2011).

133. Proffen, T. & Neder, R. B. *DISCUS*: a program for diffuse scattering and defect-structure simulation. *J. Appl. Crystallogr.* **30,** 171–175 (1997).

134. Weber, M. J. *Handbook of optical materials*. (CRC Press, 2003).

135. Blackburn, J. L., Chappell, H., Luther, J. M., Nozik, A. J. & Johnson, J. C. Correlation between Photooxidation and the Appearance of Raman Scattering Bands in Lead Chalcogenide Quantum Dots. *J. Phys. Chem. Lett.* **2,** 599–603 (2011).

136. Nelson, J. *The physics of solar cells*. (Imperial College Press ; Distributed by World Scientific Pub. Co, 2003).

137. Zhao, N. *et al.* Colloidal PbS Quantum Dot Solar Cells with High Fill Factor. *ACS Nano* **4,** 3743–3752 (2010).

138. Talapin, D. V., Lee, J.-S., Kovalenko, M. V. & Shevchenko, E. V. Prospects of Colloidal Nanocrystals for Electronic and Optoelectronic Applications. *Chem. Rev.* **110,** 389–458 (2010).

139. Nag, A. *et al.* Metal-free Inorganic Ligands for Colloidal Nanocrystals: S2–, HS –, Se2–, HSe–, Te2–, HTe –, TeS32–, OH– , and NH2 – as Surface Ligands. *J. Am. Chem. Soc.* **133,** 10612–10620 (2011).

140. Fafarman, A. T. *et al.* Thiocyanate-Capped Nanocrystal Colloids: Vibrational Reporter of Surface Chemistry and Solution-Based Route to Enhanced Coupling in Nanocrystal Solids. *J. Am. Chem. Soc.* **133,** 15753–15761 (2011).

141. Bae, W. K. *et al.* Highly Effective Surface Passivation of PbSe Quantum Dots through Reaction with Molecular Chlorine. *J. Am. Chem. Soc.* **134,** 20160–20168 (2012).

142. Zanella, M. *et al.* Atomic Ligand Passivation of Colloidal Nanocrystal Films via their Reaction with Propyltrichlorosilane. *Chem. Mater.* **25,** 1423–1429 (2013).

143. Fang, H.-H., Balazs, D. M., Protesescu, L., Kovalenko, M. V. & Loi, M. A. Temperature-Dependent Optical Properties of PbS/CdS Core/Shell Quantum Dot Thin Films: Probing the Wave Function Delocalization. *J. Phys. Chem. C* 150720065642000 (2015). doi:10.1021/acs.jpcc.5b05890

144. Greenham, N. C., Peng, X. & Alivisatos, A. P. Charge separation and transport in conjugated polymer/cadmium selenide nanocrystal composites studied by photoluminescence quenching and photoconductivity. *Synth. Met.* **84,** 545–546 (1997).

145. Mork, A. J., Weidman, M. C., Prins, F. & Tisdale, W. A. Magnitude of the Förster Radius in Colloidal Quantum Dot Solids. *J. Phys. Chem. C* **118,** 13920–13928 (2014).

146. Xu, F. *et al.* Efficient Exciton Funneling in Cascaded PbS Quantum Dot Superstructures. *ACS Nano* **5,** 9950–9957 (2011).

147. Carlson, D. E. & Wronski, C. R. Amorphous silicon solar cell. *Appl. Phys. Lett.* **28,** 671 (1976).

148. Choi, M.-J. *et al.* Tailoring of the PbS/metal interface in colloidal quantum dot solar cells for improvements of performance and air stability. *Energy Environ. Sci.* **7,** 3052 (2014).

149. Willard, D. M., Carillo, L. L., Jung, J. & Van Orden, A. CdSe−ZnS Quantum Dots as Resonance Energy Transfer Donors in a Model Protein−Protein Binding Assay. *Nano Lett.* **1,** 469–474 (2001).

150. Clapp, A. R. *et al.* Fluorescence Resonance Energy Transfer Between Quantum Dot Donors and Dye-Labeled Protein Acceptors. *J. Am. Chem. Soc.* **126,** 301–310 (2004).

151. Klar, T. A., Franzl, T., Rogach, A. L. & Feldmann, J. Super-Efficient Exciton Funneling in Layer-by-Layer Semiconductor Nanocrystal Structures. *Adv. Mater.* **17,** 769–773 (2005).

152. Kramer, I. J., Levina, L., Debnath, R., Zhitomirsky, D. & Sargent, E. H. Solar Cells Using Quantum Funnels. *Nano Lett.* **11,** 3701–3706 (2011).

153. Cnops, K. *et al.* 8.4% efficient fullerene-free organic solar cells exploiting long-range exciton energy transfer. *Nat. Commun.* **5,** 3406 (2014).

154. Guyot-Sionnest, P. Electrical Transport in Colloidal Quantum Dot Films. *J. Phys. Chem. Lett.* **3,** 1169–1175 (2012).

155. Kemp, K. W. *et al.* Interface Recombination in Depleted Heterojunction Photovoltaics based on Colloidal Quantum Dots. *Adv. Energy Mater.* **3,** 917–922 (2013).

156. Speirs, M. J. *et al.* Origin of the increased open circuit voltage in PbS–CdS core–shell quantum dot solar cells. *J Mater Chem A* **3,** 1450–1457 (2015).

157. Lai, L.-H., Protesescu, L., Kovalenko, M. V. & Loi, M. A. Sensitized solar cells with colloidal PbS–CdS core–shell quantum dots. *Phys Chem Chem Phys* **16,** 736–742 (2014).

158. Wheeler, D. A., Fitzmorris, B. C., Zhao, H., Ma, D. & Zhang, J. Ultrafast exciton relaxation dynamics of PbS and core/shell PbS/CdS quantum dots. *Sci. China Chem.* **54,** 2009–2015 (2011).

159. Litvin, A. P. *et al.* PbS Quantum Dots in a Porous Matrix: Optical Characterization. *J. Phys. Chem. C* **117,** 12318–12324 (2013).

160. Maiberg, M. & Scheer, R. Theoretical study of time-resolved luminescence in semiconductors. II. Pulsed excitation. *J. Appl. Phys.* **116,** 123711 (2014).

161. Kanevce, A., Levi, D. H. & Kuciauskas, D. The role of drift, diffusion, and recombination in time-resolved photoluminescence of CdTe solar cells determined through numerical simulation: The role of drift, diffusion, and recombination in time-resolved photoluminescence. *Prog. Photovolt. Res. Appl.* **22,** 1138–1146 (2014).

162. Chantana, J. *et al.* Investigation of Cu(In,Ga)Se2 absorber by time-resolved photoluminescence for improvement of its photovoltaic performance. *Sol. Energy Mater. Sol. Cells* **130,** 567–572 (2014).

163. Wehrenfennig, C., Liu, M., Snaith, H. J., Johnston, M. B. & Herz, L. M. Charge carrier recombination channels in the low-temperature phase of organic-inorganic lead halide perovskite thin films. *APL Mater.* **2,** 081513 (2014).

164. Stranks, S. D. *et al.* Electron-Hole Diffusion Lengths Exceeding 1 Micrometer in an Organometal Trihalide Perovskite Absorber. *Science* **342,** 341–344 (2013).

165. Zhitomirsky, D. *et al.* Engineering colloidal quantum dot solids within and beyond the mobility-invariant regime. *Nat. Commun.* **5,** 3803 (2014).

166. Hyun, B.-R., Choi, J. J., Seyler, K. L., Hanrath, T. & Wise, F. W. Heterojunction PbS Nanocrystal Solar Cells with Oxide Charge-Transport Layers. *ACS Nano* **7,** 10938–10947 (2013).

167. Kim, G.-H. *et al.* Inverted Colloidal Quantum Dot Solar Cells. *Adv. Mater.* **26,** 3321–3327 (2014).

168. Ko, D.-K., Brown, P. R., Bawendi, M. G. & Bulović, V. p-i-n Heterojunction Solar Cells with a Colloidal Quantum-Dot Absorber Layer. *Adv. Mater.* **26,** 4845–4850 (2014).

169. Gao, J. *et al.* Improvement in carrier transport properties by mild thermal annealing of PbS quantum dot solar cells. *Appl. Phys. Lett.* **102,** 043506 (2013).

170. Mora-Sero, I. *et al.* Selective contacts drive charge extraction in quantum dot solids via asymmetry in carrier transfer kinetics. *Nat. Commun.* **4,** 2272 (2013).

171. Willis, S. M., Cheng, C., Assender, H. E. & Watt, A. A. R. The Transitional Heterojunction Behavior of PbS/ZnO Colloidal Quantum Dot Solar Cells. *Nano Lett.* **12,** 1522–1526 (2012).

172. Luther, J. M. *et al.* Stability Assessment on a 3% Bilayer PbS/ZnO Quantum Dot Heterojunction Solar Cell. *Adv. Mater.* **22,** 3704–3707 (2010).

173. Ihly, R., Tolentino, J., Liu, Y., Gibbs, M. & Law, M. The Photothermal Stability of PbS Quantum Dot Solids. *ACS Nano* **5,** 8175–8186 (2011).

174. Jeong, K. S. *et al.* Enhanced Mobility-Lifetime Products in PbS Colloidal Quantum Dot Photovoltaics. *ACS Nano* **6,** 89–99 (2012).

175. Kramer, I. J. *et al.* Efficient Spray-Coated Colloidal Quantum Dot Solar Cells. *Adv. Mater.* **27,** 116–121 (2015).

176. Luther, J. M. *et al.* Structural, Optical, and Electrical Properties of Self-Assembled Films of PbSe Nanocrystals Treated with 1,2-Ethanedithiol. *ACS Nano* **2,** 271–280 (2008).

177. Snaith, H. J. Perovskites: The Emergence of a New Era for Low-Cost, High-Efficiency Solar Cells. *J. Phys. Chem. Lett.* **4,** 3623–3630 (2013).

178. Lattante, S. Electron and Hole Transport Layers: Their Use in Inverted Bulk Heterojunction Polymer Solar Cells. *Electronics* **3,** 132–164 (2014).

179. Bi, D., Yang, L., Boschloo, G., Hagfeldt, A. & Johansson, E. M. J. Effect of Different Hole Transport Materials on Recombination in $CH_3NH_3PbI_3$ Perovskite-Sensitized Mesoscopic Solar Cells. *J. Phys. Chem. Lett.* **4,** 1532–1536 (2013).

180. Su, Y.-W., Lan, S.-C. & Wei, K.-H. Organic photovoltaics. *Mater. Today* **15,** 554–562 (2012).

181. Park, N.-G. Perovskite solar cells: an emerging photovoltaic technology. *Mater. Today* **18,** 65–72 (2015).

182. Christians, J. A., Fung, R. C. M. & Kamat, P. V. An Inorganic Hole Conductor for Organo-Lead Halide Perovskite Solar Cells. Improved Hole Conductivity with Copper Iodide. *J. Am. Chem. Soc.* **136,** 758–764 (2014).

183. Zhao, K. *et al.* Solution-Processed Copper Thiocyanate (CuSCN) Hole Transporting Layer for Efficient p-i-n Perovskite Solar Cells. *J Mater Chem A* **3,** 20554–20559 (2015).

184. Gao, J. *et al.* n-Type Transition Metal Oxide as a Hole Extraction Layer in PbS Quantum Dot Solar Cells. *Nano Lett.* **11,** 3263–3266 (2011).

185. Pattantyus-Abraham, A. G. *et al.* Depleted-Heterojunction Colloidal Quantum Dot Solar Cells. *ACS Nano* **4,** 3374–3380 (2010).

186. Ludwigs, S., Andrienko, D. & SpringerLink (Online service). *P3HT revisited: from molecular scale to solar cell devices.* (2014). at <http://link.springer.com/book/10.1007/978-3-662-45145-8>

187. Park, S. K. *et al.* Electrical characteristics of poly (3-hexylthiophene) thin film transistors printed and spin-coated on plastic substrates. *Synth. Met.* **139,** 377–384 (2003).

188. Ukai, S., Ito, H., Marumoto, K. & Kuroda, S. Electrical Conduction of Regioregular and Regiorandom Poly(3-hexylthiophene) Doped with Iodine. *J. Phys. Soc. Jpn.* **74,** 3314–3319 (2005).

189. Noh, J. H. *et al.* Nanostructured TiO2/CH3NH3PbI3 heterojunction solar cells employing spiro-OMeTAD/Co-complex as hole-transporting material. *J. Mater. Chem. A* **1,** 11842 (2013).

190. Terán-Escobar, G., Pampel, J., Caicedo, J. M. & Lira-Cantú, M. Low-temperature, solution-processed, layered V2O5 hydrate as the hole-transport layer for stable organic solar cells. *Energy Environ. Sci.* **6,** 3088 (2013).

191. Demtsu, S. H. & Sites, J. R. Effect of back-contact barrier on thin-film CdTe solar cells. *Thin Solid Films* **510,** 320–324 (2006).

192. Kouskoussa, B. *et al.* On the improvement of the anode/organic material interface in organic solar cells by the presence of an ultra-thin gold layer. *Phys. Status Solidi A* **206,** 311–315 (2009).

193. Hintz, H., Peisert, H., Egelhaaf, H.-J. & Chassé, T. Reversible and Irreversible Light-Induced p-Doping of P3HT by Oxygen Studied by Photoelectron Spectroscopy (XPS/UPS). *J. Phys. Chem. C* **115,** 13373–13376 (2011).

194. Tress, W. *et al.* The role of the hole-transport layer in perovskite solar cells - reducing recombination and increasing absorption. in 1563–1566 (IEEE, 2014). at <http://ieeexplore.ieee.org/lpdocs/epic03/wrapper.htm?arnumber=6925216>

195. Marinova, N. *et al.* Light Harvesting and Charge Recombination in $CH_3NH_3PbI_3$ Perovskite Solar Cells Studied by Hole Transport Layer Thickness Variation. *ACS Nano* **9,** 4200–4209 (2015).

196. Peters, V., Tumkur, T. U. & Noginov, M. A. Control of chemical reactions in the vicinity of hyperbolic metamaterials and metallic surfaces. in FM1C.6 (OSA, 2014). doi:10.1364/CLEO_QELS.2014.FM1C.6

197. Silverstein, R. M. *Spectrometric identification of organic compounds.* (John Wiley and Sons, Inc, 2015).

198. Koster, L. J. A., Mihailetchi, V. D., Xie, H. & Blom, P. W. M. Origin of the light intensity dependence of the short-circuit current of polymer/fullerene solar cells. *Appl. Phys. Lett.* **87,** 203502 (2005).

199. Mihailetchi, V., Wildeman, J. & Blom, P. Space-Charge Limited Photocurrent. *Phys. Rev. Lett.* **94,** 126602 (2005).

200. Sharma, S. K. & Tewary, V. K. Theory of open-circuit photovoltage decay in a finite base solar cell with drift field. *J. Phys. Appl. Phys.* **15,** 1077–1087 (1982).

201. Lakhwani, G. *et al.* Probing Charge Carrier Density in a Layer of Photodoped ZnO Nanoparticles by Spectroscopic Ellipsometry. *J. Phys. Chem. C* **114,** 14804–14810 (2010).

202. Ning, Z. *et al.* Air-stable n-type colloidal quantum dot solids. *Nat. Mater.* **13,** 822–828 (2014).

203. Koleilat, G. I., Wang, X. & Sargent, E. H. Graded Recombination Layers for Multijunction Photovoltaics. *Nano Lett.* **12,** 3043–3049 (2012).

204. Wang, X. *et al.* Tandem colloidal quantum dot solar cells employing a graded recombination layer. *Nat. Photonics* **5,** 480–484 (2011).